Mukesh Yadav

On-chip refractive index sensors for lab-on-a-chip applications

Doctoral thesis

NTNU
Norwegian University of Science and Technology
Thesis for the Degree of
Philosophiae Doctor
Faculty of Information Technology and Electrical
Engineering
Department of Electronic Systems

NTNU
Norwegian University of
Science and Technology

Mukesh Yadav

On-chip refractive index sensors for lab-on-a-chip applications

Thesis for the Degree of Philosophiae Doctor

Trondheim, December 2023

Norwegian University of Science and Technology
Faculty of Information Technology and Electrical Engineering
Department of Electronic Systems

NTNU
Norwegian University of
Science and Technology

Abstract

Optical waveguide-based refractive index sensing is an emerging technology for the sensitive monitoring of molecular interactions. This technology could fulfill the requirements for "on-chip" detection in lab-on-a-chip platforms due to their outstanding characteristics of high sensitivity, label-free, and real-time detection. Due to their compact and portable design, these optical sensors have the potential to become an essential tool in the field of biosensing, offering an efficient and reliable method for real-time diagnosis. This could provide significant advantages over current analytical methods.

The focus of this thesis is to design and fabricate a novel optical waveguide-based label-free refractive index sensor. The aim is to develop a refractive index sensor with high sensitivity, a large measurement range, and the ability to multiplex. At the current stage, optical waveguide-based refractive index sensors are not used widely for commercial applications. This can be attributed to the challenges of the current waveguide-based sensor technology. For a sensor to become widely used for commercial application, it must possess high sensitivity, selectivity, wide measurement range, and multiplexing capability. The latter two features help reduce ambiguity in measurements, minimize the required sample volume, and improve the throughput to reduce the cost of sensor chips. This work has therefore concentrated on the development of a sensor system with all these features.

This thesis presents contributions to developing a novel on-chip sensor and its integration with other components for a lab-on-a-chip sensing platform. The included papers document the proof of concept, fabrication, and characterization of the developed Mach-Zehnder interferometer-assisted ring resonator configuration sensor. A paper on the development of bio-compatible microfluidics components for a lab-on-a-chip platform is also documented in the thesis. Additional investigation on an all-optical phase-modulated Mach-Zehnder interferometer sensor was done during the early part of the thesis and documented in the thesis.

Acknowledgements

I would like to acknowledge many people who have been involved in my thesis. Firstly, I want to express my gratitude to Astrid Aksnes, my supervisor, who gave me the opportunity to pursue my passion for a PhD. Astrid has always provided realistic perspectives and sound advice while allowing me to follow my own research ideas. My co-supervisor, Dag Roar Hjelme, has been invaluable in providing technical discussions throughout my studies and has always been a part of my project.

My project has been a part of the Lab-on-a-chip project at Dept. of Electronic Systems at NTNU, where I have met many wonderful colleagues. The interdisciplinary discussions have given me very helpful insights. I would also like to acknowledge the work of the master students that I co-supervised. Their dedication and valuable contributions have been very helpful.

I am immensely grateful to my colleagues at Gløshaugen, particularly to Jens Høvik, who introduced me to the finer aspects of SOI fabrication and provided me with valuable advice whenever I encountered issues with my experimental setup. I would also like to express my gratitude to Nina Bjørk Arnfinnsdottir for introducing me to biofunctionalization and for collaborating with me on long and demanding experiments in the lab. Additionally, I would like to thank Jong Wook Noh for his invaluable assistance in modifying the experimental setup and for his excellent editing skills in writing our papers.

During lunch and coffee breaks, I enjoyed the company of Ergys Puka and Amar Jaiswal. I would also like to thank my family for providing me with the best environment possible, and my dad for always asking about my work, and my mom for reminding me to eat on time. Lastly, I am grateful to my wife and best friend, Bhumika Shukla, whose impact on my life is immeasurable.

Contributions

I conducted the research for this thesis at the Department of Electronic Systems, Norwegian University of Science and Technology (NTNU) in Trondheim, Norway, between August 2017 and December 2021. The NTNU Nanolab cleanroom facility was utilized for the fabrication needed for the thesis. Research studies have been performed under the supervision of Professor Astrid Aksnes (NTNU), and co-supervisor Professor Dag Roar Hjelme (NTNU). The work has been a part of the Lab-on-a-chip project, with funding from the Research Council of Norway through grant numbers 248869/O70 and 245963/F50.

During the doctoral study I have been co-supervisor for four master students: Eivind Jülke Røer, Espen Hovland, Halvor R. Fergestad and Lars Olav Skrebergene.

PUBLICATIONS

Paper I
Mukesh Yadav, Jong Wook Noh, Dag Roar Hjelme, and Astrid Aksnes, "Spectral shaping of ring resonator transmission response," Opt. Express 29, 3764-3771 (2021).

M.Y. planned the study and performed theoretical analysis under supervision from D.R.H. and A.A.. **M.Y.** performed fabrication and characterization. J.W.N. assisted **M.Y.** in modified of the optical experimental set-up. **M.Y.** did all data analysis. **M.Y.** drafted the manuscript together with J.W.N.. All authors contributed to the discussion of results and preparations of the manuscript.

Paper II
Mukesh Yadav and Astrid Aksnes, "Multiplexed Mach-Zehnder interferometer assisted ring resonator sensor," Opt. Express 30, 1388-1396 (2022).

M.Y. planned and designed the experiment under supervision of A.A.. **M.Y.** performed fabrication, characterization and sensing measurements. **M.Y.** did all data analysis. **M.Y.** drafted the first version of the manuscript. A.A. and **M.Y.** contributed to the discussion of results and preparations of the manuscript.

Paper III

Linda Sønstevold, Mukesh Yadav, Nina Bjørk Arnfinnsdottir, Aina Kristin Herbjørnrød, Geir Uri Jensen, Astrid Aksnes, and Michal Marek Mielnik, "Biocompatible bonding of a rigid off-stoichiometry thiol-ene-epoxy polymer microfluidic cartridge to a biofunctionalized silicon biosensor," Journal of Micromechanics and Microengineering 32(7), 075008 (2022).

L.S. conceptualized and designed the experiment under supervision of M.M.M.. L.S. performed the fabrication of microfluidics and physical characterization. **M.Y.** fabricated the sensor chip. **M.Y.** together with N.B.A. performed the bio-functionalization and sensing measurements. **M.Y.** did sensor measurement analysis. A.K.H and M.M.M. assisted L.S. in characterization. G.U.J. assisted L.S. in methodology. L.S. drafted the first manuscript. L.S., A.A. and M.M.M. contributed to reviewing and editing of the manuscript.

Paper IV

Mukesh Yadav, Jens Høvik, Dag Roar Hjelme, Astrid Aksnes, "Sensitivity enhanced biophotonic sensor utilizing sub-wavelength gratings," Proc. SPIE 10729, Optical Sensing, Imaging, and Photon Counting: From X-Rays to THz, Vol. 10729, 76-80 (2018).

M.Y. planned the study and designed the experiment under supervision from J.H., D.R.H. and A.A.. **M.Y.** performed simulation with guidance from J.H.. **M.Y.** did all data analysis. **M.Y.** drafted the first draft of the manuscript. All authors contributed to the discussion of results and preparations of the manuscript.

PATENT APPLICATION

1. Mukesh Yadav, Astrid Aksnes, Dag Roar Hjelme, Jens Høvik - European Patent Application No. 21714357.7 (4121742). (Intention to grant announced).

2. Mukesh Yadav, Astrid Aksnes, Dag Roar Hjelme, Jens Høvik - United States Patent Application No. 17/912327 (US2023-0134264).

OTHER RESULTS

Conference contributions and other results which are not directly related or otherwise overlap with existing contributions to the thesis are:

1. Mukesh Yadav, and Astrid Aksnes. "Mach-Zehnder interferometer assisted ring resonator configuration for refractive index sensing." The European Conference on Lasers and Electro-Optics, Optica Publishing Group, ch_6_5. (2021).

2. Jens Høvik, Mukesh Yadav, Jong Wook Noh, and Astrid Aksnes, "Waveguide asymmetric long-period grating couplers as refractive index sensors," Opt. Express 28, 23936-23949 (2020).

3. Mukesh Yadav, Jong Wook Noh, Dag Roar Hjelme, and Astrid Aksnes. "Hybrid ring resonator sensor with high quality factor and wide dynamic range." Optical Sensors, Optica Publishing Group, SM3B-3 (2020).

4. Jens Høvik, Mukesh Yadav, Nina Bjørk Arnfinnsdottir, Astrid Aksnes, "Lab-on-a-chip photonic biosensor for detection of antigens," Proc. SPIE 10728, Biosensing and Nanomedicine XI, 1072806 (2018).

5. Mukesh Yadav, Jens Høvik, and Astrid Aksnes. "Highly sensitive lab-on-a-chip biosensor utilizing phase-modulated Mach-Zehnder interferometer." Optical Sensors, Optica Publishing Group, SeTu4E-5 (2018).

SOFTWARE

MATLAB: MATLAB program was used for theoretical and experimental data analysis during the PhD research.

COMSOL: Finite element method (FEM) from COMSOL software was used to perform simulation studies on proposed sensor designs.

MPB: MIT Photonic Bands (MPB) software was used to study the dispersion effect on optical waveguides with different cladding and subwavelength gratings.

Contents

List of Figures

List of Tables

Nomenclature

CHAPTER 1

Introduction

Most clinical diagnostics are carried out in advanced laboratories, which can be costly and time-consuming. To address this issue, dedicated portable and reliable sensors called biosensors can be used. These sensors are designed for biosensing applications and can quickly detect biochemical interactions and convert them into measurable quantities, providing an affordable and fast diagnostic solution[1–11].

Optical waveguide-based biosensors have emerged as a reliable system for measuring analytes in body fluids. In the past, sensors based on optical technology were limited to laboratory environments due to limited fabrication capabilities and dependence on bulky free-space optics. However, recent advancements in microelectronics and silicon technology have made it possible to produce smaller structures, encouraging the development of waveguide-based sensors[12,13]. These sensors are compact and portable, making them ideal for fast and multiplexed biosensing applications.

Traditionally, biological research relied on the attachment of labels such as fluorescent dies and nanoparticles to target analytes for detection. The labeled detection technique provides high sensitivity and even allows the detection of a single analyte molecule. However, labeling of analytes can alter the analyte functionally and physically[14]. Moreover, the labeling process requires intensive labor and is costly. Optical waveguide sensors are capable of label-free detection of biochemical interactions. Label-free detection is the direct detection of target analytes through some physical properties. Label-free detection requires receptors or ligands and target analytes. Receptors are attached to the sensor surface and target analytes bind to these receptors due to affinity interaction. The binding of analytes with receptors creates complexes and changes the refractive index of the sensor surface. Waveguide-based refractive index sensors can simultaneously measure refractive index change induced by receptor-analyte interaction. An optical waveguide-based refractive index sensor converts the refractive index change into a measurable quantity, such as intensity change. The sensitivity to detect the refractive index change due to the analyte depends on the sensor design, while selectivity towards specific analytes relies on a process that involves attaching receptors to the sensor surface to

capture specific analytes called biofunctionalization [1].

These sensors have vast potential applications in medical diagnosis, food safety, environmental monitoring, and many other fields. Optical waveguide-based sensors can be designed to be compact and portable, making them a valuable tool in biosensing for real-time diagnosis. However, at the current stage, optical waveguide-based refractive index sensors are not used widely for commercial applications. To the author's knowledge, there are only a few companies (Genalyte and SiPhox) producing optical waveguide-based sensors for commercial usage. This can be attributed to the challenges present in the current sensor technology. In addition to sensitivity and selectivity, waveguide sensors should also possess a wide measurement range and the ability to perform multiplexing. The latter two features help reduce ambiguity in measurements, minimize the required sample volume, and improve the throughput to reduce the cost of sensor chips. The development of a waveguide-based refractive index sensor with all these features is challenging and it is hindering the commercialization of optical waveguide sensors for various applications. To address these challenges, extensive research is ongoing. This thesis work is also targeted to address these challenges.

In addition to the optical waveguide-based sensor chip, biofunctionalization and microfluidics are used to make the sensor selective to the specific analyte and to control the flow of relevant fluids over the sensor surface, respectively. The Lab-on-a-chip platform, which is a complete system created by combining biofunctionalization and a microfluidics subsystem with the optical waveguide sensors, is ideal for biosensing applications. It provides a highly integrated and automated platform for rapid, sensitive, and selective detection of various analytes in different body fluids.

This Ph.D. project has been part of the research project called Lab-on-a-chip platform for bio-photonic sensing. The long-term goal is to develop an integrated Label-free biosensor platform that could detect multiple biomarkers simultaneously.

1.1 AIM OF THESIS

This thesis aimed to develop a multiplexed optical waveguide-based refractive index sensor with an extensive measurement range and high sensitivity for refractive index sensing applications. This sensor is developed on the silicon-on-insulator waveguide platform and operates in the narrow C-band wavelength range. The main contributions of this thesis are summarized as follows:

- Evaluation of prior refractive index sensing techniques concerning their sensitivity, measurement range, and multiplexing.

- Design and theoretical analysis to optimize the sensor design to obtain the above-mentioned capabilities.

- Fabrication of sensors on a silicon-on-insulator platform utilizing electron beam lithography and dry etching techniques. Characterization using scanning electron microscopy.

- Fabrication of microfluidics system using PDMS polymer with soft lithography technique.

- Optical characterization to measure the fabricated sensors' sensitivity, measurement range, and multiplexing capability using an external cavity tunable laser with a 1500- 1600 nm wavelength range. Further optimization of fabrication to improve the results.

- Demonstrate the multiplexed sensor with tunable measurement range and low detection limit using saline solutions with different salt concentrations.

1.2   CONTRIBUTIONS BEYOND STATE-OF-THE-ART TECHNOLOGY

This thesis contributed beyond the state-of-the-art through the development of a novel sensor called the Mach-Zehnder interferometer-assisted ring resonator configuration (MARC) sensor. This includes developing the MARC sensor from the idea stage to the application stage. This also resulted in a patent application titled 'Optical sensing apparatus'.

1.3   REFERENCES

[1] Heather M Robison and Ryan C Bailey. A guide to quantitative biomarker assay development using whispering gallery mode biosensors. *Current Protocols in Chemical Biology* **9** (3), 158–173 (2017). Cited on page/s 1, 2.

[2] Tom Claes, Jordi Girones Molera, Katrien De Vos, Etienne Schacht, Roel Baets, and Peter Bienstman. Label-free biosensing with a slot-waveguide-based ring resonator in silicon on insulator. *IEEE Photonics Journal* **1** (3), 197–204 (2009). Cited on page/s 1.

[3] Katrien De Vos, Irene Bartolozzi, Etienne Schacht, Peter Bienstman, and Roel Baets. Silicon-on-insulator microring resonator for sensitive and label-free biosensing. *Optics Express* **15** (12), 7610–7615 (2007). Cited on page/s 1.

[4] Carl Fredrik Carlborg, *et al.* A packaged optical slot-waveguide ring resonator sensor array for multiplex label-free assays in labs-on-chips. *Lab on a Chip* **10** (3), 281–290 (2010). Cited on page/s 1.

[5] RG Heideman and PV Lambeck. Remote opto-chemical sensing with extreme sensitivity: design, fabrication and performance of a pigtailed integrated optical phase-modulated Mach-Zehnder interferometer system. *Sensors and Actuators B: Chemical* **61** (1-3), 100–127 (1999). Cited on page/s 1.

[6] RG Heideman, RPH Kooyman, and Jan Greve. Performance of a highly sensitive optical waveguide Mach-Zehnder interferometer immunosensor. *Sensors and Actuators B: Chemical* **10** (3), 209–217 (1993). Cited on page/s 1.

[7] P Prabhathan, VM Murukeshan, Zhang Jing, and Pamidighantam V Ramana. Compact SOI nanowire refractive index sensor using phase shifted bragg grating. *Optics Express* **17** (17), 15330–15341 (2009). Cited on page/s 1.

[8] Enxiao Luan, Han Yun, Minglei Ma, Daniel M Ratner, Karen C Cheung, and Lukas Chrostowski. Label-free biosensing with a multi-box sub-wavelength phase-shifted bragg grating waveguide. *Biomedical Optics Express* **10** (9), 4825–4838 (2019). Cited on page/s 1.

[9] Adam L Washburn, L Cary Gunn, and Ryan C Bailey. Label-free quantitation of a cancer biomarker in complex media using silicon photonic microring resonators. *Analytical Chemistry* **81** (22), 9499–9506 (2009). Cited on page/s 1.

[10] Tom Claes, Wim Bogaerts, and Peter Bienstman. Experimental characterization of a silicon photonic biosensor consisting of two cascaded ring resonators based on the Vernier-effect and introduction of a curve fitting method for an improved detection limit. *Optics Express* **18** (22), 22747–22761 (2010). Cited on page/s 1.

[11] Alexander Ksendzov and Yangyang Lin. Integrated optics ring-resonator sensors for protein detection. *Optics Letters* **30** (24), 3344–3346 (2005). Cited on page/s 1.

[12] Wim Bogaerts, Peter De Heyn, Thomas Van Vaerenbergh, Katrien De Vos, Shankar Kumar Selvaraja, Tom Claes, Pieter Dumon, Peter Bienstman, Dries Van Thourhout, and Roel Baets. Silicon microring resonators. *Laser & Photonics Reviews* **6** (1), 47–73 (2012). Cited on page/s 1.

[13] Wim Bogaerts, Roel Baets, Pieter Dumon, Vincent Wiaux, Stephan Beckx, Dirk Taillaert, Bert Luyssaert, Joris Van Campenhout, Peter Bienstman, and Dries Van Thourhout. Nanophotonic waveguides in silicon-on-insulator fabricated with cmos technology. *Journal of Lightwave Technology* **23** (1), 401 (2005). Cited on page/s 1.

[14] Vimala Rani Samuel and K Jagajjanani Rao. A review on label free biosensors. *Biosensors and Bioelectronics: X* page 100216 (2022). Cited on page/s 1.

CHAPTER 2

Background

2.1 OPTICAL WAVEGUIDE: BASICS

An optical waveguide consists of a transparent dielectric material with a higher refractive index than the surrounding material. A dielectric structure with refractive index contrast restricts the light within the high-index material and allows guided light propagation. Confinement and propagation of light in the high-index material occur due to total internal reflection. An optical fiber is a typical example of a waveguide structure. Optical fibers are cylindrical waveguides that can transmit optical signals over long distances. They are commonly used for telecommunication applications. In the early days, telecommunication signals that were transmitted through optical fibers required periodic reamplification and reconditioning. To achieve this, repeaters were used. Repeaters were typically composed of a laser, a detector, lenses, and mirrors. These components were spread out on an optical bench, which made repeaters sensitive to temperature changes, thermal gradients, and mechanical vibrations from separately mounted parts. To address these challenges in a repeater, S.E. Miller from Bell Laboratory suggested combining all components required for a repeater into a single chip and interconnecting them with a small optical waveguide [1]. This led to the development of integrated optics and on-chip waveguides [2]. Initially, integrated optics and on-chip waveguides were mostly limited to telecommunication applications. In recent decades, research interest in the development of on-chip channel waveguide-based devices for other applications has increased rapidly. Channel waveguides provide the advantage of fabricating complex device structures in a few mm^2 chips. The small size of channel waveguides makes this technology suitable also for developing highly sensitive, multiplexed portable optical sensors.

2.2 OPTICAL WAVEGUIDE-BASED REFRACTIVE INDEX SENSOR

Optical waveguide-based refractive index sensors use the waveguiding principle to propagate light and detect the refractive index change induced by the analyte

on the waveguide surface. Optical waveguide-based refractive index sensors are highly sensitive and can be used to detect small index changes induced by variations in gas composition, humidity, temperature, and binding of a specific biomarker to the sensor surface[3,4].

2.2.1 Principle

Optical waveguide-based refractive index sensors are generally based on the evanescent field sensing principle. An evanescent field is an exponentially decaying electric field that originates from the interface between the high-index core and the low-index top cladding material when total internal reflection occurs. It is given by $E_y(x, z) = E_{y0}e^{-\alpha x}$, where E_{y0} is the electric field at the interface, x is the penetration depth in cladding, and α is the attenuation coefficient. In evanescent field sensing, this fast-decaying evanescent field interacts with the density or refractive index change in the surrounding (cladding), which results in a change in the effective refractive index of the guided mode in the waveguide[4,5]. An effective refractive index can be defined as the free space velocity divided by the waveguide phase velocity. Typically, the evanescent field in the cladding layer extends for a few hundred nanometers. However, it can be further extended by tuning the refractive index of the cladding.

2.2.2 Evaluation parameters (sensitivity, LOD, selectivity, measurement range, multiplexing)

Sensitivity is an essential evaluation parameter for an optical waveguide-based refractive index sensor. In evanescent field sensing, sensitivity is determined by the strength of interaction of the evanescent field with the measurand. It can be divided into categories: bulk sensitivity and surface sensitivity. Bulk sensitivity considers the refractive index change of the entire waveguide cladding. However, surface sensitivity considers the refractive index change within the few tens to hundreds of nanometers above waveguide surface[6]. Sensor output can be intensity, resonance wavelength, or resonance angle, depending on the sensor design. Sensitivity for different sensor designs is described in the following section. In this thesis, bulk sensitivity was generally preferred and used to define sensor sensitivity

Limit of detection (LOD) refers to the smallest refractive index change that can be reliably detected. It is a critical parameter to evaluate the performance of the sensor. It depends on the sensor, read-out equipment, overall noise level, and surface chemistry. It is generally calculated as $3\sigma/S$, where σ is the standard

deviation in the sensor response and S is the sensor sensitivity[7,8].

Selectivity is a crucial sensor characteristic that makes it sensitive only to a specific target analyte. It prevents any other analytes from attaching or adsorbing to the sensor surface. It is represented as the ratio of the sensor signal induced by the target analyte and the interfering substance (target/interference). The attachment of unspecific analytes can cause a significant background signal and worsen the detection limit. Typically, sensor surface coating or surface functionalization is used to control selectivity[9].

Measurement range of a refractive index sensor is defined as a sensor's maximum detectable refractive index change (Δn_{max}). The measurement range of a sensor describes its versatility. It is generally limited by the inherent characteristic of sensors. E.g., the free spectral range of a ring resonator poses a limitation to the measurement range, and it is calculated as FSR/S, where FSR is the free spectral range of a ring resonator and S is the sensitivity of the ring resonator sensor[10].

Multiplexing or high throughput is a crucial parameter in a sensor. It improves the reliability of the sensor response if used to run a parallel analysis for the same analyte. It can also multiplex multiple analytes. It reduces the cost and time required for the chemical analysis of several analytes.

2.3   SENSOR DESIGNS

As described in section 2.2.1, in evanescent field sensing, the interaction of the evanescent field and the analyte causes a change in the effective refractive index of the guided mode. However, an effective refractive index change due to an analyte is not a measurable quantity and thus requires a specific configuration of waveguides to convert this change into a measurable quantity. Various kinds of sensor designs exist, including Mach Zehnder interferometer[11–17], ring resonator[18–22], Vernier effect-based sensor[23,24], OWLS[25,26], etc. These sensors utilize different basic principles to convert an effective refractive index change into a measurable quantity. Moreover, these sensor designs provide different sensitivity and measurement ranges. A sensor design is selected for sensing applications depending on the user requirements of accuracy, sensitivity, and measurement range.
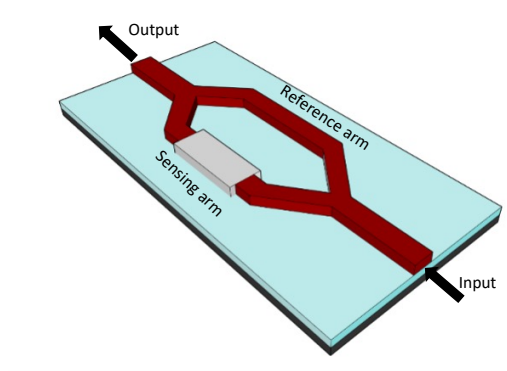
FIGURE 2.1. Schematic of a Mach-Zehnder interferometer.

2.3.1 Mach-Zehnder interferometer

A Mach-Zehnder interferometer (MZI) sensor is an optical sensor design that utilizes the interference principle to quantify the refractive index change due to an analyte or a measurand[11–17]. In the MZI configuration, a single-mode input waveguide is split into two arms and recombined using a Y-branch into an output waveguide. One of the arms is used as a reference arm, and the other arm is used as a sensing arm. The reference arm is covered with a non-porous solid top cladding. The sensing arm is without the complete cladding and is open for interaction between the evanescent field and the surrounding. The refractive index change experienced by the sensing arm results in a change in the effective refractive index of the guided mode. The schematic of an MZI sensor is shown in Fig.2.1. An effective refractive index change in the sensing arm due to a measurand leads to a phase change at the output. The phase change at the waveguide output of a symmetric MZI can be directly calculated from the waveguide output intensity as:

$$I = I_s + I_r + 2\sqrt{I_s I_r} \cos \Delta\phi_m, \tag{2.1}$$

$$\Delta\phi_m = \cos^{-1}\left(\frac{I - I_s - I_r}{2\sqrt{I_s I_r}}\right), \tag{2.2}$$

where, I_s, I_r, and $\Delta\phi_m$ are the intensity in the sensing arm, intensity in the reference arm, and phase change due to the measurand respectively. The phase change due to the measurand is given as:

$$\Delta\phi_m = \frac{2\pi}{\lambda_0} L_{int} \Delta n_{eff}, \tag{2.3}$$
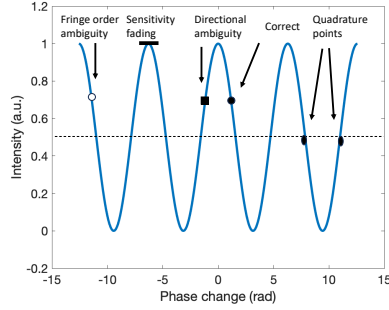
FIGURE 2.2. Plot showing the MZI periodic intensity response and the associated intrinsic problems for determining the phase change associated with the measurand.

where, λ_0, L_{int}, Δn_{eff} are the wavelength of the monochromatic source, interaction length in the sensing arm and the effective refractive index change due to the analyte, respectively.

The sensitivity of an MZI sensor is calculated by differentiating the above-mentioned equation and is given as:

$$\frac{\partial \Delta \phi_m}{\partial n_c} = \frac{2\pi L_{int}}{\lambda} \frac{\partial n_{eff}}{\partial n_c}. \tag{2.4}$$

As shown in Eq. 2.4, the MZI sensitivity scales with the sensing arm length L_{int}, and the waveguide sensitivity constant $\frac{\partial n_{eff}}{\partial n_c}$. Scaling of sensitivity with length makes MZI sensors highly sensitive. Moreover, they can be used with cost-effective fixed wavelength laser sources by tracking the interference sinusoidal intensity response. However, high sensitivity MZI sensors require fast detectors to detect the output intensity fast enough to reduce ambiguity in results due to the periodic nature of the interferometer output. Due to the periodic nature, interferometer-based sensors have limitations of phase ambiguity and sensitivity fading, which lead to false results[11]. These conditions in the MZI output response are highlighted in Figure 2.2.

2.3.2   Ring resonator

A ring resonator (RR) is a sensor design that utilizes the optical resonance phenomenon to detect the surrounding refractive index change[18–22]. A channel bus waveguide is placed adjacent to the ring waveguide in a ring resonator. The schematic of a ring resonator is shown in Fig.2.3. In a ring resonator configuration, a bus waveguide is utilized to couple waves into the ring. When the wavelength of light fits a whole number of times within the optical path length
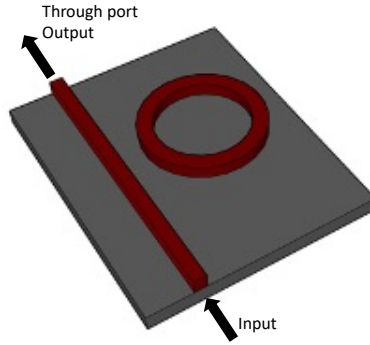
FIGURE 2.3. Schematic of a ring resonator.

of the ring, it causes constructive interference, resulting in resonance within the cavity. From this condition we can calculate the resonance wavelength:

$$\lambda_{res} = \frac{n_{eff}L}{m}, m = 1, 2, 3..., \tag{2.5}$$

where, L is the cavity length and n_{eff} is the effective index of the resonant mode.

At these resonances, an abrupt drop in intensity is measured in the transmission spectrum of the bus waveguide (Through port). The sharpness of the resonance is defined as the quality factor and calculated as:

$$Q = \frac{\lambda}{\Delta\lambda_{FWHM}}, \tag{2.6}$$

where, λ is the resonance wavelength and $\Delta\lambda_{FWHM}$ is the full width half maximum of the resonance.

In ring resonator sensors, any refractive index change in the surrounding of the ring induces a phase shift in the guided mode and results in a resonance shift. This resonance wavelength shift scales with the amount of refractive index change. However, like MZI sensors, ring resonators are prone to ambiguous results if the resonance shift is faster than the laser wavelength tuning and detection system.

The sensitivity of the ring resonator is defined as the resonance wavelength shift w.r.t the change in the surrounding refractive index, and is given as:

$$S = \frac{\Delta\lambda_{res}}{\Delta n}, \tag{2.7}$$

where, $\Delta\lambda_{res}$ is the resonance wavelength shift and Δn is the surrounding index change.
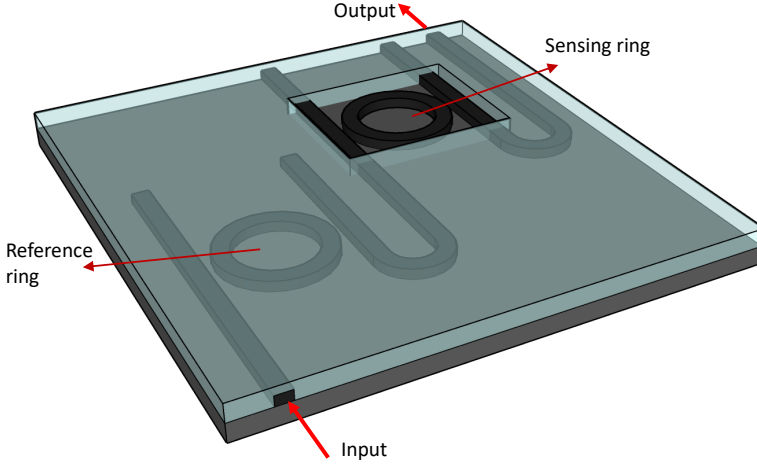
FIGURE 2.4.   Schematic of a cascaded ring resonator-based Vernier sensor design

2.3.3   *Vernier-based sensor*

The vernier scale is a method used to improve the measurement accuracy of an instrument. In this method, two scales with different periods are overlaid over each other, and the overlap between lines on the two scales is used to improve the accuracy of measurements. This fundamental principle of vernier scale is utilized in Vernier-based optical sensors [23,24]. In these sensors, periodic intensity responses from optical structures are overlaid. Cascaded optical networks are being used for overlaid vernier response. Cascaded ring resonators and ring resonators cascaded with an MZI are a few Vernier-based sensor examples. The cascaded ring resonator configuration is shown in Fig. 2.4.

The sensitivity of the cascaded ring resonator is given as [23]:

$$\frac{\partial \lambda_{central}}{\partial n_{env}} = \frac{FSR_{ref}}{FSR_{ref} - FSR_{sensor}} \frac{\frac{\partial n_{eff,sensor}}{\partial n_{env}} \lambda}{n_{g,sensor}}, \tag{2.8}$$

where, $\frac{\partial n_{eff,sensor}}{\partial n_{env}}$ is the change of the effective index of the sensor ring resonator waveguide due to a change of the refractive index in the environment of the sensor and $n_{g,sensor}$ is the group index of the sensor ring resonator waveguide. FSR_{ref} and FSR_{sensor} are the free spectral range of the reference ring and the sensing ring, respectively. In cascaded sensors, the sensitivity scales with the factor $\frac{FSR_{ref}}{FSR_{ref} - FSR_{sensor}}$ compared to the standard ring resonator. This factor depends on the free spectral ranges and their differences, which can be tuned by changing the radius of both rings.

2.3.4 Optical waveguide lightmode spectroscopy (OWLS)

Optical waveguide lightmode spectroscopy is a method used to monitor the adsorption of molecules on a sensor surface[25,26]. OWLS sensors are based on evanescent field sensing but use a different detection principle than other commonly used refractive index sensors. However, it is still commonly used for refractive index applications and therefore included in this thesis. In an OWLS sensor, an optical waveguide grating is used to excite the guided mode of a planar waveguide. The incident light from a laser gets diffracted from the grating and starts propagating inside the waveguide (Fig. 2.5). This only occurs at two distinct incident angles for mono-mode waveguides represented by the two effective refractive indexes for the transverse electric ($n_{eff,TE}$) and the transverse magnetic ($n_{eff,TM}$) polarization modes. The effective refractive indexes can be found using the mode equation[26]. (eq. 2.9).

$$0 = \frac{2\pi}{\lambda} \sqrt{n_F^2 - n_{eff}^2} \times (d_F + \frac{n_A^2 - n_C^2}{n_F^2 - n_C^2} [\frac{(n_{eff}/n_c)^2 + (n_{eff}/n_A)^2 - 1}{(n_{eff}/n_c)^2 + (n_{eff}/n_F)^2 - 1}]^2 d_A) -$$
$$arctan[(\frac{n_F}{n_C})^{2\rho} \frac{\sqrt{n_{eff}^2 - n_C^2}}{\sqrt{n_F^2 - n_{eff}^2}}] - arctan[(\frac{n_F}{n_S})^{2\rho} \frac{\sqrt{n_{eff}^2 - n_S^2}}{\sqrt{n_F^2 - n_{eff}^2}}],$$

$$(2.9)$$

where $\rho = 0$ for TE and $\rho = 1$ for TM modes, n_{eff} is the effective refractive index, n_A, n_C, n_F, n_S, are refractive index of deposited adlayer, refractive index of cover medium, refractive index of waveguiding film, refractive index of supporting glass, respectively, d_F and d_A are thickness of waveguiding film and deposited adlayer, respectively.

Eq. 2.9 can be split into two separate equations depending on the value of ρ. Two equations (ρ=1 for the TM mode and ρ=0 for the TE mode) depend on the two effective refractive indexes (N), N_{TE} and N_{TM} ; which can be related to the in-coupling angles, α_{TE} and α_{TM}; respectively. These angles correspond to peaks in the light-mode spectrum according to,

$$n_{eff} = n \sin \alpha + l\lambda/\Lambda, \qquad (2.10)$$

where n is the refractive index of air, λ is the wavelength of the laser, Λ is the grating constant, n_{eff} is the effective refractive index and l is the diffraction order.

Continuously measuring the shift of these in-coupling angles allows the direct online monitoring of the adsorption of macromolecules above the grating without the need for any labeling procedure. The method is highly sensitive

(i.e., detection limits $< 1ng/cm^2$) up to a distance of a few hundred nanometers above the surface of the waveguide [26]. Furthermore, a measurement time resolution of seconds permits an in situ, real-time study of adsorption kinetics.
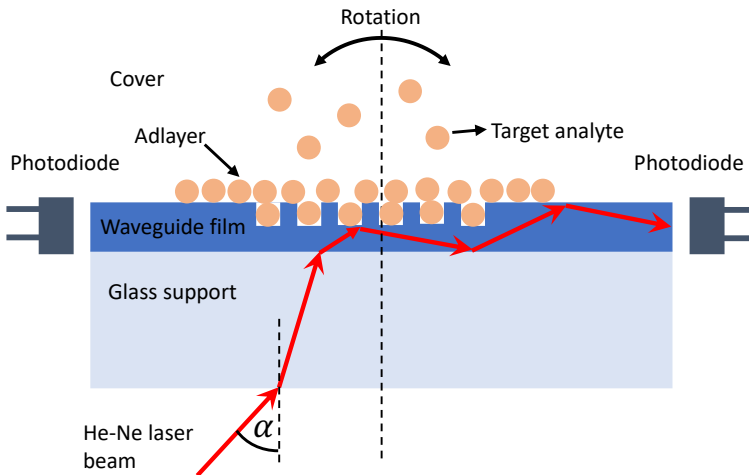
FIGURE 2.5. Schematic of an OWLS sensor.

2.3.5 *Subwavelength grating-based waveguide sensor*

Subwavelength grating (SWG) waveguides are based on the formation of subwavelength gratings in the waveguide core (Fig. 2.6). Subwavelength gratings are formed by periodically positioning high index and low-index materials (or air) at the subwavelength scale [27]. In contrast to conventional index-guided channel waveguides, a SWG waveguide core is a composite medium with subwavelength scale periodic openings between the high-index material. SWGs are theoretically transparent due to the small grating period compared to the wavelength. This combination of transparency and periodic absence of high-index material in SWGs allows an increase in interaction between the propagating light and the material present in the surounding and in the low-index region. This low refractive index region can also be air.

Most optical waveguide sensors are based on evanescent field sensing, i.e., they exploit the interaction between the evanescent tail of a guided mode and the analyte to produce a change in the effective index of the mode. In order to maximize the device sensitivity, it is important that the sensing waveguide provides a high overlap of the mode field with the analyte. The SWG waveguide provides an increase in interaction between the light and analyte due to its design with periodic open regions.
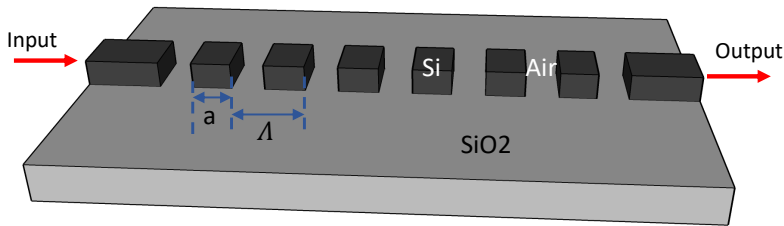
FIGURE 2.6. Schematic of a waveguide with subwavelength gratings.

In the case of optical refractive index sensors, the strength of light-matter interaction defines the change in the effective refractive index due to the analyte. The sensitivity of optical refractive index sensors using conventional waveguides can be further enhanced by utilizing SWGs. Several research studies have already been performed and are ongoing toward sensitivity enhancement using SWG in different sensor architectures[28–31].

2.3.6 The current advancements and technology trends

The above-mentioned sensor designs are conventional and the mostly used sensor architecture for academic and industrial development. In addition to these sensors, several other sensor architectures have been developed using plasmonic and photonic structures[4]. All these sensors are based on different detection mechanisms and possess specific merits and limitations.

Along with the sensors described in the previous section, a few commonly used sensor designs are listed in Table 2.1 and compared based on evaluation parameters detailed in Section 2.2.2. Most of these sensors are suitable for specific applications. Some sensors are ideal for highly sensitive measurements but have limited measurement ranges, while others have ultra-large measurement ranges but are less sensitive. There is still a need to develop a so-called multipurpose sensor that can be used for different applications. It should be cost-effective and possess high sensitivity, large measurement range, and multiplexing capability.

In recent times, Vernier, plasmonic and hybrid plasmonic-photonic sensor technologies have been emerging rapidly[3]. There are some recently developed sensors that offer both high sensitivity and large measurement range, such as Vernier-based sensors[32,33] and hybrid plasmonic-ring resonator sensors[34,35].

Despite their advantages, these sensors are not yet used commercially due to their bulky design or the need for high-precision measurement setups. For example, Vernier-based sensors require a high-precision spectrum analyzer, and hybrid plasmonic-ring resonator sensors exhibit similar limitations as ring resonators towards versatility and multiplexing capability.

To address these challenges, we developed a novel Mach-Zehnder interferometer assisted ring resonator configuration (MARC) sensor.

TABLE 2.1.   Comparison table (size, sensitivity, fabrication, multiplexing)

Sensor design	Sensitivity	Measurement range	Multiplexing	Size	Challenges
Standard ring resonator	100-300 nm/RIU[18–22]	Defined by free spectral range (FSR)	Requires sensor array (multiple input and output)	Very Small (30 um x30 um)	Works best with small rings, requires a laser with fast wavelength scan
2-cascaded ring resonator sensor	2,169 nm/RIU[23]	FSR of cascaded ring resonator	Requires sensor array (multiple input and output)	Bulky (Larger than 400 um x 150 um)	Large rings are required, high resolution measurement
Ring cascaded with MZI sensor	21,500 nm/RIU[24]	FSR of cascaded ring resonator	Requires sensor array (multiple input and output)	Bulky (Larger than 1000 um x 500 um)	Large rings are required, high resolution measurement
Mach-Zehnder interferometer	100-800 nm/RIU[11,12]	2π phase shift	Requires sensor array	Bulky (Sensitivity scales with length)	Fast and high-resolution detection
OWLS	16°/RIU[25,26]	Defined by incident angle causing coupling	Requires sensor array	Bulky (Require moving parts)	High-resolution rotation (mechanical movement of source) and detection

2.3.7   *MARC sensor*

The Mach-Zehnder interferometer-assisted ring resonator configuration sensor is a novel optical waveguide-based refractive index sensor. It consists of a balanced Mach-Zehnder interferometer and an add-drop ring resonator, illustrated in Figure 2.7. The ring resonator acts as a sensing element. The
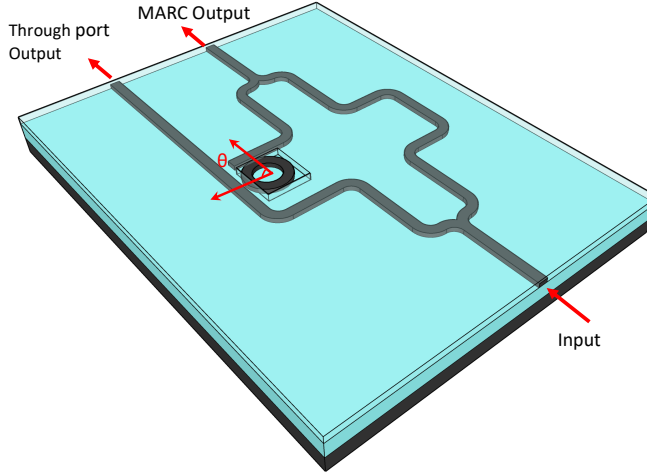
FIGURE 2.7. Schematic of a MARC sensor with an arbitrary angular separation of θ.

balanced interferometer in this configuration converts the phase response at the ring resonator drop port into an intensity response. The phase response at the drop port is engineered by physically changing the angular separation between the drop port and the through port. The engineered phase response is translated into the transmission response by the balanced MZI. Transmission spectra obtained from varying the angular separation are unique and provide large effective free spectral ranges. The device principle is discussed in detail in the next chapter.

The sensitivity of a MARC sensor is exactly the same as a ring resonator sensor. It is defined as resonance wavelength shift w.r.t the change in the surrounding refractive index, and it is given as:

$$S = \frac{\Delta\lambda_{res}}{\Delta n},\tag{2.11}$$

where, $\Delta\lambda_{res}$ is the resonance wavelength shift and Δn is the surrounding refractive index change.

However, in contrast to a ring resonator, the measurement range of a MARC sensor is given as (defined in section 2.2.2), $\Delta n_{max} = \frac{FSR_e}{S}$, where FSR_e is the effective free spectral range of the MARC output. FSR_e of the MARC sensor is defined as $N \cdot FSR$, where N is an integer, and its value is dependent on the angular separation between the drop port and the through port. This makes the measurement range of a MARC sensor tunable and large compared to a ring resonator sensor. It is explained in detail in the next chapter.

TABLE 2.2.   Comparison table for MARC

Sensor design	Sensitivity	measurement range	Multiplexing	Size	Challenges
MARC sensor	100-300 nm/RIU, and can be enhanced with larger rings and chemical amplification	Integer times RR FSR	Single sensor with multiple RRs can be used to detect 2-3 analytes (no need for multiple input and output)	Small, 2-3 sensors in smaller than 400 um x 300 um area	Signal processing to demultiplex signal.

2.4   LAB-ON-A-CHIP INTEGRATION

An optical sensor chip is a component in an integrated sensing platform which can be used for biosensing or chemical sensing applications. The integrated sensing platform is generally referred to as a Lab-on-a-chip (LOC) platform/system. LOC systems are made up of several subsystems. A systematic approach is required to integrate these subsystems into a LOC system. Fig. 2.6 depicts a schematic of an ideal LOC system including a multiplexed optical sensor, coupling components, and microfluidics. In addition to these components, electronic and software systems are used for measurement data acquisition and analysis, and the optical system including the laser and detectors are used for excitation and detection.
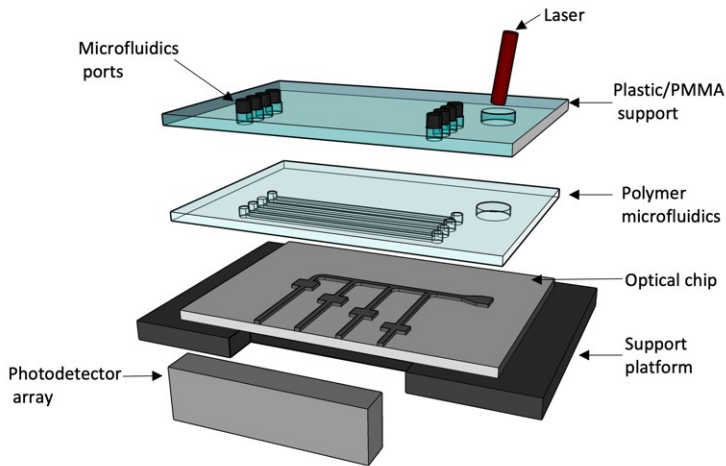
FIGURE 2.8. Schematic of an integrated packaged sensor chip with microfluidics.

In LOC systems, microfluidics is an important component. Microfluidics are used for controlled delivery of fluids over the sensor to perform biofunctionalization of the sensor surface and sensing. The microfluidic layer is generally made up of soft polymer material and the soft-lithography process is used to create channels in the polymer layer for fluid flow. It can be bonded irreversibly or reversibly to the sensor chip. Traditional bonding methods are usually irreversible; however, some microfluidic applications require reversible bonding for chip reusability. Biocompatible bonding and less gas permeability are two important challenges that need to be addressed when using microfluidics. These two features are required to keep sensor chips reusable and avoid gas bubbles during experiments, respectively.

2.5 REFERENCES

[1] Stewart E Miller. Integrated optics: An introduction. *The Bell system technical journal* **48** (7), 2059–2069 (1969). Cited on page/s 5.

[2] Donald L. Lee. Electromagnetic principles of integrated optics. Wiley (1986). Cited on page/s 5.

[3] Yi Xu, Ping Bai, Xiaodong Zhou, Yuriy Akimov, Ching Eng Png, Lay-Kee Ang, Wolfgang Knoll, and Lin Wu. Optical refractive index sensors with plasmonic and photonic structures: promising and inconvenient truth. *Advanced Optical Materials* 7 (9), 1801433 (2019). Cited on page/s 6, 14.

[4] M Carmen Estevez, Mar Alvarez, and Laura M Lechuga. Integrated optical devices for lab-on-a-chip biosensing applications. *Laser & Photonics Reviews* **6** (4), 463–487 (2012). Cited on page/s 6, 14.

[5] Adam Densmore, D-X Xu, Philip Waldron, Siegfried Janz, Pavel Cheben, J Lapointe, André Delâge, Boris Lamontagne, JH Schmid, and Edith Post. A silicon-on-insulator photonic wire based evanescent field sensor. *IEEE Photonics Technology Letters* **18** (23), 2520–2522 (2006). Cited on page/s 6.

[6] Enxiao Luan, Hossam Shoman, Daniel M Ratner, Karen C Cheung, and Lukas Chrostowski. Silicon photonic biosensors using label-free detection. *Sensors* **18** (10), 3519 (2018). Cited on page/s 6.

[7] Hans-Peter Loock and Peter D Wentzell. Detection limits of chemical sensors: Applications and misapplications. *Sensors and Actuators B: Chemical* **173**, 157–163 (2012). Cited on page/s 7.

[8] Daniel MacDougall, Warren B Crummett, *et al.* Guidelines for data acquisition and data quality evaluation in environmental chemistry. *Analytical Chemistry* **52** (14), 2242–2249 (1980). Cited on page/s 7.

[9] Vimala Rani Samuel and K Jagajjanani Rao. A review on label free biosensors. *Biosensors and Bioelectronics: X* page 100216 (2022). Cited on page/s 7.

[10] Daoxin Dai. Highly sensitive digital optical sensor based on cascaded high-q ring-resonators. *Optics Express* **17** (26), 23817–23822 (2009). Cited on page/s 7.

[11] RG Heideman and PV Lambeck. Remote opto-chemical sensing with extreme sensitivity: design, fabrication and performance of a pigtailed integrated optical phase-modulated Mach-Zehnder interferometer system. *Sensors and Actuators B: Chemical* **61** (1-3), 100–127 (1999). Cited on page/s 7, 8, 9, 15.

[12] RG Heideman, RPH Kooyman, and Jan Greve. Performance of a highly sensitive optical waveguide Mach-Zehnder interferometer immunosensor. *Sensors and Actuators B: Chemical* **10** (3), 209–217 (1993). Cited on page/s 7, 8, 15.

[13] Francisco Prieto, Borja Sepúlveda, A Calle, Andreu Llobera, Carlos Domínguez, Antonio Abad, A Montoya, and Laura M Lechuga. An integrated optical interferometric nanodevice based on silicon technology for biosensor applications. *Nanotechnology* **14** (8), 907 (2003). Cited on page/s 7, 8.

[14] Firehun Tsige Dullo, Susan Lindecrantz, Jana Jágerská, Jørn H Hansen, Magnus Engqvist, Stian Andre Solbø, and Olav Gaute Hellesø. Sensitive on-chip methane detection with a cryptophane-a cladded Mach-Zehnder interferometer. *Optics Express* **23** (24), 31564–31573 (2015). Cited on page/s 7, 8.

[15] Dengpeng Yuan, Ying Dong, Yujin Liu, and Tianjian Li. Mach-Zehnder interferometer biochemical sensor based on silicon-on-insulator rib waveguide with large cross section. *Sensors* **15** (9), 21500–21517 (2015). Cited on page/s 7, 8.

[16] Laura M Lechuga, ATM Lenferink, RPH Kooyman, and J Greve. Feasibility of evanescent wave interferometer immunosensors for pesticide detection: chemical aspects. *Sensors and Actuators B: Chemical* **25** (1-3), 762–765 (1995). Cited on page/s 7, 8.

[17] EF Schipper, AM Brugman, C Dominguez, Laura M Lechuga, RPH Kooyman, and J Greve. The realization of an integrated Mach-Zehnder waveguide immunosensor in silicon technology. *Sensors and Actuators B: Chemical* **40** (2-3), 147–153 (1997). Cited on page/s 7, 8.

[18] Katrien De Vos, Irene Bartolozzi, Etienne Schacht, Peter Bienstman, and Roel Baets. Silicon-on-insulator microring resonator for sensitive and label-free biosensing. *Optics Express* **15** (12), 7610–7615 (2007). Cited on page/s 7, 9, 15.

[19] Carl Fredrik Carlborg, *et al.* A packaged optical slot-waveguide ring resonator sensor array for multiplex label-free assays in labs-on-chips. *Lab on a Chip* **10** (3), 281–290 (2010). Cited on page/s 7, 9, 15.

[20] Adam L Washburn, L Cary Gunn, and Ryan C Bailey. Label-free quantitation of a cancer biomarker in complex media using silicon photonic microring resonators. *Analytical Chemistry* **81** (22), 9499–9506 (2009). Cited on page/s 7, 9, 15.

[21] Alexander Ksendzov and Yangyang Lin. Integrated optics ring-resonator sensors for protein detection. *Optics Letters* **30** (24), 3344–3346 (2005). Cited on page/s 7, 9, 15.

[22] Chung-Yen Chao and L Jay Guo. Biochemical sensors based on polymer microrings with sharp asymmetrical resonance. *Applied Physics Letters* **83** (8), 1527–1529 (2003). Cited on page/s 7, 9, 15.

[23] Tom Claes, Wim Bogaerts, and Peter Bienstman. Experimental characterization of a silicon photonic biosensor consisting of two cascaded ring resonators based on the Vernier-effect and introduction of a curve fitting method for an improved detection limit. *Optics Express* **18** (22), 22747–22761 (2010). Cited on page/s 7, 11, 15.

[24] Xianxin Jiang, Yangqing Chen, Fang Yu, Longhua Tang, Mingyu Li, and Jian-Jun He. High-sensitivity optical biosensor based on cascaded Mach-Zehnder interferometer and ring resonator using vernier effect. *Optics Letters* **39** (22), 6363–6366 (2014). Cited on page/s 7, 11, 15.

[25] András Székács, Nóra Adányi, Inna Székács, Krisztina Majer-Baranyi, and István Szendrő. Optical waveguide light-mode spectroscopy immunosensors for environmental monitoring. *Applied Optics* **48** (4), B151–B158 (2009). Cited on page/s 7, 12, 15.

[26] J Vörös, JJ Ramsden, G Csucs, I Szendrő, SM De Paul, M Textor, and ND Spencer. Optical grating coupler biosensors. *Biomaterials* **23** (17), 3699–3710 (2002). Cited on page/s 7, 12, 13, 15.

[27] Przemek J Bock, Pavel Cheben, Jens H Schmid, Jean Lapointe, André Delâge, Siegfried Janz, Geof C Aers, Dan-Xia Xu, Adam Densmore, and Trevor J Hall. Subwavelength grating periodic structures in silicon-on-insulator: a new type of microphotonic waveguide. *Optics Express* **18** (19), 20251–20262 (2010). Cited on page/s 13.

[28] Jonas Flueckiger, Shon Schmidt, Valentina Donzella, Ahmed Sherwali, Daniel M Ratner, Lukas Chrostowski, and Karen C Cheung. Sub-wavelength grating for enhanced ring resonator biosensor. *Optics Express* **24** (14), 15672–15686 (2016). Cited on page/s 14.

[29] R Sumi, Nandita Das Gupta, and Bijoy Krishna Das. Integrated optical Mach-Zehnder interferometer with a sensing arm of sub-wavelength grating waveguide in soi. In *2017 IEEE SENSORS* pages 1–3. IEEE (2017). Cited on page/s 14.

[30] Hai Yan, Lijun Huang, Xiaochuan Xu, Swapnajit Chakravarty, Naimei Tang, Huiping Tian, and Ray T Chen. Unique surface sensing property and enhanced sensitivity in microring resonator biosensors based on subwavelength grating waveguides. *Optics Express* **24** (26), 29724–29733 (2016). Cited on page/s 14.

[31] Lijun Huang, Hai Yan, Xiaochuan Xu, Swapnajit Chakravarty, Naimei Tang, Huiping Tian, and Ray T Chen. Improving the detection limit for on-chip photonic sensors based on subwavelength grating racetrack resonators. *Optics Express* **25** (9), 10527–10535 (2017). Cited on page/s 14.

[32] Yong Liu, Yang Li, Mingyu Li, and Jian-Jun He. High-sensitivity and wide-range optical sensor based on three cascaded ring resonators. *Optics Express* **25** (2), 972–978 (2017). Cited on page/s 14.

[33] Paul Azuelos, Pauline Girault, Nathalie Lorrain, Luiz Poffo, Mohammed Guendouz, Monique Thual, Jonathan Lemaitre, Parastesh Pirasteh, Isabelle Hardy, and Joël Charrier. High sensitivity optical biosensor based on polymer materials and using the vernier effect. *Optics Express* **25** (24), 30799–30806 (2017). Cited on page/s 14.

[34] Xu Sun, Daoxin Dai, Lars Thylén, and Lech Wosinski. Double-slot hybrid plasmonic ring resonator used for optical sensors and modulators. In *Photonics* volume 2 pages 1116–1130. MDPI (2015). Cited on page/s 14.

[35] Darius Urbonas, Armandas Balčytis, Martynas Gabalis, Konstantinas Vaškevičius, Greta Naujokaitė, Saulius Juodkazis, and Raimondas Petruškevičius. Ultra-wide free spectral range, enhanced sensitivity, and removed mode splitting soi optical ring resonator with

dispersive metal nanodisks. *Optics Letters* **40** (13), 2977–2980 (2015). Cited on page/s 14.

CHAPTER 3

Theoretical analysis and experimental method

In the initial stages of my Ph.D., I studied an all-optical Mach-Zehnder interferometer (MZI) sensor using SWG, with the aim of improving sensitivity and reducing measurement ambiguity in Mach-Zehnder interferometer-based sensors. Although the theoretical analysis yielded promising results, the experimental work highlighted the challenge of fabricating low-loss SWG waveguides. Nonetheless, knowledge gained about the phase modulation from this research encouraged the study of the Mach-Zehnder interferometer-assisted ring resonator configuration, which became the primary focus of my Ph.D. research.

3.1 MACH-ZEHNDER INTERFEROMETER SENSOR UTILIZING SUBWAVELENGTH GRATINGS

3.1.1 *Basic principle*

In this study, a conventional MZI sensor was designed with the inclusion of SWGs in its arms. 2D Finite element method simulations using COMSOL were performed on different designs of MZI with SWGs to study refractive index change sensitivity and modulation frequency.

The Mach-Zehnder interferometer sensor is a widely-used optical waveguide sensor design because of its simplicity and high sensitivity [1-3]. The detailed description of a MZI sensor can be found in section 2.3.1. The output intensity of the Mach-Zehnder interferometer is periodic in relation to the phase difference between the guided modes travelling in both arms, and can be expressed as:

$$I = I_s + I_r + 2\sqrt{I_s I_r} \cos \Delta\phi_s(t), \tag{3.1}$$

The phase difference depends on the arm length and difference in effective refractive index of the guided mode in both arms,

$$\Delta\phi_s(t) = 2\pi\frac{L}{\lambda}(n_{eff,s}(t) - n_{eff,r}), \tag{3.2}$$

where $\Delta\phi_s(t)$ is the phase difference between the mode propagating in the two arms, λ is the coupled wavelength, L is the interaction length, $n_{eff,r}$ and
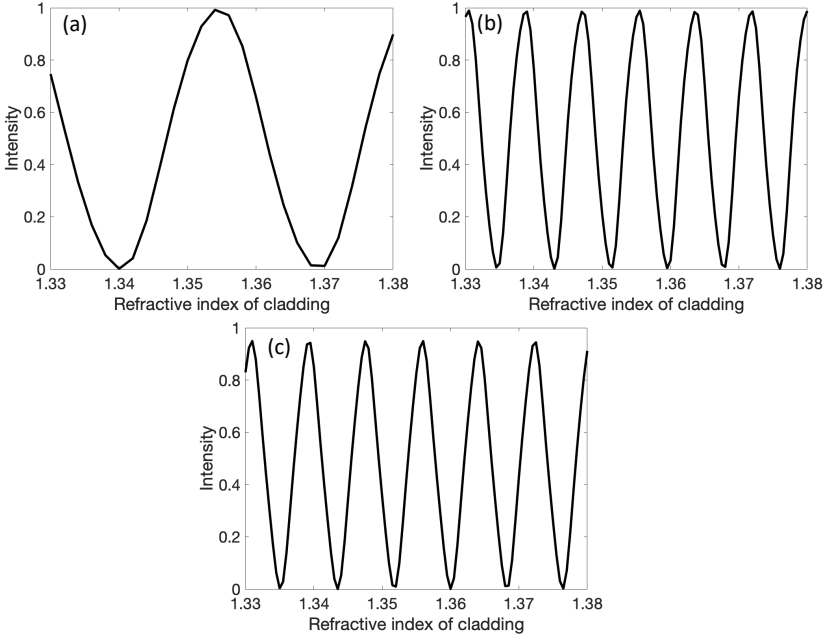
FIGURE 3.1. COMSOL simulated output intensity vs sensing arm cladding refractive index for (a) MZI without SWGs, (b) MZI with 3044 SWGs in the sensing arm, and (c) MZI with 3044 SWGs in both arms.

$n_{eff,s}(t)$ are the effective refractive indices of the guided mode in the reference arm and the sensing arm, respectively.

Eq. 3.1 shows that the MZI output is periodic with the phase change induced by the refractive index change. This periodic nature of the output can lead to false readings or ambiguous results. This is due to phase ambiguity and sensitivity fading as shown in Fig. 2.2 [1]. A phase modulation technique is commonly used to overcome these issues. The basic requirement for this technique is the generation of the modulation signal with a higher frequency than the sensor signal. However, this approach requires electrodes and an electrical circuit, which complicates fabrication and integration with microfluidics. The wavelength modulation technique can be a better alternative as it does not require electrodes or electrical circuits, simplifying fabrication and enabling miniaturization [4]. It involves the use of a tunable laser to induce wavelength-dependent phase modulation in the interferometer. The wavelength dependent phase modulation is given as:

$$\delta(\Delta\phi_s) = \frac{2\pi}{\lambda}[-\frac{1}{\lambda}(n_{eff,s} - n_{eff,r}) + \frac{\partial(n_{eff,s} - n_{eff,r})}{\partial\lambda}]L\delta\lambda. \qquad (3.3)$$

A subwavelength grating waveguide is a composite medium with subwavelength scale periodic openings between the high-index material[5]. SWGs are theoretically transparent due to the small grating period compared to the wavelength. This combination of transparency and periodic open areas between the high-index material in SWG allows an increase in interaction between the propagating light and the material present in the surrounding and in the low-index region. This architecture is generally used with conventional refractive index sensors to enhance sensitivity[6–9]. Moreover, due to the increase in interaction strength with the surrounding material, SWG waveguide can be used to shorten the wavelength change required to induce specific phase change for the phase modulation.

To study the effect of SWGs on the MZI response, finite element method (FEM) simulations were performed on three designs, namely MZI with SWGs in the sensing arm, MZI with SWGs in both arms, and MZI with no SWGs. MZIs were designed using silicon waveguides supporting single TE mode. The MZI arms were $761 \ \mu m$ long. The reference arm of MZI in all designs was covered with SU8 (n=1.57). However, the refractive index of the sensing arm cladding layer was tuned between 1.33 and 1.38 for sensitivity analysis and kept constant in air (n=1) for modulation analysis. Subwavelength gratings with a 250 nm period and 60% duty cycle were included in the interferometer arms.

To investigate the sensitivity to refractive index change of these designs , the reference cladding was kept constant while the sensing arm cladding's refractive index was tuned between 1.33 and 1.38. The resulting MZI output intensity was then estimated. The simulated MZI output intensity for both designs with SWGs was compared to that of a conventional MZI, as displayed in Fig. 3.1.

As shown in Fig. 3.1, the sensitivity of a MZI sensor can be enhanced by three times by adding SWGs gratings in its sensing arm. Furthermore, the sensitivity of an interferometer can also be increased by three times when SWGs are present in both arms, as compared to the conventional MZI.

To study the wavelength dependent phase modulation, the MZI output intensity was estimated for all three designs by tuning the wavelength of the coupled light. For phase modulation analysis, the reference arm was covered with SU8 and the sensing arm with air for both designs. Fig. 3.2 presents the MZI output intensity response with respect to the wavelength.

As shown in Fig. 3.2, the conventional MZI requires a larger wavelength change to achieve a 2π phase shift, compared to the MZI with SWGs. The MZI with SWGs in both arms requires 50% less wavelength change to achieve the same phase change. However, when SWGs are only present in the sensing arm, a much lower wavelength change is required for a 2π phase shift, but the intensity (phase) versus wavelength over a large range is non-uniform as shown
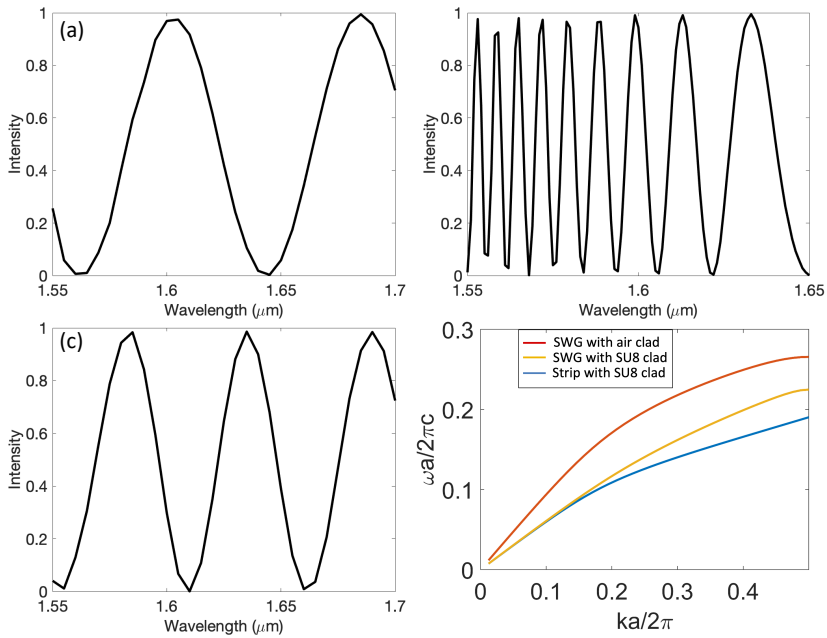
FIGURE 3.2. (a) COMSOL simulated MZI output intensity vs wavelength, (a) MZI without SWGs, (b) MZI with 3044 SWGs in the sensing arm, (c) MZI with 3044 SWGs in both arms, and (d) MPB simulated frequency vs wave vector dispersion curve for lattice constant of $250\ nm$. (k is the waveguide propagation constant.)

in Fig. 3.2 (b).

To further study the effect of SWGs on dispersion, MIT photonic band gap (MPB) simulations were performed. MPB is a technique that utilizes Maxwell's equations to identify the frequency eigenstates for arbitrary propagation constant. MPB simulations were performed on silicon-based SWGs and strip waveguides with different claddings. The resulting dispersion relation is shown in Fig.3.2 (d). This shows that SWGs have higher dispersion than strip waveguides. The slope difference between the strip and SWGs due to the difference in dispersion explains the non-uniform modulated signals. This is evident from eq. 3.3, where the second term becomes non-negligible for the sensor with a strip waveguide in one arm and SWGs in the other arm, which results in a signal with non-uniform frequency over a wavelength range.

3.1.2   *Sensor design and fabrication*

Three different combinations of MZI with SWGs were designed to investigate modulation and sensitivity. All three designs featured MZI with 4 *mm* arm lengths and utilized 220 *nm* thick and 500 *nm* wide strip waveguides that supported single TE guided mode. The first design was a simple MZI with a 4 *mm* arm length and no SWGs. The second design was an MZI with 100 periods of SWGs embedded in the sensing arm, and the third design was an MZI with 100 periods of SWGs embedded in both arms. The SWGs were created with a 250 *nm* period and a duty cycle of 60%. Fabricated SWGs are shown in Fig. 3.3.

These devices were fabricated on a SOI platform made of amorphous silicon. The process began with depositing a layer of 220 *nm* high amorphous silicon on a 1 *μm* thick layer of thermal oxide on a silicon substrate using plasma-enhanced chemical vapor deposition (PlasmaLab System 100-PECVD). The MZI with SWG designs were then fabricated on SOI using electron beam lithography (Elionix ELS G100). To do this, a thin layer of 200 *nm* Allresist AR-P 6200 was spin-coated onto an SOI chip and baked at 150 degrees Celsius for 1 minute. The baked electron beam resist was then exposed with the Elionix ELS-G100 system to create the waveguide pattern, using a beam current of 500 *pA*. After exposure, the chip was developed in AR 600-546 for 1 minute, followed by 1 minute oxygen plasma. An inductively coupled plasma reactive ion etching (ICP-RIE) chiller was used to etch the amorphous silicon layer through the resist mask to generate the sensor design. Once etching was complete, the sample was cleaned using AR 600-71 to remove any remaining resist.
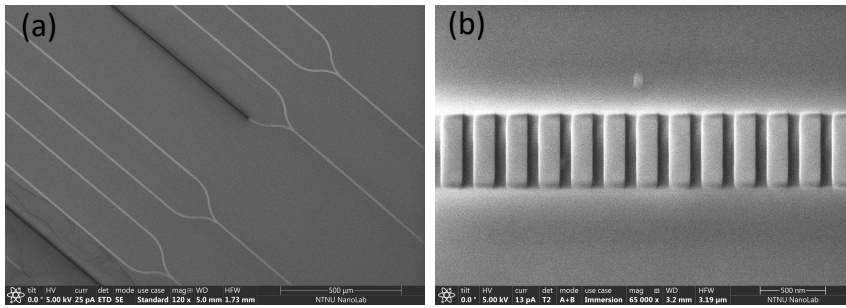
FIGURE 3.3. Scanning electron microscopy (SEM) image of fabricated (a) MZIs, and (b) Sub-wavelength gratings.

3.1.3 Experimental set-up and characterization

To carry out experimental characterization, a photonic chip with several designs of MZI with SWGs was placed on a translational stage. An external cavity laser (Thorlabs TLK L-1550M) with a central wavelength of 1550 nm was used as the light source. To couple light from an external cavity laser into the waveguide, a tapered lensed fiber with a spot diameter of 2.5 μm and a working distance of 14 μm purchased from OZ-optic was utilized. In order to enhance the coupling to the TE-like mode of the waveguides and regulate the polarization of the light from the laser source, a polarization controller (Thorlabs FPC562) was utilized. To capture the optical power from the MZI output, a cleaved single-mode optical fiber was coupled to the MZI output and connected to an InGaAs photodetector (Thorlabs DET10C2). Lastly, a LabView program was employed to collect the output power and tune the laser wavelength.

The preliminary measurement results obtained from the MZI with 100 periods of SWGs show promising results. However, the wavelength dependent phase modulation for all three designs was found to be the same. The main reason for this behaviour is that in the simulations, the sensing arm is completely replaced with SWGs but in the fabricated architecture, SWGs replace only less than 1% of the sensing arm. Therefore, the effective refractive index due to the strip waveguide is dominant over the SWGs and results in the same response as for the strip waveguide. To further improve the sensitivity and the wavelength dependent phase modulation frequency, the number of SWGs in the MZI designs were increased. Low transmission was observed in the fabricated MZI with a large number of SWGs in its arm. These results are reported in paper IV.

3.2 MARC SENSOR THEORETICAL ANALYSIS
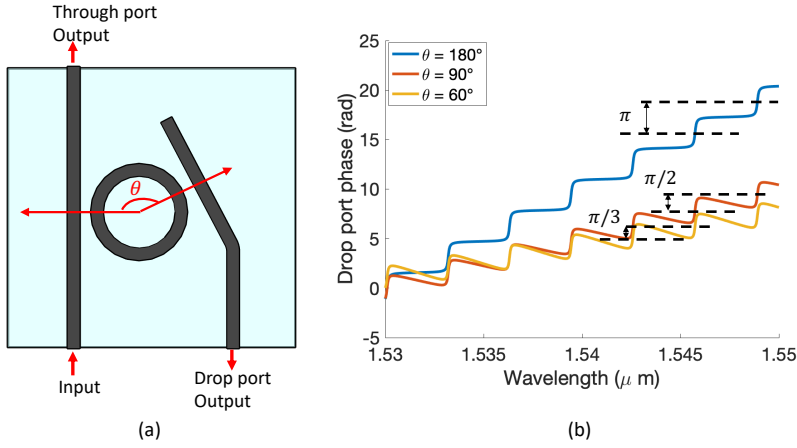
FIGURE 3.4. (a) Schematic of a ring resonator with an arbitrary angular separation of θ, (b) phase response at the drop port for different angular separations.

3.2.1 Basic principle

A MARC device comprises a balanced MZI and an add-drop ring resonator, as shown in Fig. 2.7. The basic principle behind this configuration is to study the phase response at the ring resonator drop port and the corresponding intensity response.

To analyze the drop port phase response, we first consider a ring resonator (RR) with an arbitrary angular separation, θ, and investigate the effect of the angular separation on the drop port phase response. A ring resonator with varying angular separation is shown in Fig. 3.4(a). The amplitude transmission response, t, and phase of the transmitted light at the drop port, ϕ, of a RR with an arbitrary angular separation are given as:

$$\phi = arctan\frac{Im[t]}{Re[t]} = \pi + \psi\frac{\theta}{2\pi} + arctan\frac{\gamma_1\gamma_2\sin\psi}{1 - \gamma_1\gamma_2 a\cos\psi}, \qquad (3.4)$$

$$t = \frac{\sqrt{1 - \gamma_1^2}\sqrt{1 - \gamma_2^2}a_d\exp-j(\psi\frac{\theta}{2\pi})}{1 - \gamma_1\gamma_2 a\exp-j\psi}, \qquad (3.5)$$

where $\psi(= \frac{\omega}{c}n_{eff}(2\pi r))$ is the round-trip phase shift, n_{eff} is the effective refractive index, r is the ring radius, a is the single-pass amplitude transmission factor, $\gamma_1(\gamma_2)$ is the self-coupling coefficient of the coupler and a_d is the fraction of the round-trip amplitude transmission factor between the input and output coupler.
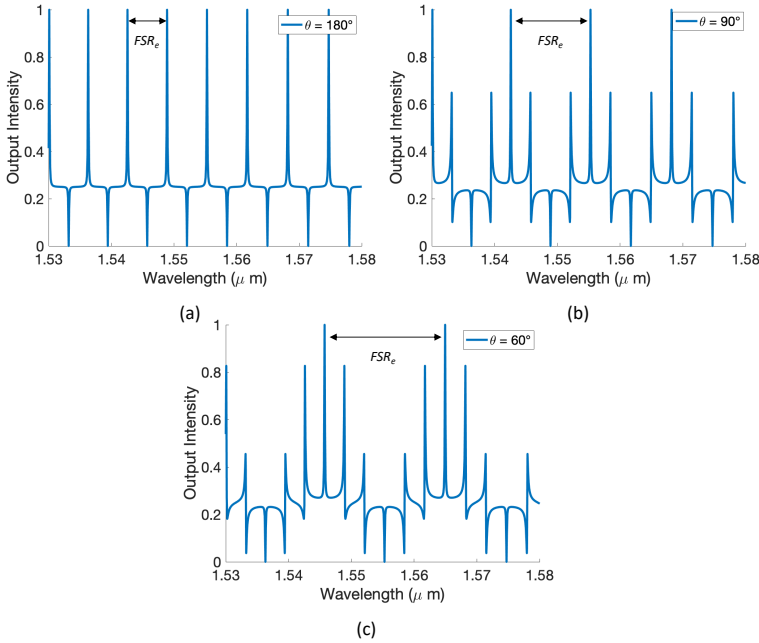
Figure 3.5. Transmission spectra of the MARC with angular separations of 180°, 90°, and 60°.

Figure 3.4(b) displays the phase response at the drop port for various angular separations. A traditional add-drop resonator setup with an angular separation of 180° yields a gradual increase in phase as the wavelength changes. This results in a π radians phase accumulation between resonances. However, if the angular separation is decreased to 90°, the accumulated phase difference drops to $\pi/2$ radians. Further reducing it to 60° leads to a decrease in the accumulated phase difference to $\pi/3$ radians. By selecting a specific angular separation, it is possible to control the phase response at the drop port. This control depends on both the angular separation and wavelength. To simplify the numerical analysis, it is assumed that all ring resonators are identical, with a radius of $30\mu m$, and are lossless with a coupling coefficient of 1. Additionally, the resonators are critically coupled with $\gamma_1 = \gamma_2$.

In the MARC, the balanced MZI converts the phase change introduced by resonances at the drop port into a transmission intensity (Figure 2.7). The intensity transmission response, T_{out}, obtained from the MARC can be expressed as [10]:

$$T_{out} = \frac{1}{4}[1 + |t|^2 + 2|t|\cos\phi].$$

(3.6)

The findings of the study presented in Figure 3.5 show three distinct transmission spectra with varying angular separations, namely 180°, 90°, and 60°. The transmission spectrum for an angular separation of 180° displays two distinct resonance lineshapes separated by a 3 *nm* free spectral range. These lineshapes are identified as interference maxima and minima with Lorentzian and inverse Lorentzian shapes. Meanwhile, when the angular separation is at 90°, the transmission spectrum exhibited three different resonance lineshapes, namely Lorentzian, inverse Lorentzian, and Fano-like shapes. The Fano-like lineshape is located in the middle of the Lorentzian and inverse Lorentzian lineshapes due to interference. The transmission spectrum for an angular separation of 60° presents four distinct resonance lineshapes, two of which have asymmetric Fano-like shapes.

Based on the aforementioned results, the study concludes that the number of distinctive resonance lineshapes in a transmission spectrum decreases as the angular separation increases. This discovery offers a unique spectral signature within a relatively narrow band by designating a specific angular separation for a transmission spectrum with multiple distinct resonance lineshapes. Overall, the data presented in Figure 3.5 provides valuable insight into the behavior of transmission spectra at varying angular separations and contributes to the further understanding of interference and resonance phenomena.

The resonance lineshape repeats itself when the accumulated phase reaches an integer multiple of 2π. This results in a transmission spectrum with a certain period, defined as the effective free spectral range (FSR_e). The FSR_e is related to the free spectral range (FSR) of the given ring resonator. The FSR is defined as the separation between two consecutive resonances and is given by $\frac{\lambda^2}{2\pi r n_g}$, where n_g is the group index, λ is the vacuum wavelength and r is the ring radius. For a given angular separation ($\theta = 2\pi/L$), the FSR_e of a transmission spectrum can be expressed as,

$$FSR_e = N \cdot FSR, \tag{3.7}$$

where N satisfies the condition $\theta = 2\pi \frac{M}{N}$, where N and M are integers that can be solved for L by setting $L = N/M$. There are two possible solutions. If L is a rational number in irreducible fraction form ($L = \frac{p}{q}$), then $N = p$ and $M = q$. If L is a positive integer, then $N = L$ and $M = 1$.

The positive integer N determines the effective free spectral range (FSR_e) for a given angular separation. As the angular separation decreases, the value of N increases, resulting in an increase in the FSR_e. In Figure 3.5, the FSR_e for 60° is calculated to be 18 *nm*, which is 6 times larger than the FSR of 3 *nm* for a conventional RR.
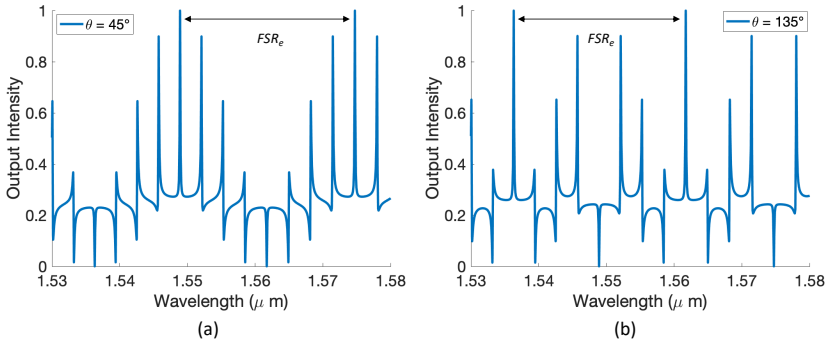
FIGURE 3.6. Transmission spectra of the MARC with angular separations of 45°, and 135°.

In Figures 3.6(a) and (b), the spectra of 45° and 135° have the same FSR_e of $24nm$ but exhibit noticeable differences due to the accumulated phase shift between the resonances. For the 135° case, the resonances occur with a phase shift of $3/8\,\pi$ radians, which is three times larger than that of the 45° case. This difference distinguishes one transmission spectrum from another. However, both cases require the same number of phase-shift steps to achieve a total phase accumulation of an integer multiple of 2π and have the same FSR_e. Thus, this process can produce a unique spectral signature and an extended effective free spectral range.

3.2.2 Sensing principle

When there is a change in the refractive index of the area surrounding the ring resonator, it causes a shift in resonance. These shifts can be measured through both the through port output and the MARC output, and they are proportional to the change in refractive index. The resonance shifts measured from both outputs are similar, but the MARC output is better for tracking large resonance shifts, while the through port output provides more precise positions of resonances. This is because the through port output provides resonances with a higher Q-factor and the line shapes of resonances are not affected by interference, making resonance tracking more accurate than the interference-based MARC output. The sensitivity that shows the resonance shift based on the refractive index change can be obtained from both the through port and the MARC output.

$$S = \frac{\Delta\lambda}{\Delta n} = \frac{m}{L}\left(\frac{\partial n_{eff}}{\partial n_{bulk}}\right)^{-1}, \tag{3.8}$$

where, L is the round-trip length of the ring, m is the cavity mode order, n_{bulk} is the bulk refractive index due to the analyte and n_{eff} is the effective refractive index of the guided mode.

Besides sensitivity, the measurement range of a sensor is also crucial in determining its usefulness and flexibility. In the case of the MARC sensor, the measurement ranges of the through-port output and the MARC output are not the same. The measurement ranges for both the through port and MARC outputs are given by,

$$\Delta n_{max}{}^{Through} = \frac{FSR}{S} \tag{3.9}$$

$$\Delta n_{max}{}^{MARC} = \frac{FSR_e}{S} \tag{3.10}$$

where, Δn_{max} is the maximum detectable change in refractive index and FSR is the free spectral range of the ring resonator. FSR_e is the effective free spectral range of the MARC output.

The equations reveal that the through-port output has a restricted measurement range due to the free spectral range. However, the MARC output has a measurement range that can be increased by increasing the effective free spectral range FSR_e, which can be controlled by changing the angular separation. Figure 3.7 demonstrates the contrast between the measurement range from the through port output and the MARC output, highlighting how the MARC output improves the measurement range.
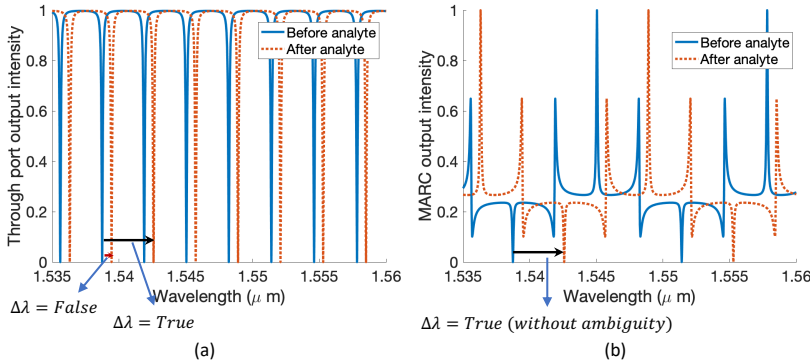
FIGURE 3.7. (a) Resonance shift measurement using the through port output, (b) Resonance shift measurement using the MARC output. The transmission response obtained from the through port output presents a case of false positives when the shift is abrupt and larger than the FSR, which is not present in the MARC response shown.

When considering the best multiplexing options, it is important to take into account sensors with large measurement ranges and distinguishable transmission responses. In the case of a standard ring resonator sensor, the measurement

range is dependent on the free spectral range, which can be increased by reducing the ring radius. However, this reduction can lead to a lower Q-factor of the ring resonator. Moreover, transmission spectra from ring resonators show repetitive resonances with similar line shapes, which makes the multiplexing of ring resonators challenging. On the other hand, a MARC sensor with a specific angular separation effectively enhances the effective free spectral range of the ring resonator without any negative impact on the Q-factor. Additionally, a MARC sensor can create a transmission response with a unique spectral signature, which is another advantageous feature. Both of these capabilities can be used for multiplexed sensing by integrating different rings with varying angular separations, along with a balanced Mach-Zehnder interferometer. This approach can lead to a versatile and effective multiplexing system, which can be utilized in a wide range of applications.

3.2.3 Sensor design and fabrication

1-ring MARC sensor

MARC sensor devices were designed with silicon strip waveguides with balanced MZIs and ring resonators, operating in the telecommunication wavelength band. Firstly, to experimentally verify the generation of unique spectral signatures from MARC, five different angular separations, ranging from 30°to 180°, were used to design the MARC with a single ring resonator. Ring resonators were designed with a radius of 30 μm, and a coupling gap between the ring and the bus waveguides of 150 nm. Silicon strip waveguides were 500 nm wide and 220 nm high to support the fundamental TE-like mode at the source wavelength of 1550 nm. For waveguide input and output coupling, inverted tapered silicon waveguides were used to enhance the coupling efficiency. Inverted taper silicon waveguides were 300 μm long with starting width of 70 nm.

For sensing applications, three 1-ring MARC sensors were designed with different angular separations and ring radii, as displayed in Figure 3.8. One sensor had a 180°angular separation and a 25 μm ring radius (Figure 3.8(a)), while the second had a 135°angular separation and a 45 μm ring radius (Figure 3.8(b)). The last sensor was designed with a 90°angular separation and a 35 μm ring radius (Figure 3.8(c)). All three sensors had a coupling gap of 150 nm between the ring and bus waveguides. The basic requirement of a MARC sensor is the balanced MZI. To ensure that the MZI remained balanced in each of the 1-ring MARC sensors, the path length of both MZI arms was kept the same. The path length of the arm without the ring is the path length from the first Y-splitter to the output Y-splitter. The path length of the arm with the ring is

calculated as the sum of the path length from the first Y-splitter to the ring and from the ring to the output Y-splitter of the MZI. The endpoint position at the ring for these two paths is the position where the coupling gap between the ring and the bus waveguide is minimum (150 *nm*). Path lengths used to design all these sensors are shown in Fig. 3.8.
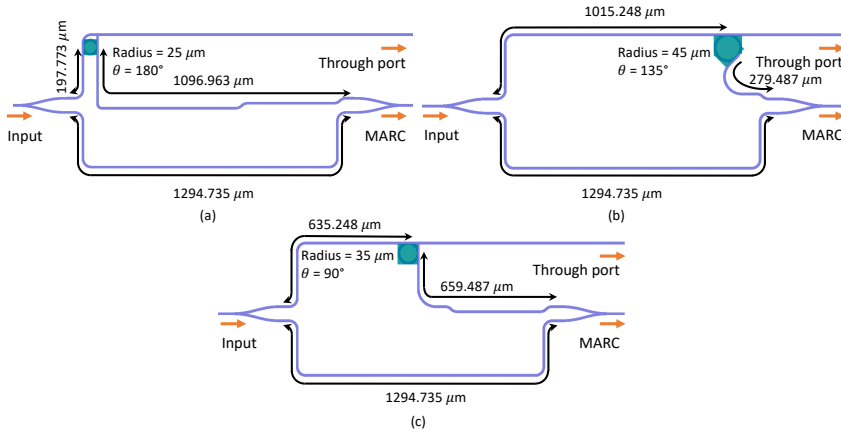
FIGURE 3.8. (a) Design of a MARC sensor with a ring resonator with 180°and 25 *μm* radius. (b) Design of a MARC sensor with a ring resonator with 135°and 45 *μm* radius. (c) Design of a MARC sensor with a ring resonator with 90°and 35 *μm* radius.

2-ring and 3-ring MARC sensor

To determine the multiplexing capability of the MARC, sensors were designed with 2 and 3 ring resonators. For the 2-ring MARC configuration, two rings with radii of 25 *μm* and 45 *μm* were used, with angular separations of 180°and 135°respectively as shown in Fig. 3.9(a). Similarly, for the 3-ring configuration, 3 ring resonators were used with radii of 25 *μm*, 35 *μm* and 45 *μm*, and angular separations of 180°, 90°and 135°respectively as Fig. 3.9(b). To prevent overlapping of resonances, the rings were designed with varying radii in both configurations. To ensure that the MZI remained balanced in both 2-ring MARC and 3-ring MARC, the path length of both MZI arms for each ring was kept the same. To differentiate, the path lengths used for different rings in both designs are highlighted with different colors in Fig. 3.9.
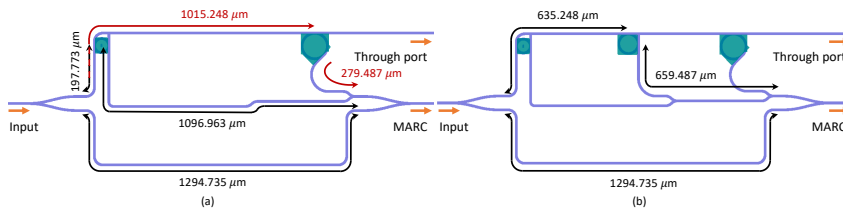
FIGURE 3.9. (a) Design of a MARC sensor with 2 ring resonators with 180°and 135°angular separation. Radii for these two rings are 25 μm and 45 μm, respectively. (b) Design of a MARC sensor with 3 ring resonators. For this case, an additional ring resonator with 35 μm ring radius and 90°is integrated with the MARC.

3.2.4 Microfluidics design

To enable precise flow of target fluid flow over the ring resonator, a microfluidics system based on Poly-Di-Methyl Siloxane (PDMS) was created. The PDMS microfluidics system features multiple channels, each with a width of 150 μm and height of 80 μm, and a separate inlet and outlet for accurate control of the fluid flow.

3.2.5 Fabrication of MARC sensor and microfluidics

MARC sensors were fabricated on SOI wafers with 220 nm of hydrogenated amorphous silicon on top of the 1 μm thermal oxide layer. Amorphous silicon was deposited on a thermal oxide wafer by plasma enhanced chemical vapor deposition (PLasmaLab System 100-PECVD) using SiH4 and Ar gases. Silicon strip waveguides with 500 nm width were patterned by electron beam lithography (Elionix ELS-G100) using e-beam resist (Allresist AR-P 6200). Lithography was followed by dry etching using inductively coupled plasma reactive ion etching (ICP-RIE). SU8 polymer strips were photolithographically patterned on top of silicon inverted tapers. SU8 strips were 300 μm long, 2 μm wide and 2 μm high. The complete chip was covered with 400 nm layer of Polymethyl methacrylate (PMMA) and a small area over the ring resonators was exposed with electron beam lithography to ensure that only the ring resonator interacts with the refractive index change in the surrounding.

For the controlled flow of solution over each ring resonator in the MARC sensors, three 150 μm wide and 80 μm high microfluidic channels were made on PDMS polymer using soft lithography. For sensing experiments, PDMS microfluidics and the photonic chip were clamped together with an acrylic plate.
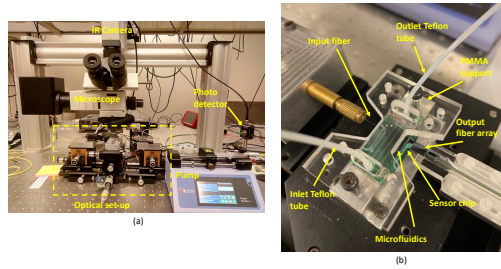
FIGURE 3.10. Optical-microfluidic experimental set-up to test optical waveguide based sensors.

3.2.6 Experimental set-up

To carry out experimental characterization, a photonic chip with PDMS microfluidics was placed on a translational stage. To couple light from an external cavity laser with a central wavelength of 1550 *nm* into the waveguide, a tapered lensed fiber with a spot diameter of 2.5 *μm* and a working distance of 14 *μm* was utilized. To control the polarization of the light from the laser source and improve the coupling to the TE-like mode of the waveguides, a polarization controller (Thorlabs FPC562) was employed. To capture the optical power from the through output and the MARC output, two single-mode optical fibers connected with InGaAs photodetectors (Thorlabs DET10C2) were positioned in front of the output waveguides. However, for the SWG-based sensor (section 3.1), only one photodetector was needed to capture the sensor response. Finally, a LabView program was used for output power collection and laser wavelength tuning.

To perform sensing characterization, the PDMS microfluidic's inlet was connected to a vial containing the target solution, while the outlet was connected to a syringe pump with Teflon tubes. The experimental set-up for the sensing measurements is shown in Fig. 3.10.

3.2.7 Sensor characterization and sensing method

To characterize fabricated sensors and perform sensing experiments, the above-shown measurement setup was used. Firstly, input and output fibers were aligned with the sensor´s input and output waveguides to maximize the output optical power. Before flowing target fluids over the sensor, MARC and ring resonator intensity responses were measured to verify if the sensor response is as expected. After this quick test, the DI water was flowed over the sensor surface for baseline measurements. Saline solutions with varying salt concen-

trations were used for the sensing experiment. During the sensing experiment, solutions were pumped through the microfluidic channel with the syringe pump at a 20 $\mu l/min$ rate. Firstly, DI water was pumped over the sensor, and the corresponding MARC and ring resonator responses were measured. It was done to create a baseline before pumping saline solutions. After the baseline measurements, saline solutions with varying concentrations (6%, 12%, 18%) were consecutively pumped over the sensor surface. For each saline solution, MARC and through port intensity responses were measured after 1 minute of continuous flow of saline solution over the sensor surface, before switching the solution. Finally, the DI water was again pumped over the sensor, and corresponding intensity responses were measured. After measurements, MARC and through port outputs were plotted and used to accurately calculate the resonance shift. Measurement with 1-ring MARC sensor highlighted the advantage of MARC sensor in terms of large measurement range, which directly related with the effective free spectral range obtained from the MARC. Sensing measurements done using 2-rings and 3-ring MARC sensors showed the advantage of both large measurement range and multiplexing capability. During these experiments, no TEC controller was used to regulate the temperature. All measurements were performed at room temperature and saline solutions were kept at room temperature before measurements.

3.2.8 Analysis of measurement data

A LabView program was utilized to scan wavelengths and save raw data of intensity vs. wavelength from MARC and through port outputs. MATLAB was used to fit MARC spectral response with the theoretically generated spectral response to extract the resonance data. In addition, the through port output response was Lorentzian fitted to extract precise resonance shift information. MARC output response for various saline solutions and corresponding through port output responses are shown in Fig. 3.11. The Lorentzian fitting to a through port resonance is shown in Fig. 3.11(c).

For the case of 1-ring MARC, the MARC output enhances the measurement range of the sensor which allows reliable tracking of resonance when the resonance shift is larger than the FSR of the ring resonator. However, in the case 2-ring and 3-ring MARC sensors, the output of the MARC not only expands the measurement range of the sensors, but also enables the use of several ring sensors at once by utilizing the unique spectral signatures generated by the MARC. To distinguish responses from each individual ring, the multiplexed spectral response from the baseline measurement was overlaid with the theoretically estimated spectral response from each ring. Additionally,
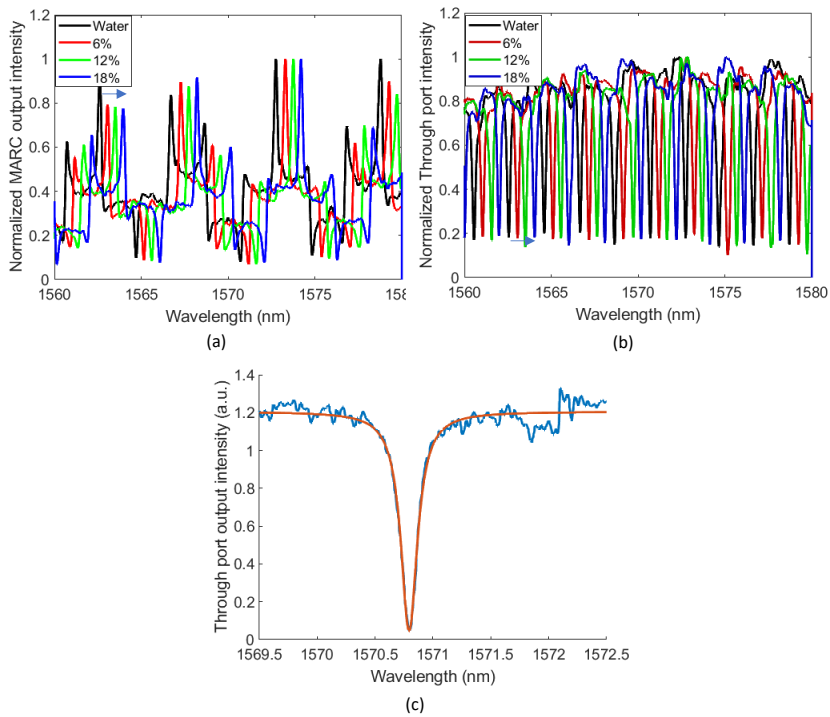
FIGURE 3.11. (a) Transmission response obtained from MARC, (b) through port outputs for different saline solutions, (c) Through port resonance fitted with a Lorentzian fit.
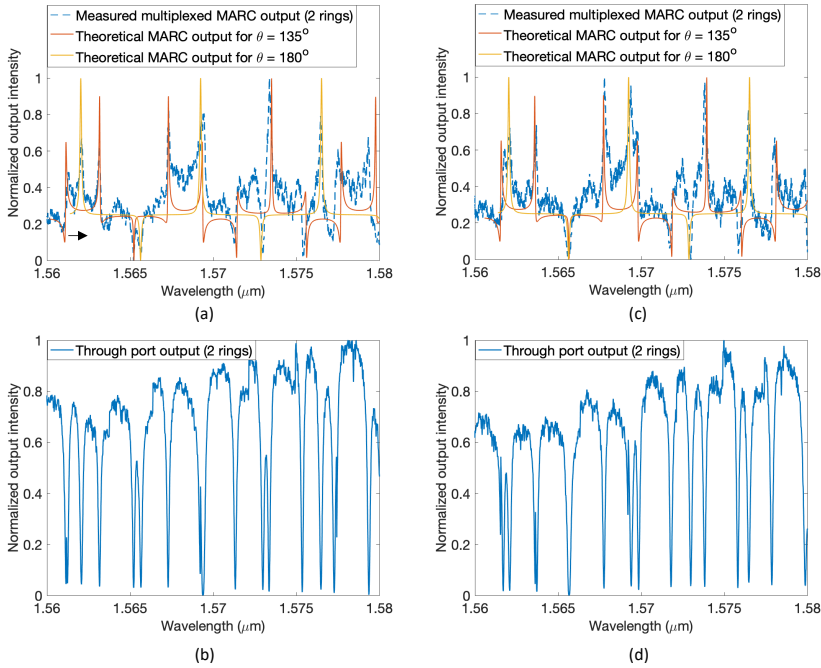
FIGURE 3.12. Measured transmission responses from a 2-ring MARC sensor. (a) Multiplexed response from the MARC with two rings covered with deionized water, (b) Multiplexed response from the through port with two rings covered with de-ionized water, (c) Multiplexed response from the 2-ring MARC when ring with 135°angular separation was covered with 6% saline solution, (d) Multiplexed response from the through port when ring with 135°angular separation was covered with 6% saline solution.

a Lorentzian fit was used to find the precise resonance shift for each ring by fitting it to the through port response.

Figure 3.12 presents a 2-ring MARC output response overlaid with the MATLAB-generated plots for each ring and corresponding through port output response. Figures 3.12(a) and (b) show the MARC and through port responses for the case when water was flowed over both ring resonators. The MATLAB-generated signal was overlaid the measured MARC output and fine-tuned to fit well by manually adjusting the refractive index and ring radius. The fine-tuned theoretical signal was then fitted to the MARC response observed during the sensing experiment. A minor change in wavelength was all that was needed to align the theoretical signal with the actual MARC data. A wavelength shift of 0.52 *nm* was used when 6% saline solution was flowed over the ring with 135°angular separation, as illustrated in Figure 3.12(c).

For the case of 3-rings, a similar mathematical MATLAB analysis was
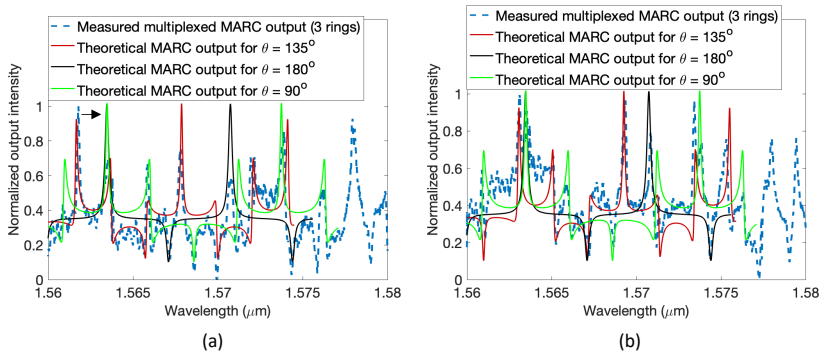
FIGURE 3.13. Measured transmission response from multiplexed MARC sensors (a) Measured response from the MARC with 3 rings covered with deionized water, (b) when ring with 135°angular separation was covered with 18% saline solution.

carried out to distinguish the response from each ring during the sensing experiments. Measured MARC output and fitted MATLAB plot for 3 rings are shown in Fig. 3.13 when used for sensing. MARC output for the 3-ring configuration shows higher output noise compared to the 2-ring configuration. This can be attributed to imperfections in waveguide fabrication and interference from reflections at the chip end facets. More details of this work are found in papers I and II.

The central focus of Paper III, which is included in this thesis, was the development of a biocompatible microfluidics system for a lab-on-a-chip sensor. My main contribution to the paper was to assess the biocompatibility of the microfluidics system, by performing proof-of-principle measurements with an SOI ring resonator and MARC sensors. This also allowed us to demonstrate the practical application of ring resonator-based sensors for lab-on-a-chip technologies.

3.3   REFERENCES

[1] RG Heideman and PV Lambeck. Remote opto-chemical sensing with extreme sensitivity: design, fabrication and performance of a pigtailed integrated optical phase-modulated Mach-Zehnder interferometer system. *Sensors and Actuators B: Chemical* **61** (1-3), 100–127 (1999). Cited on page/s 23, 24.

[2] Francisco Prieto, Borja Sepúlveda, A Calle, Andreu Llobera, Carlos Domínguez, Antonio Abad, A Montoya, and Laura M Lechuga. An integrated optical interferometric nanodevice based on silicon technology for biosensor applications. *Nanotechnology* **14** (8), 907 (2003). Cited on page/s 23.

[3] Dengpeng Yuan, Ying Dong, Yujin Liu, and Tianjian Li. Mach-Zehnder interferometer

biochemical sensor based on silicon-on-insulator rib waveguide with large cross section. *Sensors* **15** (9), 21500–21517 (2015). Cited on page/s 23.

[4] Stefania Dante, Daphné Duval, Borja Sepúlveda, Ana Belen González-Guerrero, José Ramón Sendra, and Laura M Lechuga. All-optical phase modulation for integrated interferometric biosensors. *Optics Express* **20** (7), 7195–7205 (2012). Cited on page/s 24.

[5] Przemek J Bock, Pavel Cheben, Jens H Schmid, Jean Lapointe, André Delâge, Siegfried Janz, Geof C Aers, Dan-Xia Xu, Adam Densmore, and Trevor J Hall. Subwavelength grating periodic structures in silicon-on-insulator: a new type of microphotonic waveguide. *Optics Express* **18** (19), 20251–20262 (2010). Cited on page/s 25.

[6] Jonas Flueckiger, Shon Schmidt, Valentina Donzella, Ahmed Sherwali, Daniel M Ratner, Lukas Chrostowski, and Karen C Cheung. Sub-wavelength grating for enhanced ring resonator biosensor. *Optics Express* **24** (14), 15672–15686 (2016). Cited on page/s 25.

[7] R Sumi, Nandita Das Gupta, and Bijoy Krishna Das. Integrated optical Mach-Zehnder interferometer with a sensing arm of sub-wavelength grating waveguide in soi. In *2017 IEEE SENSORS* pages 1–3. IEEE (2017). Cited on page/s 25.

[8] Hai Yan, Lijun Huang, Xiaochuan Xu, Swapnajit Chakravarty, Naimei Tang, Huiping Tian, and Ray T Chen. Unique surface sensing property and enhanced sensitivity in microring resonator biosensors based on subwavelength grating waveguides. *Optics Express* **24** (26), 29724–29733 (2016). Cited on page/s 25.

[9] Lijun Huang, Hai Yan, Xiaochuan Xu, Swapnajit Chakravarty, Naimei Tang, Huiping Tian, and Ray T Chen. Improving the detection limit for on-chip photonic sensors based on subwavelength grating racetrack resonators. *Optics Express* **25** (9), 10527–10535 (2017). Cited on page/s 25.

[10] Mukesh Yadav and Astrid Aksnes. Multiplexed Mach-Zehnder interferometer assisted ring resonator sensor. *Optics Express* **30** (2), 1388–1396 (2022). Cited on page/s 30.

CHAPTER 4

Summary of papers

The main objective of this work was to develop a multiplexed optical waveguide-based sensor with a wide measurement range and high sensitivity. In addition to the development of a sensor, research on microfluidics was also done during my Ph.D. work. Microfluidics is an important component of a Lab-on-a-chip platform in addition to a sensor chip. The thesis spans the complete cycle of the development process of an optical waveguide sensor platform. This includes the design, fabrication, and characterization of sensors. As a result, the thesis includes theoretical analysis as well as experimental analysis work.

This chapter gives a brief overview and short discussion of each paper included in the thesis.

4.1 Proof of concept: MARC

Spectral shaping of ring resonator transmission response
Mukesh Yadav, Jong Wook Noh, Dag Roar Hjelme, and Astrid Aksnes, "Spectral shaping of ring resonator transmission response," *Opt. Express 29, 3764-3771 (2021)*

This study focused on the impact of the ring resonator drop port phase response on intensity. Prior to this publication, there were only a few papers on this topic, with most of the research focusing on the through port output phase response. The study introduced amplitude and phase response from the ring resonator drop port output and explored the effects of varying the angular separation between the through port and the drop port waveguide. This resulted in a modified phase response, which was then studied to determine its effect on intensity response.

Theoretical analysis of the hybrid configuration with varying angular separation showed transmission spectra with unique spectral signatures over a wavelength band. These spectral signatures offered advantages over a standard ring resonator as they consisted of symmetric Fano-like, asymmetric Fano-like, Lorentzian and inverse Lorentzian resonances with different shapes of adjacent resonances. The hybrid design was fabricated and characterized, confirming the theoretical analysis to generate unique spectral signatures with large effective free spectral ranges.

The distinct lineshapes generated from the hybrid design can potentially be utilized for several applications including optical switching and filtering. Additionally, the large effective free spectral range obtained from the hybrid design is highly advantageous for sensing applications to detect wide refractive index change. It provides a large measurement range independent of the ring parameters compared to a ring resonator-based sensor. An experiment on temperature sensing was conducted to show how spectral signatures can be used in optical sensing. The findings revealed that instead of decreasing the ring radius, changing the angular separation between the drop port and the through port waveguides can expand the measurement range of a ring resonator sensor. The study also discussed the possibility of using spectral signatures to label RRs with unique spectral fingerprints for multiplexing of RR sensors in a MARC.

4.2   Evaluation of MARC sensor for large measurement range and multiplexing

Multiplexed Mach-Zehnder interferometer assisted ring resonator sensor
Mukesh Yadav and Astrid Aksnes, "Multiplexed Mach-Zehnder interferometer assisted ring resonator sensor," *Opt. Express 30, 1388-1396 (2022)*

In this paper, we focused on addressing the challenges of a refractive index sensor based on a ring resonator by utilizing the MARC sensor. Creating a ring resonator sensor that has a high Q-factor, wide measurement range, and small footprint is a difficult task. Furthermore, the short measurement range limits the multiplexing capability of ring resonators. Multiplexing is useful in enhancing the throughput and reducing the overall cost of the device. It also allows for flexibility in placing a reference sensor close to the actual sensor for drift correction and control experiments. Typically, real-time continuous resonance tracking is necessary to overcome the challenge of the short measurement range. However, this requires a faster tracking rate than the analyte binding rate, which in turn necessitates the use of an expensive tunable laser source. Multiplexing can be addressed by fabricating multiple ring resonator sensors in a parallel configuration on a chip. However, this configuration typically requires multiple photodetectors or photodiode arrays.

We presented a novel MARC sensor that can simultaneously provide both large measurement range and multiplexing capability without compromising the Q-factor or the detection limit provided by the ring resonator. We have experimentally demonstrated a multiplexed MARC sensor with a large measurement range. For a MARC sensor with 45 μm ring radius, the measurement range was ~16.1 nm which is 8 times larger than for a standard ring resonator sensor. In addition to the enhancement in the measurement range, the transmission response from MARC for a specific angular separation provides a unique spectral signature. We used these spectral signatures in experiments to show that the MARC sensor can detect multiple targets simultaneously. During the experiment, we demonstrated that the sensor can detect up to 2 or 3 rings at once. The MARC sensor has a broad measurement range and can detect multiple targets, making it an ideal option for high throughput sensing for various applications.

4.3 **DEVELOPMENT OF BIOCOMPATIBLE MICROFLUIDICS FOR AN OPTICAL LAB-ON-A-CHIP SENSOR PLATFORM**

Biocompatible bonding of a rigid off-stoichiometry thiol-ene-epoxy polymer microfluidic cartridge to a biofunctionalized silicon biosensor
Sønstevold, Linda, Mukesh Yadav, Nina Bjørk Arnfinnsdottir, Aina Kristin Herbjørnrød, Geir Uri Jensen, Astrid Aksnes, and Michal Marek Mielnik. "Biocompatible bonding of a rigid off-stoichiometry thiol-ene-epoxy polymer microfluidic cartridge to a biofunctionalized silicon biosensor." . *Journal of Micromechanics and Microengineering 32, no. 7 (2022): 075008*

The focus of the work was on packaging a Lab-on-a-chip biosensor platform. The paper details the development process of a polymer microfluidics cartridge for a silicon microring-based biosensor chip. The microfluidics cartridge was created using Ostemer 322 Crystal Clear, a commercially available off-stoichiometry thiol-ene-epoxy resin from Mercene Labs in Sweden. This development process was necessary to overcome challenges associated with common methods for biocompatible biosensor packaging. While PDMS is the most commonly used polymer in microfluidics applications due to its ability to integrate complex micro and nanofluidic patterns, it has inherent properties that make it difficult to use in LOC systems. For example, PDMS absorbs small hydrophobic molecules and has high gas permeability, which results in gas bubble formation and evaporation during experiments.

The biocompatibility, bonding, and leakage of Ostemer 322-based microfluidics for a Lab-on-a-chip were experimentally tested by bonding it with a biosensor chip and performing biosensing measurements. It was shown that the packaging procedure does not compromise the biological function of the attached biomolecules. Bonded microfluidics eliminates the widespread problem of leakage in clamped systems. Additionally, the bonding is reversible allowing disintegration of the microfluidic package for free access to the sensor surface or re-use of the silicon sensor. In summary, this procedure overcomes many of the obstacles for microfluidic packaging of biosensors both for research and commercialization. My main contribution to this work was to evaluate the biocompatibility of the developed microfluidics system. My role involved conducting sensing measurements with SOI ring resonator and MARC sensors, which allowed us to demonstrate the practical application of ring resonator-based sensors in lab-on-a-chip technologies.

4.4   Evaluation of sensitivity and modulation frequency for MZI sensors utilizing subwavelength gratings

Sensitivity enhanced biophotonic sensor utilizing sub-wavelength gratings

Mukesh Yadav, Jens Høvik, Dag Roar Hjelme, Astrid Aksnes, "Sensitivity enhanced biophotonic sensor utilizing sub-wavelength gratings," *Proc. SPIE 10729, Optical Sensing, Imaging, and Photon Counting: From X-Rays to THz, 107290N (18 September 2018)*

This study was conducted before the development of the MARC sensor. It focused on analyzing the phase modulation and sensitivity of a Mach Zehnder interferometer with Sub-wavelength gratings (SWGs) in its arms. The study examined the effects of SWGs on sensitivity and wavelength-dependent phase modulation, both when SWGs were included in only one arm and in both arms. The goal of adding SWGs was to improve sensitivity and increase the frequency of wavelength-dependent phase modulation.

The results of the simulation indicate that the use of SWGs in both arms can enhance the sensitivity of bulk refractive index change by three times and phase-modulated frequency by two times (50% less wavelength change to achieve the 2π phase change) compared to a conventional asymmetric MZI. On the other hand, when SWGs are only used in one arm of the MZI, the wavelength dependent phase modulation response exhibits a frequency that is at least five times higher. However, dispersion causes the response to be chirped. To verify these findings, MZI with a few periods of SWGs were fabricated and characterized, and the initial measurements for MZI with a few periods of SWGs showed encouraging results.

CHAPTER 5

Conclusions

Optical waveguide-based sensing is sensitive, label-free, portable, and real-time. It's ideal for "on-chip" detection in lab-on-a-chip platforms, providing significant advantages over current analytical methods. Currently, optical waveguide-based sensing is mainly utilized for research purposes. There are only a few companies that are employing optical waveguide sensing technology for commercial products. This is due to the inherent challenges associated with current optical waveguide sensors. Developing an optical sensor that possesses all the necessary qualities, such as high sensitivity, wide measurement range, and multiplexing capability, is a challenging task.

This thesis work is concentrated on the development of on optical waveguide-based sensor system with all these relevant evaluation parameters. The research work during this thesis resulted in the development of a novel sensor called the Mach-Zehnder interferometer-assisted ring resonator configuration (MARC) sensor. The MARC sensor provides wide measurement range and ability to multiplex in addition to the high sensitivity. The MARC sensor's versatility and high throughput capabilities make it a robust sensor platform for commercial applications.

In this thesis, Paper 1 presented the theoretical and experimental study of the Mach-Zehnder interferometer-assisted ring resonator configuration (MARC). The study explored the effect of varying the angular separation between the through port and the drop port waveguide on the RR drop port phase response. A balanced MZI determined the intensity response for different angular separations. Transmission spectra obtained for different angular separations showed unique spectral signatures with large effective free spectral ranges. These results were experimentally verified. An experiment on temperature sensing was conducted to show how spectral signatures can be used in optical sensing. The presented MARC architecture has a wide range of potential applications, including optical filtering and switching, but its most significant use is in optical sensing devices due to its large measurement range and multiplexing capability.

In Paper 2, the MARC sensor was evaluated as a platform with high sensitivity, large measurement range, and multiplexing capability, which are essential

parameters that determine the cost, portability, and throughput of a sensor. We have experimentally demonstrated that the MARC sensor can simultaneously provide both large measurement range and multiplexing capability without compromising the Q-factor.

In addition to developing the sensor technology, microfluidics packaging of the sensor chip was developed using Ostemer polymer. PDMS is one of the most common polymer materials used for microfluidics. It has several advantages but poses several challenges, including high gas permeability, reversible bonding, and reusability. Paper 3 presented microfluidics fabrication processing and its characterization. Characterization of microfluidics included bonding with a sensor chip and the biocompatibility test by sensing a biomarker. The results showed high bonding strength between the sensor chip and microfluidics, no leakage of fluid during the sensing experiment, and no effect of microfluidics processing on the biofunctionalization of the chip.

The study of sub-wavelength gratings (SWGs) on the Mach-Zehnder interferometer was explored in the early part of the thesis to enhance sensitivity and perform all-optical phase modulation. This approach was presented in paper 4 and involved theoretical simulation analysis and preliminary experimental results. The analysis showed a 3-fold increase in sensitivity and a 2-fold increase in modulation frequency with SWGs in both arms. While this approach has great potential, it requires a high-resolution fabrication facility. Fabrication of low-loss SWG waveguides is challenging. This limitation of SWG-based sensors led to the study and development of the MARC architecture.

Outlook

The published papers show advancements in sensor technology and packaging in comparison to what is currently available. These components are vital for a portable sensor platform. The newly developed MARC sensor architecture enables the use of cost-effective light sources (LEDs) and detectors. The focus of future work should be on integrating the source, chip, and detector and developing bio-functionalization protocols for specific biomarkers. The ultimate objective is to create an affordable health monitoring system for the general public.

Publications

6.1 PAPER I

Spectral shaping of ring resonator transmission response

Spectral shaping of ring resonator transmission response

MUKESH YADAV,* JONG WOOK NOH, DAG ROAR HJELME, AND ASTRID AKSNES

Department of Electronic Systems, Norwegian University of Science and Technology (NTNU), Trondheim NO- 7491, Norway
*mukesh.yadav@ntnu.no

Abstract: We present a Mach-Zehnder interferometer assisted ring resonator configuration (MARC) to realize resonator transmission spectra with unique spectral signatures and significantly large effective free spectral ranges. Transmission spectra with unique spectral signatures are generated by changing the angular separation between the through port and the drop port waveguides of the ring resonator (RR). These spectral signatures are comprised of several distinct resonance lineshapes including Lorentzian, inverse Lorentzian and asymmetric Fano-like shapes. One of the spectral signatures generated from the MARC device is utilized for the temperature sensing measurement to demonstrate a MARC-based sensor with high Q-factor and wide measurement range.

1. Introduction

Silicon ring resonator based optical devices are widely utilized for various applications such as optical filters [1,2], modulators [3], and sensors [4–8]. This can be mainly attributed to the combination of high index contrast platform and the availability of complementary metal–oxide–semiconductor (CMOS) fabrication technology [9]. A conventional RR consists of a closed loop waveguide and a bus waveguide. The bus waveguide evanescently couples light into the closed loop waveguide. When the optical path length of the closed loop waveguide is equal to an integer multiple of the source wavelength, light inside the loop interferes constructively and results in resonance. Ring resonators support multiple resonances. The separation between adjacent resonances is defined as the free spectral range and depends on the optical path length of the closed loop. A resonance lineshape of optical resonators is generally symmetric Lorentzian, and its linewidth determines the performances of RR-based filters and sensors.

In recent years, extensive research has been specifically devoted to the modification of the RR resonance lineshape [10–13]. By modification of the resonance lineshape, sharp, and asymmetric Fano lineshapes and square, triangular, sinusoidal shapes are realized. The sharpness and the asymmetry of the Fano lineshape define the sensitivity of the device and enable photonic sensors with high sensitivity and switches with low switching energy [14–16]. Tunability of the asymmetry in Fano resonance lineshapes enables the realization of reconfigurable optical filters [17]. Square, sinusoidal, and triangular shapes are relevant for optical filtering applications [11,18].

The above-mentioned resonance lineshapes are commonly realized by ring-coupled Mach-Zehnder interferometer (MZI) devices, and they can be divided into two categories. One configuration, all-pass ring resonator inserted into one arm of the MZI, is utilized to convert the phase response at the through port output into the intensity response. This resultant response is comprised of Fano resonances spaced by the RR free spectral range [10,17,19,20]. The Fano resonance lineshape can be tuned into different asymmetrical ones by using an active or passive component on one of the arms in the configuration. The other configuration, add-drop ring resonator inserted into one arm of the MZI, is designated to translate the phase response at

the drop-port output into the intensity response [11,18]. In addition to the ring-enhanced MZI configurations, a double injection configuration has been explored to realize intensity responses with sinusoidal, triangular and square shapes [12].

Throughout this paper, we shall use the terms 'lineshape' and 'transmission spectrum' for the shape of an individual resonance and the intensity response over a wavelength range including several resonances, respectively.

In this paper, we present a Mach-Zehnder interferometer assisted ring resonator configuration (MARC) to tailor the RR drop port phase response and the resulting transmission spectrum. The phase response at the drop port is altered by carefully designing a RR geometry, specifically the angular separation constituted by two bus waveguides in the immediate vicinity of the ring. By incorporating a particular angular separation in the MARC device, it produces transmission spectra with unique spectral signatures and significantly large effective free spectral ranges. These unique spectral signatures are comprised of several distinct lineshapes including Lorentzian, inverse Lorentzian and asymmetric Fano-like shapes. Furthermore, these unique spectral signatures in the transmission spectrum remain unchanged even when the spectrum is shifted. (Note: Tuning and control of individual resonance lineshapes are out of the scope of this paper.) The combination of this characteristic and the large effective free spectral range is experimentally verified and utilized for a temperature sensing experiment to demonstrate a MARC sensor with high Q-factor of 60,000 and 2-fold enhanced measurement range compared with the conventional RR.

2. Theoretical analysis of the MARC

A MARC device is comprised of a balanced MZI and an add-drop ring resonator as shown in Fig. 1. The aim of this study is to investigate the effect of an arbitrary angular separation, θ, between the through and the drop port waveguides on the MARC intensity response. To analyze the MARC intensity response, we first consider a RR with an arbitrary angular separation and investigate the effect of the angular separation on the drop port phase response. The drop port amplitude transmission response, t, of a RR with an arbitrary angular separation as shown in Fig. 2(a) is given as [21]:

$$t = -\frac{\sqrt{1-\gamma_1^2}\sqrt{1-\gamma_2^2}a_{\text{d}}\exp[i(\psi\frac{\theta}{2\pi})]}{1-\gamma_1\gamma_2 a\exp[i(\psi)]}, \tag{1}$$

where $\psi = \frac{\omega}{c}n(2\pi r)$ is the round-trip phase shift, n is the effective refractive index, r is the ring radius, a is the single-pass amplitude transmission factor, $\gamma_1(\gamma_2)$ is the self-coupling coefficient of the coupler and a_d is the fraction of the round-trip amplitude transmission factor between the input and output coupler.

The phase of the transmitted light at the RR drop port, ϕ, is given as [21,22]:

$$\phi = \arctan\frac{Im[t]}{Re[t]} = \pi + \psi\frac{\theta}{2\pi} + \arctan\frac{\gamma_1\gamma_2\sin(\psi)}{1-\gamma_1\gamma_2 a\cos(\psi)}. \tag{2}$$

To simplify the numerical analysis in the following, all the ring resonators are assumed to be identical (r=30 μm), lossless (a=1) and critically coupled (γ_1=γ_2).

In the MARC, the balanced MZI is used to convert the phase change introduced by resonances at the drop port into a transmission intensity. The intensity transmission response, T_{out}, obtained from the MARC can be expressed as [11,13]:

$$T_{\text{out}} = \frac{1}{4}[1 + |t|^2 + 2|t|\cos\phi]. \tag{3}$$

Figure 2(b) presents the phase response at the drop port with different angular separations. The ring resonator with the angular separation of 180° is a conventional add-drop resonator
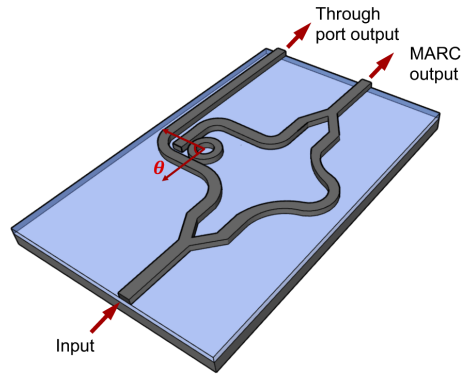
Fig. 1. Schematic of a MARC device with an angular separation of θ between the through port and the drop port waveguides.
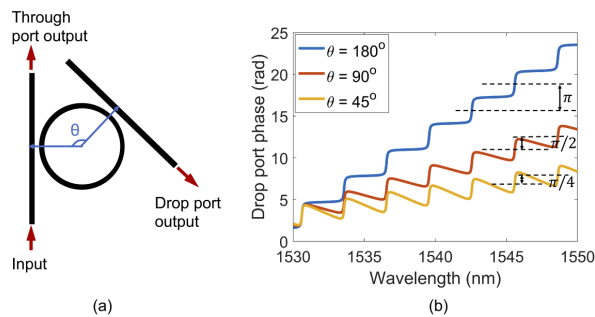
Fig. 2. (a) Schematic of a ring resonator with an angular separation of θ between the through port and the drop port waveguides, and (b) Drop port phase response for different angular separations.

configuration, and its phase increases monotonically as a function of wavelength, leading to π radians phase accumulation between resonances. For 90° angular separation, the accumulated phase difference between resonances is reduced to $\pi/2$ radians. The accumulated phase difference is further reduced to $\pi/4$ radians by setting the angular separation to 45°. The phase response at the drop port is a function of angular separation and wavelength, and thus it can be controlled by choosing a specific angular separation.

Figure 3 shows six transmission spectra of the MARC with angular separations of 180°, 135°, 90°, 60°, 45°, and 30°. The transmission spectrum for $\theta = 180°$ (Fig. 3(a)) is comprised of two distinct resonance lineshapes, separated by a free spectral range of 3 *nm*. These lineshapes exhibit Lorentzian and inverse Lorentzian resonance lineshapes corresponding to the interference maxima and minima. Figure 3(c) shows the transmission spectrum for $\theta = 90°$ with three distinct resonance lineshapes. These resonance lineshapes display Lorentzian, inverse Lorentzian and Fano-like shapes. The Fano-like lineshape is located in the middle of the Lorentzian and the inverse Lorentzian lineshapes, induced by the interference when the total phase accumulation is $\pi/2 + n\pi$. Furthermore, seven distinct resonance lineshapes are found in the transmission

spectrum of $\theta = 30°$ as depicted in Fig. 3(f), and five of them show asymmetric Fano-like shapes. Based on these transmission calculations, it is concluded that there is an inverse relationship between the angular separation and the number of distinct resonance lineshapes in a transmission spectrum. Consequently, a specific angular separation can be designated for a transmission spectrum in combination with multiple distinctive resonance lineshapes. Moreover, that makes it possible to have a unique spectral signature within a relatively narrow band.
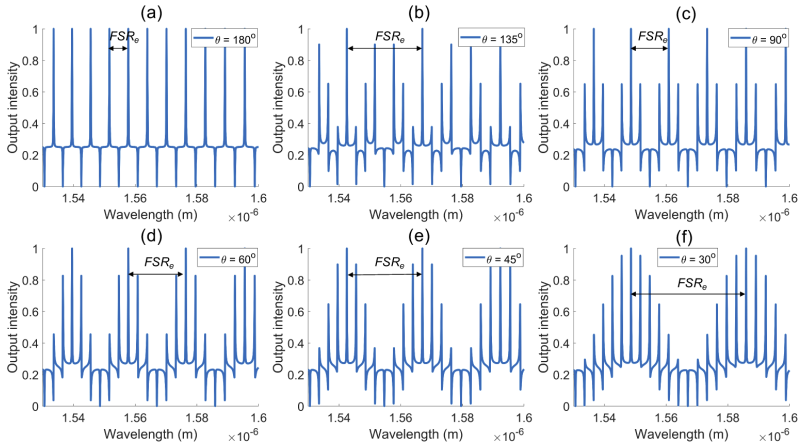
Fig. 3. Transmission spectra of MARC devices with angular separations of (a) 180°, (b) 135°, (c) 90°, (d) 60°, (e) 45°, and (f) 30°.

When the accumulated phase reaches an integer multiple of 2π, the resonance lineshape repeats itself. This results in a transmission spectrum with a certain period, defined as the effective free spectral range (FSR_e). The FSR_e is related to the free spectral range (FSR) of the given ring resonator. The FSR is defined as the separation between two consecutive resonances, and given by $\frac{\lambda^2}{n_g 2\pi r}$, where n_g is the group index, λ is the vacuum wavelength and r is the ring radius. For a given angular separation ($\theta = \frac{2\pi}{L}$), the FSR_e of a transmission spectrum can be expressed as,

$$FSR_e = N \cdot FSR, \tag{4}$$

where N satisfies the condition $\theta = 2\pi \frac{M}{N}$, that results in $L = \frac{N}{M}$, where N and M are integers. The parameter L can be divided into two cases. In one case, L is a rational number given as an irreducible fraction $L = \frac{p}{q}$, and its solutions are $N = p$ and $M = q$. In the other case, L is a positive integer, and its solutions $N=L$ and $M=1$.

The effective free spectral range (FSR_e) for a given angular separation is governed by the positive integer N. The value of N is inversely proportional to the angular separation, which leads to an increase in the FSR_e. As shown in Fig. 3(f), the FSR_e is calculated to be 36 nm, and this is 12 times larger than the normal FSR of 3 nm. Figures 3(b) and (e) show that both spectra of 45° and 135° have the same FSR_e of 24 nm, but these spectra are highly distinctive. This phenomenon can be explained by the accumulated phase shift between the resonances. For the 135° case, the resonances occur with the phase shift of $\frac{3}{8}\pi$ radians, which is three times larger than that of the 45° case, and correspondingly this difference differentiates one transmission spectrum from another. However, both cases require the same number of phase-shift steps to attain the total phase accumulation of an integer multiple of 2π, and these transmission spectra

have the same FSR_e. Thus, unique spectral signature and extended effective free spectral range are achievable by means of the angular separation specified for a MARC device.

3. Design and fabrication

We designed MARC devices based on silicon strip waveguides with balanced MZIs and ring resonators, operating in the telecommunication wavelength band. Ring resonators were designed with a radius of 30 μm, a coupling gap between the ring and the bus waveguides of 150 nm, and five angular separations of 30°, 45°, 90°, 135°, and 180°. Silicon strip waveguides were 500 nm wide and 220 nm high to support the fundamental TE-like mode at the source wavelength of 1550 nm. For waveguide input and output coupling, inverted taper couplers were utilized to enhance the coupling efficiency.

MARC devices were fabricated on amorphous silicon-on-insulator (SOI) consisting of a hydrogenated amorphous silicon ($\alpha - Si : H$) layer of 220 nm and a buried thermal oxide layer of 1 μm on a 100 mm silicon wafer. The hydrogenated amorphous silicon was deposited by plasma enhanced chemical vapor deposition (PECVD). MARC devices were patterned by electron beam lithography (Elionix ELS-G100) using e-beam resist (Allresist AR-P 6200), followed by dry etching with inductively coupled plasma reactive ion etching (ICP-RIE). The fabricated devices were inspected under the scanning electron microscope (SEM). SEM images of fabricated devices with angular separations of 180° and 90° are shown in Fig. 4.

(a)   (b)
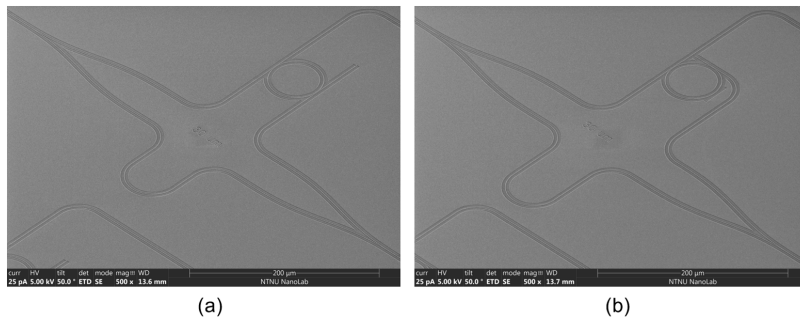
Fig. 4. SEM images of the MARC with a ring radius of 30 μm and angular separations of (a) 180°, and (b) 90°.

4. Experimental characterization

For optical characterization and evaluation of the MARC devices, end-fire coupling between the input waveguides and the tapered lensed fiber having a working distance of 14 μm and a spot diameter of 2.5 μm was used. A tunable external cavity laser (Thorlabs TLK-L1550M) with 1550 nm center wavelength and a fiber polarization controller (Thorlabs FPC562) were used for controlling the wavelength and the input polarization of the light. Two single mode fibers were placed at the output waveguides: one for the through port and the other for the MARC output, and these fibers were directly connected to InGaAs photodetectors (Thorlabs DET10C2).

Figure 5 presents transmission spectra obtained from the fabricated MARC devices. This confirms the theoretical prediction that the MARC devices with different angular separations produce a variety of spectral signatures. The discrepancies between experimental spectra in Fig. 5 and the corresponding theoretical spectra in Fig. 3 are due to a combination of wavelength dependent laser power, waveguide fabrication imperfections, and interference from chip end facet

reflections. As can be seen in Fig. 5(c), the transmission spectrum from MARC with 90° angular separation consists of three distinct resonance lineshapes: Lorentzian, inverse Lorentzian and Fano-like resonance shapes, separated by the *FSR* of 2.95 *nm*. Due to its spectral signature, it shows the FSR_e of 11.8 *nm*, which is four times larger than the normal *FSR*. In the 45° case, the measured transmission spectrum exhibit five distinct resonance lineshapes including Lorentzian, inverse Lorentzian and three non-identical asymmetric Fano-like shapes (Fig. 5(d)). In addition to that, the measured FSR_e is 23.6 *nm*. The 135° case also shows five distinct resonance lineshapes and FSR_e of 23.6 *nm* as shown in Fig. 5(b). As predicted from the calculations, it is experimentally confirmed that spectra of 45° and 135° have the same FSR_e. In spite of the same FSR_e, these transmission spectra are very distinctive since each spectrum has unique spectral signatures over the operational wavelength band.
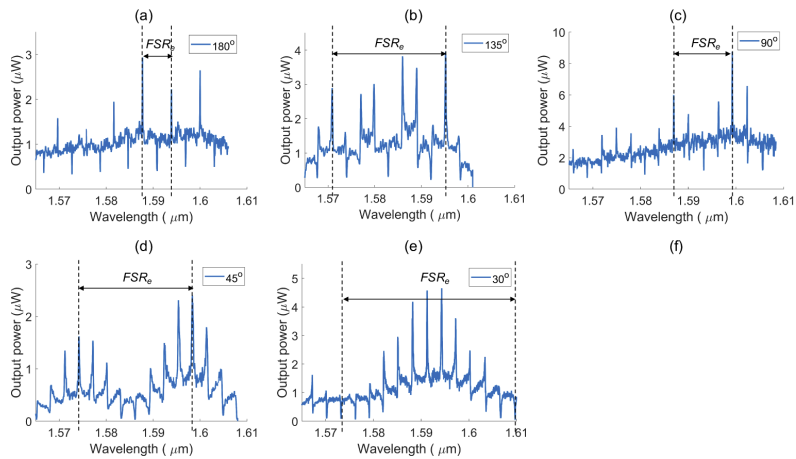
Fig. 5. Measured non-normalized transmission spectra of the MARC for angular separations of (a) 180°, (b) 135°, (c) 90°, (d) 45°, and (e) 30°.

5. Sensing experiment

To investigate a potential application of the spectral signature generated from a MARC device, we performed a temperature sensing measurement. We designed and fabricated several MARC devices with the angular separation of 180° and ring radii of 30 *μm* and 45 *μm* in order to determine the Q-factor and the sensing performance. In addition to that, although the coupling gap between the ring and the bus waveguide is a crucial parameter [21], the coupling gap is fixed to be 150 *nm* due to the fabrication process simplification. In this experiment, we monitor simultaneously both output signals from the through port and the MARC output.

The measured Q-factors are 29,600 and 51,900 for MARC devices with ring radii of 30 *μm* and 45 *μm*, respectively. These measurement values are averaged from four different MARC devices. The corresponding *FSR*s measured from the through port output are 2.95 *nm* and 1.88 *nm*, and FSR_es measured from the MARC output are 5.9 *nm* and 3.76 *nm* for ring radii of 30 *μm* and 45 *μm*, respectively. The transmission spectra from the through port and the MARC outputs of a 45 *μm* ring radius device are shown in Fig. 6(a). The MARC device with the ring radius of 45 *μm* has the highest Q-factor of 60,000 and FSR_e of 3.76 *nm* and was therefore selected for temperature sensing. For the temperature sensing experiment, the photonic chip was mounted on

the stage equipped with a Peltier element, and the temperature was varied from 21°C to 48°C while the optical outputs were continuously monitored. The 27°C rise in temperature causes the 2.5 *nm* red shift of the entire transmission spectrum as can be seen Fig. 6(b), which exceeds the *FSR* of 1.88 *nm*. This red shift, however, falls within the range of the FSR_e (3.76 *nm*), and consequently its measurement range is extended to the FSR_e. Therefore, it is demonstrated that the MARC sensor utilizing the FSR_e and the unique transmission spectrum has a 2-fold increase in the measurement range constrained generally by the *FSR* of conventional RR and MZI based sensors. Moreover, it is demonstrated that the increase in the ring radius from 30 *μm* to 45 *μm* to reduce the bending losses result in 75 % enhancement in the Q-factor with only 36 % reduction in the FSR_e. This FSR_e can be further enhanced by changing the angular separation. Thus, the MARC device with a large ring radius enables the realization of a sensor with both high Q-factor and wide measurement range.
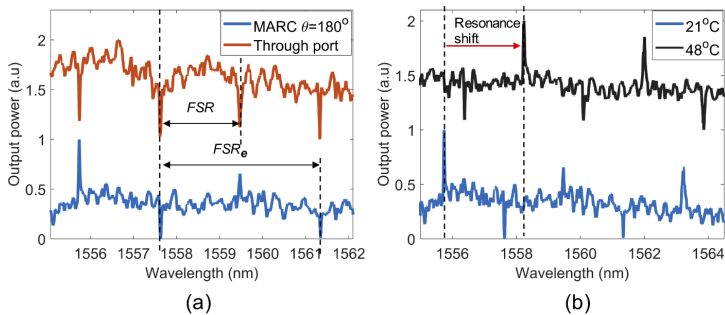
Fig. 6. (a) Measured transmission spectra from a MARC device with the ring radius of 45 um and the angular separation of 180°, (b) MARC transmission spectra at different temperatures. Noise in signals is likely due to reflections from end facets. Note: Offset in y direction is added to the plots to separate out transmission spectra.

6.   Conclusion

We have proposed and experimentally demonstrated the Mach-Zehnder interferometer assisted ring resonator configuration (MARC), which generates transmission spectra with unique spectral signatures and significantly large effective free spectral ranges. It utilizes the angular separation between the through port and the drop port waveguides to realize spectral signatures. Spectral signatures generated from MARC are comprised of distinct resonance lineshapes including Lorentzian, inverse Lorentzian, and Fano-like lineshapes.

A temperature sensing experiment has been presented to exhibit a potential application of spectral signatures in optical sensing. It demonstrates that the measurement range of a ring resonator sensor can be enhanced by changing the angular separation between the drop port and the through port waveguides, instead of reducing the ring radius. In addition to enhancing the measurement range, spectral signatures can be used to label RRs with specific spectral fingerprints, which can potentially be utilized for multiplexing of RR sensors in a MARC.

The proposed MARC device can be designed to give any number of distinct resonance lineshapes within a narrow spectrum band, which could be desirable for optical switching and filtering.

Disclosures. M.Y., A.A. and D.R.H. have applied for patent GB2004009.3 for optical sensing apparatus. The other author declares no competing financial interests.

References

1. G. Griffel, "Synthesis of optical filters using ring resonator arrays," IEEE Photonics Technol. Lett. **12**(7), 810–812 (2000).
2. B. E. Little, S. T. Chu, H. A. Haus, J. Foresi, and J.-P. Laine, "Microring resonator channel dropping filters," J. Lightwave Technol. **15**(6), 998–1005 (1997).
3. M. R. Watts, W. A. Zortman, D. C. Trotter, R. W. Young, and A. L. Lentine, "Vertical junction silicon microdisk modulators and switches," Opt. Express **19**(22), 21989–22003 (2011).
4. H. M. Robison and R. C. Bailey, "A guide to quantitative biomarker assay development using whispering gallery mode biosensors," Curr. protocols chemical biology **9**(3), 158–173 (2017).
5. T. Claes, J. G. Molera, K. De Vos, E. Schacht, R. Baets, and P. Bienstman, "Label-free biosensing with a slot-waveguide-based ring resonator in silicon on insulator," IEEE Photonics J. **1**(3), 197–204 (2009).
6. C. F. Carlborg, K. B. Gylfason, A. Kaźmierczak, F. Dortu, M. J. Bañuls, A. Maquieira Catala, G. M. Kresbach, H. Sohlström, T. Moh, L. Vivien, J. Popplewell, G. Ronan, C. A. Barrios, G. Stemme, and W. van der Wijngaart, "A packaged optical slot-waveguide ring resonator sensor array for multiplex label-free assays in labs-on-chips," Lab Chip **10**(3), 281–290 (2010).
7. T. Claes, W. Bogaerts, and P. Bienstman, "Experimental characterization of a silicon photonic biosensor consisting of two cascaded ring resonators based on the vernier-effect and introduction of a curve fitting method for an improved detection limit," Opt. Express **18**(22), 22747–22761 (2010).
8. A. Ksendzov and Y. Lin, "Integrated optics ring-resonator sensors for protein detection," Opt. Lett. **30**(24), 3344–3346 (2005).
9. W. Bogaerts, R. Baets, P. Dumon, V. Wiaux, S. Beckx, D. Taillaert, B. Luyssaert, J. V. Campenhout, P. Bienstman, and D. V. Thourhout, "Nanophotonic waveguides in silicon-on-insulator fabricated with cmos technology," J. Lightwave Technol. **23**(1), 401–412 (2005).
10. Y. Lu, J. Yao, X. Li, and P. Wang, "Tunable asymmetrical fano resonance and bistability in a microcavity-resonator-coupled mach–zehnder interferometer," Opt. Lett. **30**(22), 3069–3071 (2005).
11. S. Darmawan, Y. Landobasa, and M. Chin, "Phase engineering for ring enhanced mach-zehnder interferometers," Opt. Express **13**(12), 4580–4588 (2005).
12. R. A. Cohen, O. Amrani, and S. Ruschin, "Response shaping with a silicon ring resonator via double injection," Nat. Photonics **12**(11), 706–712 (2018).
13. Y. Zhang, S. Darmawan, L. Tobing, T. Mei, and D. Zhang, "Coupled resonator-induced transparency in ring-bus-ring mach-zehnder interferometer," J. Opt. Soc. Am. B **28**(1), 28–36 (2011).
14. C.-Y. Chao and L. J. Guo, "Biochemical sensors based on polymer microrings with sharp asymmetrical resonance," Appl. Phys. Lett. **83**(8), 1527–1529 (2003).
15. Y. Yu, M. Heuck, H. Hu, W. Xue, C. Peucheret, Y. Chen, L. K. Oxenløwe, K. Yvind, and J. Mørk, "Fano resonance control in a photonic crystal structure and its application to ultrafast switching," Appl. Phys. Lett. **105**(6), 061117 (2014).
16. M. F. Limonov, M. V. Rybin, A. N. Poddubny, and Y. S. Kivshar, "Fano resonances in photonics," Nat. Photonics **11**(9), 543–554 (2017).
17. L. Zhou and A. W. Poon, "Fano resonance-based electrically reconfigurable add-drop filters in silicon microring resonator-coupled mach-zehnder interferometers," Opt. Lett. **32**(7), 781–783 (2007).
18. H.-W. Chen, A. W. Fang, J. D. Peters, Z. Wang, J. Bovington, D. Liang, and J. E. Bowers, "Integrated microwave photonic filter on a hybrid silicon platform," IEEE Trans. Microwave Theory Tech. **58**(11), 3213–3219 (2010).
19. F. Wan, G. Qian, R. Li, J. Tang, and T. Zhang, "High sensitivity optical waveguide accelerometer based on fano resonance," Appl. Opt. **55**(24), 6644–6648 (2016).
20. B. Troia, J. S. Penades, Z. Qu, A. Z. Khokhar, A. Osman, Y. Wu, C. Stirling, M. Nedeljkovic, V. M. Passaro, and G. Z. Mashanovich, "Silicon ring resonator-coupled mach–zehnder interferometers for the fano resonance in the mid-ir," Appl. Opt. **56**(31), 8769–8776 (2017).
21. W. Bogaerts, P. De Heyn, T. Van Vaerenbergh, K. De Vos, S. Kumar Selvaraja, T. Claes, P. Dumon, P. Bienstman, D. Van Thourhout, and R. Baets, "Silicon microring resonators," Laser Photonics Rev. **6**(1), 47–73 (2012).
22. Y. Zhang, K. Wang, X. Liu, and X. Zhang, "An add-drop ring resonator interferometer sensor with high sensitivity," in *2013 Seventh International Conference on Sensing Technology (ICST)*, (2013), pp. 316–319.

6.2   PAPER II

Multiplexed   Mach-Zehnder   interferometer assisted ring resonator sensor

Multiplexed Mach-Zehnder interferometer assisted ring resonator sensor

MUKESH YADAV* AND ASTRID AKSNES

Department of Electronic Systems, Norwegian University of Science and Technology (NTNU), Trondheim NO- 7491, Norway
*mukesh.yadav@ntnu.no

Abstract: A Mach-Zehnder interferometer assisted ring resonator configuration (MARC)-based multiplexed photonic sensor with a large measurement range is experimentally demonstrated. The presented MARC sensor consists of a balanced Mach-Zehnder interferometer and a ring resonator acting as a sensing component. It produces transmission responses with unique spectral signatures, which depend on the physical angular separation between the through port and the drop port waveguides. These unique spectral signatures enhance the effective free spectral range of ring resonators. Hence MARC sensors with a large measurement range are realized. We experimentally demonstrated that the measurement range from the MARC with 135° angular separation is 8x larger than a standard ring resonator. Moreover, by utilizing the MARC, we distinguished the responses from two and three ring resonators multiplexed together. These results verify proof-of-principle for the MARC-based sensors. This inexpensive compact multipurpose device holds promise for numerous applications.

1. Introduction

Silicon-on-insulator (SOI) based optical waveguide sensors have been intensively investigated for medical diagnosis, food quality control, environmental monitoring, and other applications. These sensors utilize optical waveguide-based transducers for transforming the surrounding refractive index change due to target analytes into a measurable change in the transmission. There exist several types of transducers that use various kind of techniques to transform the refractive index change into the transmission change. Ring resonators [1–4], Mach-Zehnder interferometers [5,6], Bragg gratings [7,8], cascaded micro-ring resonators [9], and cascaded Mach-Zehnder interferometer and ring resonator [10,11] are a few examples of optical waveguide-based transducers. Among these transducers, ring resonators are considered as one of the most promising for refractive index sensing as they can be made small and resonance shifts observed from resonators can be tracked easily with high accuracy. Sensors with small footprint are highly desirable in sensing applications as they reduce the amount of sample volume required during detection. High accuracy increases the detection limit of the sensor and for ring resonator sensors it is achieved by increasing the Q-factor. In standard ring resonators, high Q-factor is attained by reducing the optical bending loss along the ring, which is achieved by changing the dimension of the waveguide and increasing the ring radius [12]. This method improves the Q-factor but shortens the free spectral range, which consequently limits the measurement range. Thus, realization of a ring resonator sensor with high Q-factor, wide measurement range and small footprint is challenging. Moreover, short measurement range also limits the multiplexing capability of ring resonators. Multiplexing is advantageous in enhancing the throughput, which consequently reduces the overall cost of the device. In addition to high throughput, it also provides flexibility of placing a reference sensor in close proximity to the actual sensor for drift correction and control experiments. To overcome the challenge of short measurement range, real-time continuous tracking of resonance is required. This is generally achieved by tracking the resonance with faster rate than the analyte binding rate. However, tracking of resonance with

faster rate normally requires an expensive tunable laser source with fast scanning speed and this solution could be ineffective for bulk sensing, where the refractive index change is abrupt. In general, multiplexing in ring resonator-based sensors is addressed by fabricating multiple ring resonator sensors in a parallel configuration. Ring resonators fabricated in parallel configurations increase the chip size and typically require multiple photodetectors or photodiode arrays [4,13].

Recently, we presented a Mach-Zehnder interferometer assisted ring resonator configuration (MARC) that generates unique spectral signatures by tuning the angular separation between the through port and the drop port waveguides [14]. Spectral signatures generated from the MARC enhance the effective free spectral range of ring resonators. In this paper, we present a novel MARC sensor that can simultaneously provide both large measurement range and multiplexing capability. Moreover, these improvements are achieved without compromising the Q-factor or the detection limit provided by the ring resonator.

2. Theory

A MARC is a design consisting of a balanced Mach-Zehnder interferometer (MZI) and an add-drop ring resonator (RR). The phase response at the ring resonator drop port is engineered by physically changing the angular separation between the drop port and the through port waveguides. The tailored phase response is converted into the transmission response by utilizing a balanced MZI. The transmission spectra obtained from MARC with specific angular separation show unique spectral signatures with large effective free spectral ranges [14].

Figure 1 shows the schematic of a MARC sensor comprised of a single RR with the ring radius of R1 and the angular separation of θ radians. As we presented in our earlier work, an angular separation of θ radians results in a phase response at the drop port with θ radians phase accumulation between resonances. This angular separation dependent phase response is translated into an intensity response with the MZI and shows unique spectral signatures. As illustrated in Fig. 1, the whole MARC device is covered with cladding except the ring resonator. The uncladded ring resonator acts as a sensing element and produces resonance wavelength shifts as a function of the refractive index change in the surrounding. The resonance shift caused by the refractive index change is observed at the through port output and the MARC output. MARC sensors with specific ring radius and angular separation can be designed to enhance the effective free spectral range of ring resonators without compromising the Q-factor.
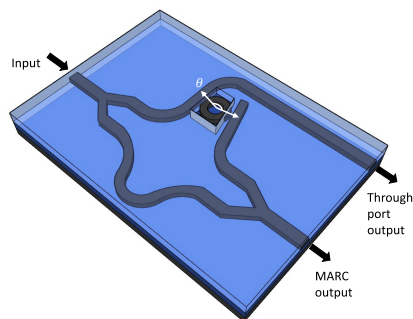

Fig. 1. Schematic of a MARC sensor with an uncladded ring resonator with ring radius of r and angular separation between through port and drop port waveguides of θ.

Through port and MARC transmission responses are given as:

$$T_{\text{through}} = \frac{\gamma_1^2 + \gamma_2^2 a^2 - 2a\gamma_1\gamma_2\cos\psi}{1 + \gamma_1^2\gamma_2^2 a^2 - 2a\gamma_1\gamma_2\cos\psi}, \tag{1}$$

$$T_{\text{MARC}} = \frac{1}{4}[1 + |t|^2 + 2|t|\cos\phi], \tag{2}$$

where, ϕ is the phase response at the drop port, ψ is the round-trip phase shift, $\gamma_1(\gamma_2)$ is the self-coupling coefficient of the coupler and a is the round-trip amplitude transmission factor between the input and output couplers. t is the drop port amplitude transmission response and it is given as, $t = -\frac{\sqrt{1-\gamma_1^2}+\sqrt{1-\gamma_2^2}a_d\exp[i(\psi\frac{\theta}{2\pi})]}{1-\gamma_1\gamma_2 a\exp[i(\psi)]}$. θ in the phase term is the angular separation between the through port and the drop port waveguides.

Any refractive index change in the surrounding of the ring resonator results in a resonance shift. Resonance shifts are proportional to the refractive index change and can be measured from both through port output and the MARC output. Resonance shifts measured from both outputs are similar. However, shifts measured from the through port output are more accurate than the MARC output. It is because the through port output provides resonances with higher Q-factor than the MARC output. The resonance shift as a function of refractive index change obtained from the through port output and the MARC output is given by [3],

$$S = \frac{\Delta\lambda}{\Delta n} = \frac{m}{L}\left(\frac{\partial n_{eff}}{\partial n_{bulk}}\right)^{-1}, \tag{3}$$

where, L is the round-trip length, m is the cavity mode order, n_{bulk} is the bulk refractive index due to the analyte and n_{eff} is the effective refractive index of the guided mode.

In addition to the sensitivity, one of the most important parameters of a sensor is the measurement range, which defines its usability and versatility. For the case of the MARC sensor, the measurement ranges of the through port output and the MARC output are not identical. The measurement ranges of the through port and MARC outputs are given by,

$$\Delta n_{max}^{through} = \frac{FSR}{S}, \tag{4}$$

$$\Delta n_{max}^{MARC} = \frac{FSR_e}{S}, \tag{5}$$

where, Δn_{max} is the maximum detectable refractive index and *FSR* is the free spectral range of the ring resonator given by $\frac{\lambda^2}{n_g 2\pi r}$, where n_g is the group index, λ is the vacuum wavelength and r is the ring radius. FSR_e is the effective free spectral range of the MARC output and is an integer multiple of *FSR* ($FSR_e = N \cdot FSR$). The integer multiple, N, depends on the angular separation between the drop port and the through port waveguides. This is explained in detail in our previous work [14].

As shown in Eq. (4), the measurement range of the through port output is limited by the free spectral range. In contrast to the through port response, the MARC output provides a measurement range that is only partially limited by the free spectral range and can be enhanced by changing the angular separation. Figure 2 illustrates the difference between the measurement range obtained from the through port output and the MARC output, and shows the MARC enhancement of the the measurement range.

Moreover, sensors with large measurement ranges are best suited for multiplexing. For the case of the standard ring resonator sensor, the measurement range depends on the free spectral range, and can be increased by reducing the ring radius. However, a decrease in the ring radius reduces the Q-factor of the ring resonator. In contrast, the MARC sensor with a specific angular
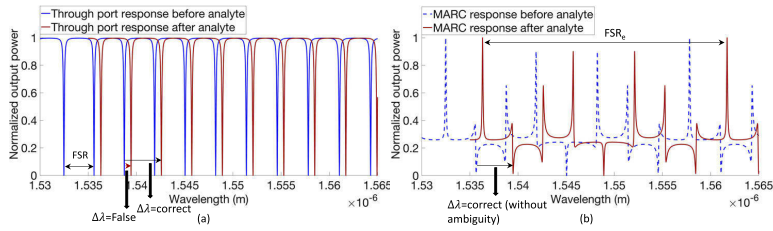
Fig. 2. . (a) Resonance shift measurement using the through port output (standard ring resonator), (b) Resonance shift measurement using the MARC output. The transmission response obtained from the through port output presents a case of false positive when the shift is abrupt and larger than the FSR.

separation can enhance the effective free spectral range of the ring resonator without affecting the Q-factor and can also produce a transmission response with a unique spectral signature. These two features of a MARC can be utilized for multiplexed sensing when distinct rings with varying angular separations are integrated with a balanced Mach-Zehnder interferometer. Figure 3(a) and Fig. 3(b) show the multiplexing of 2 and 3 ring resonators, respectively. For the case of the MARC with 2 rings, a balanced MZI is integrated with 2 ring resonators with different ring radius and angular separations. Rings with different angular separations are used to tag both rings with distinct spectral signatures, which allows easier tracking of resonance shifts for both resonators. Different ring radius reduces the number of overlapping resonances from both rings over a narrow wavelength range.
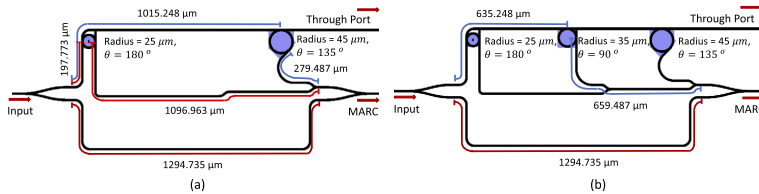
Fig. 3. (a) Schematic of MARC with 2 ring resonators with 180° and 135° angular separation. Radii for these two rings are 25 μm and 45 μm, respectively. (b) Schematic of MARC with 3 ring resonators. For this case, an additional ring resonator with 35 μm ring radius and 90° is integrated with the MARC.

3. Sensor design and fabrication

MARC sensors were designed with silicon strip waveguides, supporting the fundamental TE-like mode at 1550 nm wavelength. Strip waveguides were 500 nm wide and 220 nm high. MARC sensors consisting of a ring resonator with ring radius of 45 μm and angular separation of 135° were designed for measuring the sensitivity and the measurement range. Several MARC sensors were designed with two and three ring resonators. For the case of MARC with 2 ring resonators, two rings with ring radii of 25 μm and 45 μm, and angular separations of 180° and 135° were integrated into a balanced MZI. Similarly, for MARC sensors consisting of 3 ring resonators, a balanced MZI was integrated with three ring resonators with ring radii of 25 μm, 35 μm and 45 μm, and angular separations of 180°, 90° and 135°, respectively. Moreover, input and output

waveguides were designed with inverted tapered silicon waveguides to enhance the coupling efficiency. Inverted taper silicon waveguides were 300 μm long with starting width of 70 nm.

MARC sensors were fabricated on SOI wafers with 220 nm of hydrogenated amorphous silicon on top of the 1 μm thermal oxide layer. Amorphous silicon was deposited on a thermal oxide wafer by plasma enhanced chemical vapor deposition (PECVD) system using SiH4 and Ar gases. Silicon strip waveguides with 500 nm width were patterned by electron beam lithography (Elionix ELS-G100) using e-beam resist (Allresist AR-P 6200). Lithography was followed by dry etching using inductively coupled plasma reactive ion etching (ICP-RIE). SU8 polymer strips were photolithographically patterned on top of silicon inverted tapers. SU8 strips were 300 μm long, 2 μm wide and 2 μm high. The complete chip was covered with 400 nm layer of Polymethyl methacrylate (PMMA) and a small area over the ring resonators was exposed with electron beam lithography to ensure that only the ring resonator interacts with the refractive index change in the surrounding. For controlled flow of solution over each ring resonator in the MARC sensors, three 150 μm wide and 80 μm high microfluidic channels were made on Poly-Di-Methyl Siloxane (PDMS) polymer using soft lithography. For sensing experiments, PDMS microfluidics and the photonic chip were clamped together with an acrylic plate. Figure 4 presents the fabricated MARC sensor clamped with PDMS microfluidics. Note that this fabricated sensor design is suboptimal and only shows a proof-of-principle. Further work involves optimizing the quality factor and the angular separation.
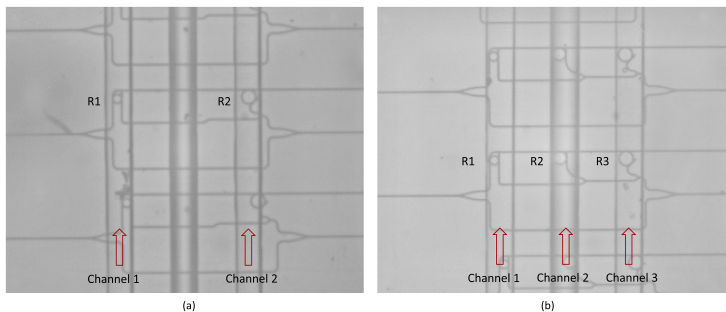
Fig. 4. (a) Fabricated MARC sensor with 2 ring resonators, (b) MARC sensor with 3 ring resonators with different radii and angular separations.

4.　Experimental characterization

For experimental characterization, the photonic chip clamped with the PDMS microfluidics was placed on the translational stage. Solutions with analyte were pumped through the microfluidic channel with the syringe pump at 20 μl/min rate. A tapered lensed fiber with 14 μm working distance and 2.5 μm spot diameter was used to couple light into the waveguide from an external cavity laser (Thorlabs TLK-L1550M) with central wavelength of 1550 nm. A polarization controller (Thorlabs FPC562) was placed between the laser source and tapered fiber to control the polarization of the light from the laser source and to enhance the coupling to the TE-like mode of the waveguides. Two single mode optical fibers connected with InGaAs photodetectors (Thorlabs DET10C2) were placed at the output waveguides to capture the optical power from the through output and the MARC output. Figure 5 presents the transmission spectra obtained from the fabricated MARC with a single resonator with 135° angular separation and ring radius of 45 μm. The transmission response from the through port output presents the standard ring resonance response and shows a Q-factor of 10000 and free spectral range of ~2 nm. The transmission

response from the MARC output presents a unique spectrum consisting of non-identical adjacent resonances unlike the through port response. The effective free spectral range measured from the MARC output was ~16.1 nm, which is 8 times larger than the conventional free spectral range measured from the through port. The measurement range of a ring resonator based-refractive index sensor, the maximum refractive index change that can be detected, is dependent on the free spectral range and challenging to extend without affecting the Q-factor. The measured effective free spectral range from MARC provides larger measurement range to the sensor and without affecting the Q-factor. To analyze this property of the MARC sensor, refractive index sensing measurements were performed on the MARC using saline solutions with varying concentrations. Figure 5(a) shows the transmission spectra from the MARC for deionized water and saline solutions with 6%, 12% and 18% salt concentration. Linear relationship was observed between the resonance shift and saline solution concentration, as shown in Fig. 5(b). The MARC sensitivity was 80.4 pm/% salt and it was calculated from the linear fit of resonance shifts. The error bar in Fig. 5(b) is larger than expected. We believe that this is due to some salt crystallization on the waveguide sidewalls of the two sensors, which were exposed to saline solutions for several hours. The salt crystallization reduced the sensitivity of these two sensors and increased the error bar in the measured resonance shift. As shown in Fig. 5(a), the transmission response from the MARC output clearly shows that the measured shifts are much smaller than the effective free spectral range. The average resonance shift measured for 18% solution was 1.45 nm and it used 72% of the measurement range obtained from the through port output. In contrast this shift utilized only 9% percent of the measurement range provided by the MARC output. Note that during sensing experiments, no TEC controller was used to regulate the chip temperature. All measurements were performed at room temperature. Saline solutions were stored at room temperature.
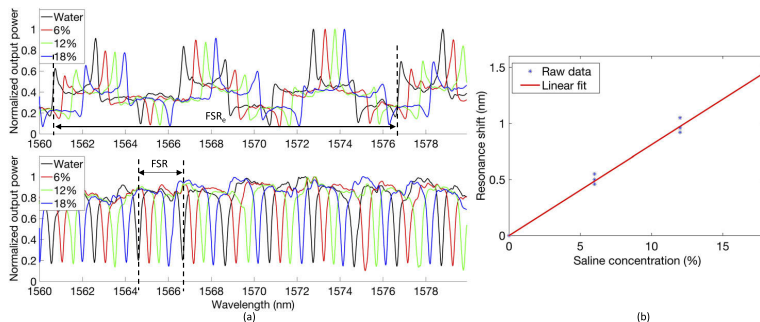
Fig. 5. (a) Transmission response obtained from MARC and through port outputs for different saline solutions, (b) Resonance shift for different saline solutions.

In this paper, in addition to the sensitivity and the measurement range, we also demonstrate the multiplexing capability of the MARC sensor. For the multiplexing experiment, two MARC sensor configurations were fabricated. In one configuration, the MARC sensor was designed to demonstrate multiplexing of two ring resonators. For this configuration, two ring resonators were integrated with a balanced MZI. The other configuration was designed with 3 ring resonators for multiplexing of 3 ring resonators. For the case of the MARC with 2 rings, the ring with 25 μm radius and 180° angular separation was used as a reference sensor and the ring with 45 μm radius and 135° angular separation was used for detecting varying saline concentrations. To improve the accuracy of the measured resonance shift, we measured both the through port output and the MARC output. From the through port output, we extracted precise information on the

resonance shift. Steps followed during the sensing experiment and corresponding measured resonance shifts are presented in Table 1. In step 1, deionized water was flowed over both rings (R1 and R2) to obtain the initial relative resonance shift between responses from both ring resonators. In steps 2-4, deionized water was continuously flowed over ring R1 and saline solutions with increasing concentrations were successively flowed over ring R2. For each saline solution, the relative resonance shift ($\Delta\lambda_{12}$) was measured. From measured relative resonance shifts and initial relative resonance shift, the effective resonance shift ($\Delta\lambda_{eff}$) for each saline solution was calculated and listed in Table 1. The resonance shifts obtained for different saline solutions show linear relationship, which is consistent with measurement results presented in the previous section. Figure 6(a) presents the transmission spectrum obtained from MARC with two rings when deionized water was flowed over both rings. Figure 6(b) shows the transmission obtained when 6% saline solution was flowed over the ring with 135° angular separation. The effective resonance shift was 0.52 nm. From the reference sensor with 180° angular separation, we measured ~20 pm shift after switching the saline solutions in the sensing channel. This shift is probably due to a small temperature difference between the two different solutions. To de-multiplex the responses of two rings from the combined MARC transmission, theoretically estimated responses for each ring were overlayed the combined response.

For the case of the MARC with 3 rings, the ring with 180° angular separation was used as the reference sensor and rings with 90° and 180° were utilized for sensing. Table 2 presents an overview of the sensing experiment performed on the MARC with 3 ring resonators. Resonance shifts from sensing rings when exposed to specific saline solution are listed in the table. Figure 6(c) shows the transmission response obtained when deionized water was flowed over all three rings. Like the MARC with 2 rings, the MARC transmission response was overlayed with theoretically estimated responses for each ring to easily de-multiplex the response from each sensor. Figure 6(d) shows the transmission response obtained when 18% saline solution was flowed over the ring with 135° angular separation and deionized water over the ring with the 90° angular separation. The corresponding resonance shift was 1.52 nm. The measurement results from the MARC with two and three rings clearly show that by combining several rings (with different angular separation and radius) with a balanced MZI allows easier multiplexing of ring resonator sensors. In addition, the reference sensor from the MARC with 2 rings and 3 rings showed a resonance shift of ~20 pm. This shift is less than 5% of the shift from the 6% saline solution, which shows that the set-up was stable without a TEC. However, the temperature stability of the set-up could be further improved by utilizing a TEC controller.

**Table 1. Overview of sensing experiments
performed on the MARC with two ring resonators.**

Steps	R1 (180°)	R2 (135°)	$\Delta\lambda_{12}$	$\Delta\lambda_{eff}$
1	water	water	1.08 nm	
2	water	6%	1.6 nm	0.52 nm
3	water	12%	2.07 nm	0.99 nm
4	water	18%	2.57 nm	1.49 nm

**Table 2. Overview of sensing experiments performed on the MARC with three
ring resonators.**

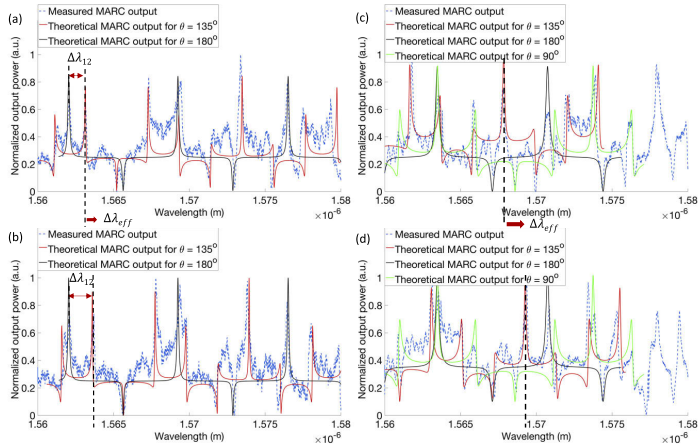| Steps	R1 (180°)	R2 (90°)	$\Delta\lambda_{12}$	$\Delta\lambda_{eff}$	R3 (135°)	$\Delta\lambda_{13}$	$\Delta\lambda_{eff}$
1	water	water	1.05 nm		water	0.69 nm	
2	water	water	1.05 nm		18%	2.21 nm	1.52 nm
3	water	18%	2.57 nm	1.52	18%	2.21 nm	1.52 nm

Fig. 6. Measured transmission response from multiplexed MARC sensors. (a) Multiplexed response from the MARC with two rings cladded with deionized water, (b) when ring with 135° angular separation was cladded with 6% saline solution, (c) Measured response from the MARC with 3 rings cladded with deionized water, (d) when ring with 135° angular separation was covered with 18% saline solution.

5. Discussion

MARC design presents a unique way to enhance the measurement range and improve multiplexing capability of a ring resonator based sensor. In the presented work, the measurement range was demonstrated only for a few configurations, and it can be further enhanced by tuning the angular separation. For multiplexing, the number of ring resonators in a MARC sensor can be further increased by improving the quality factor of individual ring resonators. Enhancement in the quality factor will reduce the intensity overlap between adjacent resonances and improve the distinguishability of response from different resonators multiplexed together. We expect that with further tuning of the angular separation and optimization of the quality factor, the measurement range and the multiplexing capability of MARC sensor will exceed the presented experimental results. Interrogation complexity will also increase with an increase in number of multiplexed sensors. Signal processing or pattern recognition techniques would be required to identify the spectral response from different sensors.

6. Conclusion

We have experimentally demonstrated a multiplexed MARC sensor with a large measurement range. For a MARC sensor with 45 μm ring radius, the measurement range was ~16.1 nm which is 8 times larger than for a standard ring resonator sensor. In contrast to the standard ring resonator sensor, large measurement range was obtained without affecting the intrinsic Q-factor of the ring resonator. In addition to the enhancement in the measurement range, the transmission response from MARC for a specific angular separation provides a unique spectral signature. These spectral signatures were experimentally utilized to demonstrate the multiplexing capability of the MARC sensor. The large measurement range and the multiplexing capability of the MARC sensor makes the sensor very suitable for high throughput sensing for numerous applications.

Disclosures. M.Y. and A.A. have applied for patent GB2004009.3 for optical sensing apparatus.

Data availability. Data underlying the results presented in this paper are not publicly available at this time but may be obtained from the authors upon reasonable request.

References

1. H. M. Robison and R. C. Bailey, "A guide to quantitative biomarker assay development using whispering gallery mode biosensors," Curr. protocols chemical biology **9**(3), 158–173 (2017).
2. T. Claes, J. G. Molera, K. De Vos, E. Schacht, R. Baets, and P. Bienstman, "Label-free biosensing with a slot-waveguide-based ring resonator in silicon on insulator," IEEE Photonics J. **1**(3), 197–204 (2009).
3. K. De Vos, I. Bartolozzi, E. Schacht, P. Bienstman, and R. Baets, "Silicon-on-insulator microring resonator for sensitive and label-free biosensing," Opt. Express **15**(12), 7610–7615 (2007).
4. C. F. Carlborg, K. B. Gylfason, A. Kazmierczak, F. Dortu, M. J. Ba nuls Polo, A. Maquieira Catala, G. M. Kresbach, H. Sohlström, T. Moh, L. Vivien, J. Popplewell, G. Ronan, C. A. Barrios, G. Stemme, and W. van der Wijngaart, "A packaged optical slot-waveguide ring resonator sensor array for multiplex label-free assays in labs-on-chips," Lab Chip **10**(3), 281–290 (2010).
5. R. Heideman and P. Lambeck, "Remote opto-chemical sensing with extreme sensitivity: design, fabrication and performance of a pigtailed integrated optical phase-modulated mach–zehnder interferometer system," Sens. Actuators, B **61**(1-3), 100–127 (1999).
6. R. Heideman, R. Kooyman, and J. Greve, "Performance of a highly sensitive optical waveguide mach-zehnder interferometer immunosensor," Sens. Actuators, B **10**(3), 209–217 (1993).
7. P. Prabhathan, V. Murukeshan, Z. Jing, and P. V. Ramana, "Compact soi nanowire refractive index sensor using phase shifted bragg grating," Opt. Express **17**(17), 15330–15341 (2009).
8. E. Luan, H. Yun, M. Ma, D. M. Ratner, K. C. Cheung, and L. Chrostowski, "Label-free biosensing with a multi-box sub-wavelength phase-shifted bragg grating waveguide," Biomed. Opt. Express **10**(9), 4825–4838 (2019).
9. T. Claes, W. Bogaerts, and P. Bienstman, "Experimental characterization of a silicon photonic biosensor consisting of two cascaded ring resonators based on the vernier-effect and introduction of a curve fitting method for an improved detection limit," Opt. Express **18**(22), 22747–22761 (2010).
10. Y. Zhang, J. Zou, Z. Cao, and J.-J. He, "Temperature-insensitive waveguide sensor using a ring cascaded with a mach–zehnder interferometer," Opt. Lett. **44**(2), 299–302 (2019).
11. X. Jiang, Y. Chen, F. Yu, L. Tang, M. Li, and J.-J. He, "High-sensitivity optical biosensor based on cascaded mach–zehnder interferometer and ring resonator using vernier effect," Opt. Lett. **39**(22), 6363–6366 (2014).
12. W. Bogaerts, P. De Heyn, T. Van Vaerenbergh, K. De Vos, S. Kumar Selvaraja, T. Claes, P. Dumon, P. Bienstman, D. Van Thourhout, and R. Baets, "Silicon microring resonators," Laser Photonics Rev. **6**(1), 47–73 (2012).
13. A. L. Washburn, L. C. Gunn, and R. C. Bailey, "Label-free quantitation of a cancer biomarker in complex media using silicon photonic microring resonators," Anal. Chem. **81**(22), 9499–9506 (2009).
14. M. Yadav, J. W. Noh, D. R. Hjelme, and A. Aksnes, "Spectral shaping of ring resonator transmission response," Opt. Express **29**(3), 3764–3771 (2021).

6.3 Paper III

Biocompatible bonding of a rigid off-stoichiometry thiol-ene-epoxy polymer microfluidic cartridge to a bio-functionalized silicon biosensor

Biocompatible bonding of a rigid off-stoichiometry thiol-ene-epoxy polymer microfluidic cartridge to a biofunctionalized silicon biosensor

Linda Sønstevold[1,*] ⦿, Mukesh Yadav[2], Nina Bjørk Arnfinnsdottir[2],
Aina Kristin Herbjørnrød[1], Geir Uri Jensen[1], Astrid Aksnes[2] and Michal Marek Mielnik[1]

[1] SINTEF Digital, Microsystems and Nanotechnology (MiNaLab), Gaustadalléen 23C, 0373 Oslo, Norway
[2] Department of Electronic Systems, Norwegian University of Science and Technology, O. S. Bragstads plass 2, 7034 Trondheim, Norway

E-mail: linda.sonstevold@sintef.no

CrossMark

Abstract
Attachment of biorecognition molecules prior to microfluidic packaging is advantageous for many silicon biosensor-based lab-on-a-chip (LOC) devices. This necessitates biocompatible bonding of the microfluidic cartridge, which, due to thermal or chemical incompatibility, excludes standard microfabrication bonding techniques. Here, we demonstrate a novel processing approach for a commercially available, two-step curable polymer to obtain biocompatible ultraviolet initiated (UVA)-bonding of polymer microfluidics to silicon biosensors. Biocompatibility is assessed by UVA-bonding to antibody-functionalized ring resonator sensors and performing antigen capture assays while optically monitoring the sensor response. The assessments indicate normal biological function of the antibodies after UVA-bonding with selective binding to the target antigen. The bonding strength between polymer and silicon chips (non-biofunctionalized and biofunctionalized) is determined in terms of static liquid pressure. Polymer microfluidic cartridges are stored for more than 18 weeks between cartridge molding and cartridge-to-silicon bonding. All bonded devices withstand more than 2500 mbar pressure, far exceeding the typical requirements for LOC applications, while they may also be de-bonded after use. We suggest that these characteristics arise from bonding mainly through intermolecular forces, with a large extent of hydrogen bonds. Dimensional fidelity assessed by microscopy imaging shows less than 2% shrinkage through the molding process and the water contact angle is approximately 80°. As there is generally little absorption of UVA light (365 nm) in proteins and nucleic acids, this UVA-bonding procedure should be applicable for packaging a wide variety of biosensors into LOC systems.

1. Introduction

Recent progress in lab-on-a-chip (LOC) technology unveils
an increasing interest and need for integration of several sub-
components, often manufactured in different materials, into
one functional system (Mielnik *et al* 2013, Andreassen and
Mielnik 2014, Valera *et al* 2016, Lindsay *et al* 2018, Chen
et al 2021, Dornhof *et al* 2022). In many respects, the idea
of realizing monolithic systems (system-on-chip) is being
abandoned, gradually shifting towards a more heterogeneous
(system-in-package) approach. This shift is fueled by applic-
ations which require ever more functional systems, like novel
diagnostic devices comprising biosensors and microfluidics,
and the acknowledgement that no single material or fabrica-
tion technology alone can fulfill all needs.

A large group of biosensors are those where the transducer
is manufactured by silicon micro- and nanofabrication tech-
nologies (Luan *et al* 2018, Poghossian and Schöning 2021).
Packaging of such biosensors into LOC devices is particularly
challenging since the transducer must be functionalized with
a biorecognition molecule to complete the biosensor. If pack-
aging is performed as the first step, i.e. prior to biofunctional-
ization, it limits the multiplexing capabilities and substantially
complicates the biofunctionalization procedure (Leichlé *et al*
2012). Biofunctionalization prior to biosensor packaging, on
the other hand, poses challenging process requirements; the
packaging must not compromise the biological activity of the
attached biomolecules. This means that most standard micro-
fabrication bonding techniques, which typically require high
temperatures, non-biocompatible chemicals, or plasma activ-
ation (Taklo 2002), are not applicable (Lepock *et al* 1993,
Leichlé *et al* 2012). These packaging challenges are substan-
tially limiting the adoption of biosensors into commercial util-
ization in novel diagnostic devices.

Common methods for biocompatible biosensor packaging[3]
in research include clamping of microfluidic structures either
molded in soft materials like polydimethylsiloxane (PDMS)
or cut in polymer sheets like Mylar (Washburn *et al* 2010).
Application of pressure sensitive adhesives to bond structured
polymer (e.g. cut or milled) onto the biosensor die (Kratz
et al 2019) is another common approach. Cutting or milling
microfluidic structures from polymer sheets drastically limits
design opportunities, and clamping solutions are prone to leak-
age. To fully exploit the potential of microfluidics to enhance

the performance of LOC systems, the package fabrication
process should allow integration of complex micro- and nan-
ofluidic patterns. This is feasible with PDMS molding, but the
material possesses several intrinsic properties that complic-
ate its use in LOC systems. Examples are absorption of small
hydrophobic molecules and high gas permeability causing gas
bubble formation and evaporation over the time course of an
experiment (Sticker *et al* 2015). Another important downside
of PDMS is that high volume production and commercializa-
tion are hindered by up-scaling difficulties and low fabrication
throughput (Volpatti and Yetisen 2014).

Another group of moldable polymers utilized for micro-
fluidic applications are thiol-enes (Bartolo *et al* 2008, Bong
et al 2012), off-stoichiometry thiol-enes (referred to as 'oste'
in many publications) (Carlborg *et al* 2011, Saharil *et al* 2012,
Pardon *et al* 2014) and off-stoichiometry thiol-ene-epoxies
(referred to as 'oste+' in many publications) (Carlborg *et al*
2014, Sandström *et al* 2015, Sticker *et al* 2015), solving
some of the challenges of PDMS. They offer e.g. direct dry-
bonding to surfaces like silicon and glass, low gas permeab-
ility, tuneable mechanical properties from rigid to rubbery
states, tuneable surface properties with permanent surface
modifications, and are compatible with both prototyping and
medium-scale volume manufacturing. For a closer descrip-
tion of off-stoichiometry thiol-ene and off-stoichiometry thiol-
ene-epoxy polymers, see Haraldsson *et al* (2014) and the
references above.

Off-stoichiometry thiol-ene-epoxies are particularly useful
for LOC technology as they are cured in two stages first form-
ing a soft mold replicate, which after alignment to a substrate
is cured to form a rigid bonded polymer. However, most work
with this type of polymer including the commercially avail-
able resins (OSTEMER 322 Crystal Clear n.d., OSTEMER
324 Flex n.d.) perform bonding at non-biocompatible temper-
atures. In the work by Zhou *et al* (2017), an off-stoichiometry
thiol-ene-epoxy resin was used to mold and then UVA-bond
a polymer well-array to a biofunctionalized microarray glass
slide at room temperature. As the resin formulation is not
given, replication to assess its applicability for silicon bio-
sensor packaging is not possible.

In this work we use the commercially available off-
stoichiometry thiol-ene-epoxy resin Ostemer 322 Crystal
Clear (Mercene Labs, Sweden) and demonstrate a novel pro-
cessing approach to obtain biocompatible packaging of a sil-
icon biosensor into a LOC device. We discuss the fabrication
process in detail, assess the physical properties of the device,
and explore in particular how storage time between the first
(thermal) curing step and the bonding step (UVA cure) affects
the bonding strength of the silicon-polymer package. The latter

---

[3] In the context of the present work, 'biocompatible biosensor packaging'
refers to the integration of a biosensor with microfluidics in a manner which
does not deteriorate or corrupt the functionality of antibodies bound to the
biosensor surface.

is an important aspect for convenient use of pre-fabricated devices as well as for commercial utilization. Finally, we apply the packaging approach to antibody-functionalized silicon ring resonator sensors and assess its biocompatibility by running an antigen capture assay after packaging.

2. Materials and methods

2.1. Fabrication

2.1.1. Polymer chip. The polymer microfluidic cartridge was fabricated in the two-component resin Ostemer 322 Crystal Clear (oste322) (Mercene Labs, Sweden). Note that in the fabrication process we have developed the order of the two curing steps of this resin is reversed compared to the procedure provided by the manufacturer. The fabrication and packaging principle is illustrated in figure 1. The starting point is two positive molds milled in polymethyl methacrylate (PMMA) (figures 1(a) and (c)) from which negative PDMS molds (figures 1(b) and (d)) are cast before assembling them to a PDMS reaction injection mold (figure 1(e)) used to fabricate the polymer microfluidic cartridge (figure 1(f)). Details on the fabrication of PMMA and PDMS molds are found in the supplementary information (section S1 (available online at stacks.iop.org/JMM/32/075008/mmedia)). Milled PMMA was used as fabrication master due to the relatively large depths of the chip's features. PDMS was used as an intermediate molding step due to its superior de-bonding properties from oste322 as compared to PMMA, mainly attributed to its mechanical flexibility and low oste322 adherence.

The polymer microfluidic cartridge (figures 1(f) and (g)) was designed with three microfluidic channels (500 μm wide, 100 μm deep). The cartridge has an area of 14 mm × 29 mm and thickness 600 μm. Structures for the direct coupling of external tubing to the microfluidic cartridge—two tube connector arrays—were integrated into the design (thickness 3 mm, area 5.2 mm × 14 mm, inlet holes 2.4 mm diameter). This gives a total polymer thickness of 3.6 mm (3 mm plus 600 μm) at the position of the tube connector arrays.

Oste322 component A and B were mixed in weight ratio 1.09:1 by vortexing in a 30 ml glass vial and left on the bench to evacuate air-bubbles. PDMS mold 1 (figure 1(b)) and 2 (figure 1(d)) were aligned to make the reaction injection mold (figure 1(e)). Due to the relatively large contact area between the two PDMS molds, they adhere sufficiently well to each other without the need for additional mechanical clamping during the subsequent pre-polymer injection and thermal cure. Up to four molds were used in parallel to fabricate four microfluidic cartridges simultaneously. The oste322 pre-polymer was injected using a 5 ml luer-slip syringe, also filling the mold's inlet and outlet holes (figure 1(e)). These will serve as backfilling reservoirs as the oste322 slightly contracts during the first cure (Sandström *et al* 2015). The assembly was baked in an oven at 90 °C until the liquid oste322 pre-polymer had become a solidified but soft material. The time to reach solidification varied between the oste322 batches from 1.5 to 5.5 h. To evaluate the onset of solidification without opening the reaction injection mold, a simple PDMS mold with a 1 mm

deep cavity (size of a standard microscope slide) was used in parallel. In this mold, oste322 pre-polymer was poured into the cavity and covered with a release liner (Fluoropolymer coated release liner 9755, 3M™ Scotchpak™). After the thermal cure, the assembly was completely cooled down before carefully demolding PDMS mold 2. The oste322, still attached to PDMS mold 1, was placed in a holder milled in PMMA (supplementary figure S1). Before transfer the areas of the holder to be in contact with oste322 were covered with release liner. PDMS mold 1 was carefully removed and excess oste322 cut away with a scalpel leaving only the structure of the final polymer microfluidic cartridge (figure 1(f)). After this, the oste322 cartridge was either bonded to the silicon chip at once, or it was covered with release liner and stored at room temperature protected from light for 1, 2, 4 and 18 weeks prior to bonding to assess the suitability for storage of prefabricated oste322.

2.1.2. Silicon chip. To assess the biocompatibility of the packaging procedure, ring resonator sensors were fabricated on silicon-on-insulator wafers, biofunctionalized with antibodies and covered with DryCoat (Virusys Corporation) before bonding. The chips were 14 mm by 29 mm with a ring resonator layout matching the microfluidic channel design of the polymer cartridge. The design and fabrication of the ring resonator sensors, biofunctionalization procedure and application of DryCoat are described in detail in the supplementary information (section S3).

In addition, non-structured silicon chips (blank chips) were prepared for assessment of bonding strength. Silicon wafers ($\langle 100 \rangle$ 675 μm thickness, Topsil) were thermally oxidized (7615 Å) before dicing (14 mm × 29 mm chips). Directly before bonding to oste322 the blank silicon chips were cleansed by ultrasonication for 5 min in acetone, then isopropanol, then deionized water, rinsed three times in deionized water and blown dry with dry filtered air.

2.1.3. Bonding. The bonding and the second curing step of oste322 happens simultaneously (figures 1(f) and (g)). The silicon chip was aligned to the thermally cured oste322 held in the PMMA holder. The assembly consisting of the silicon chip, the oste322 and the release liner was lifted from the holder, and air-bubbles were removed by applying pressure with a blunt tool on top of the protective release liner on the oste322. No clamping between the oste322 and silicon chip was necessary to retain surface contact during UVA exposure. Release liner pieces on the tube connector arrays were removed before exposure to UVA-light (Dymax light curing systems, model 1200 focused beam, UVA-range intensity (320–390 nm) 350 mW cm^{-2}) for 2 × 2 s with 20 s pause between exposure steps with aluminum foil covering the 0.6 mm thick part of the oste322. The aluminum foil and last release liner piece were removed to expose the entire oste322 device for an additional 2 × 2 s with a 20 s pause. This gave a total of 8 s UVA exposure for the 3.6 mm thick part and 4 s for the 0.6 mm thick part to fully cure and bond all parts of the device while not overexposing.
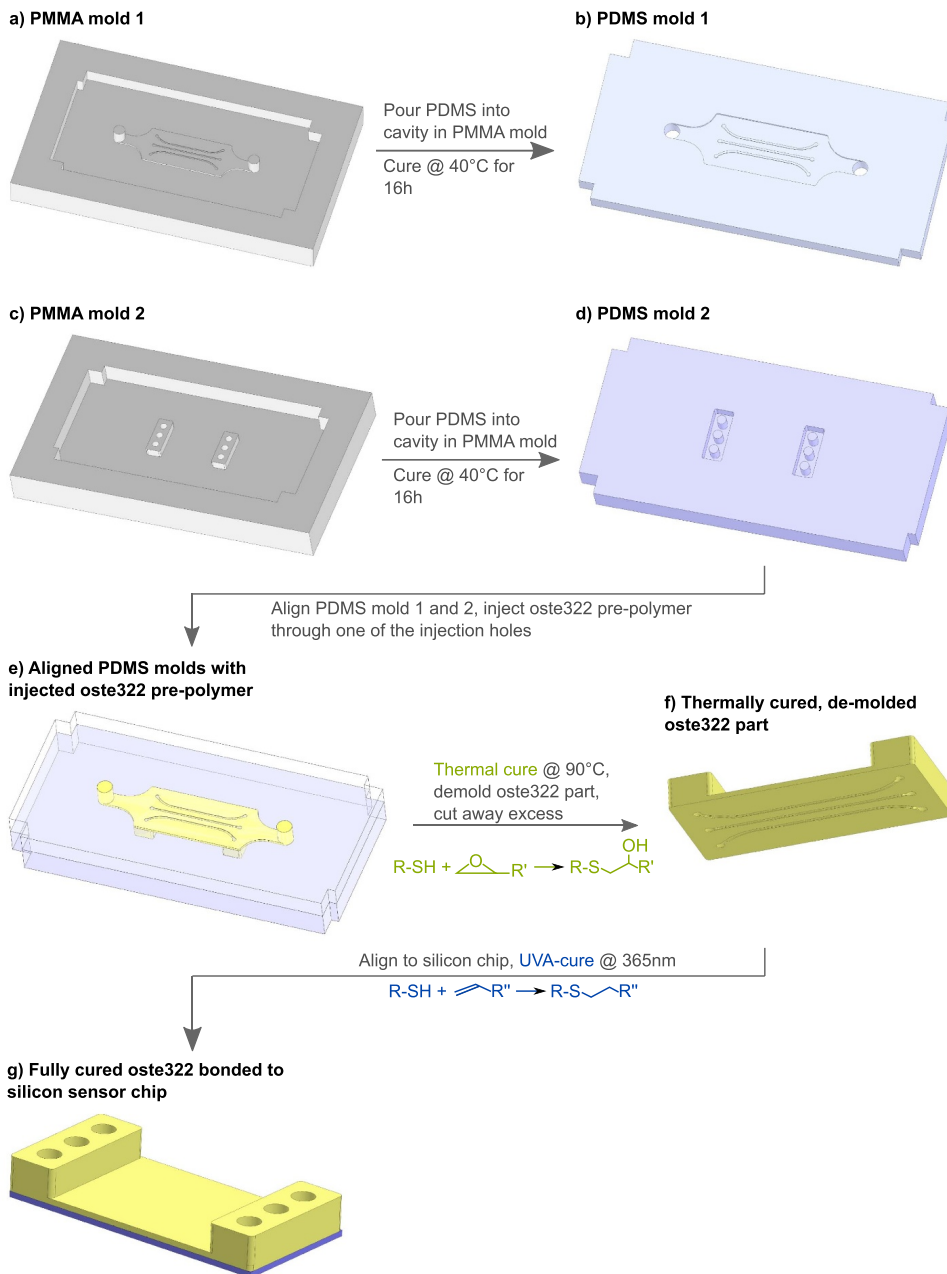
Figure 1. Fabrication procedure (a)–(g). Schematic illustration of the fabrication procedure developed to mold and then biocompatibly UVA-bond oste322 microfluidic cartridges to silicon sensor devices. (a) and (c) Positive molds are milled in PMMA. (b) and (d) Negative PDMS molds are cast from the PMMA-molds. (e) The PDMS molds are assembled to form a reaction injection mold and oste322 pre-polymer is injected before a thermal cure at 90 °C where thiol and epoxy groups react. (f) The soft intermediate oste322 is demolded, excess structures from the molding process are cut away, (g) the oste322 is aligned to the silicon sensor and UVA light initiates the second cure where thiol and allyl groups react, resulting in a rigid polymer which is bonded to the silicon sensor chip. Details of the fabrication procedure are found in section 2.1.

Table 1. Bonding strength characterization. Overview of experimental parameters (light gray) and results (dark gray) for the characterization of bonding strength between the silicon chip and polymer microfluidic cartridge. Experiments were performed with two technical replicates.

Silicon chip type	Oste322 stored on release liner	Storage time	Tolerates 500 mbar	Tolerates 2500 mbar
Blank	No	No storage	Yes	Not tested
Blank	Yes (contacted)	No storage	Yes	Yes
Blank	Yes	1 week	Yes	Not tested
Blank	Yes	2 weeks	Yes	Not tested
Blank	Yes	4 weeks	Yes	Yes
Blank	Yes	18 weeks	Yes	Yes
Biofunctionalized ring resonator chip	No	No storage	Yes	Yes

For the biofunctionalized ring resonator chips, the DryCoat was removed by immersion in deionized water before oste322 bonding. After bonding, DryCoat was injected into the microfluidic channels, incubated for 1 min, and removed before further storage at 4 °C. To assess the effect of the bonding procedure on antibody function, one un-functionalized ring resonator chip was bonded to oste322. On this chip the biofunctionalization (section 2.1.2) and antigen capture assay (section 2.3) were performed in one continuous run.

2.2. Physical characterization

The bonding strength between the silicon chip and polymer microfluidic cartridge was determined in terms of static liquid pressure with a set-up as illustrated in supplementary figure S2. A syringe pump (Harvard Apparatus PHD2000) was connected to the inlet, while a pressure sensor (GD4200, ESI Technology Ltd) was connected to the outlet of a channel in the silicon-polymer package. Deionized water was filled into the silicon-polymer package before connecting the pressure sensor. The syringe pump was run at constant flow rate between 200 and 500 μl min^{-1} while using a stereomicroscope with a large field of view covering the entire silicon-polymer package for optical monitoring of leakage. In addition to real-time visual inspection, images were acquired throughout the experiments and digitally analyzed to identify potential minor leaks. All packages were tested up to 500 mbar, while a selection was tested to 2500 mbar (overview in table 1). Up to 500 mbar the silicon polymer package was connected by polytetrafluoroethylene (PTFE)-tubing (ID: 0.3 mm, OD: 1.6 mm, VWR) with a silicone tubing sleeve (ID: 1.02 mm, OD: 2.16 mm, VWR), inserted into the inlet holes in the tube connector arrays. Above 500 mbar gluing was necessary to achieve a leak-tight connection between chip and tubing. All pressure values refer to gauge pressure.

Topographical measurements of PMMA mold 1 and the oste322 bond surface (after bonding) were done using white light interferometry (WYKO NT9800, Veeco). Arithmetic average surface roughness, R_a, was calculated by:

$$R_\mathrm{a} = \frac{1}{n} \sum_{i=1}^{n} |Z_i - \bar{Z}| \qquad (1)$$

where Z_i is the vertical height of grain i and $\bar{Z}$ the average grain height. Reported values for R_a (average $\pm$ standard deviation), in addition to average and maximum peak-to-valley roughness, are based on analyzing in total 5 mm $\times$ 6.8 mm of the surfaces.

The water contact angle was measured by pipetting 40–180 μl deionized water on the top surface of the polymer microfluidic cartridge, imaging and measuring the left and right contact angles.

Dimensional fidelity in the two-step molding process was assessed by fabrication of an oste322 device with integrated herringbone mixing structures in the upper microfluidic channel wall. To fabricate this device, we used a photolithography defined SU-8 mold to define the microfluidic structures and a milled PMMA mold to define the outer dimensions of the microfluidic cartridge. Fabrication of this cartridge is described in the supplementary information (section S5). Replication of microstructural dimensions from the SU-8 mold to PDMS mold to oste322 cartridge was assessed by microscopy imaging and image analysis. Dimensional fidelity assessment was performed on this device instead of the previously described oste322 cartridge as accurate comparison of dimensions are better allowed by the fine photolithography patterns and accurate dimensional replication is crucial for the function of such mixing structures.

All imaging was performed using an Olympus SZX10 stereomicroscope (assessing bonding strength and contact angle) or Olympus BX-61 microscope (assessing dimensional fidelity), Olympus XM10 camera and cellSens Dimension software (Olympus) for image analysis.

2.3. Biocompatibility of the packaging procedure

To assess the biocompatibility of the packaging procedure, antibody-functionalized ring resonator sensors were packaged (described in section 2.1) prior to running an antigen capture assay in the LOC devices. The experimental set-up is illustrated in figure 2. For optical characterization, a tapered lensed fiber with 14 μm working distance and 2.5 μm spot diameter was used to couple light into the waveguide. A tunable external cavity laser (Thorlabs TLK-L1550M) with 1550 nm center wavelength was used as the light source. A fiber polarization controller (Thorlabs FPC562) was placed between the light source and the tapered fiber to control the input polarization
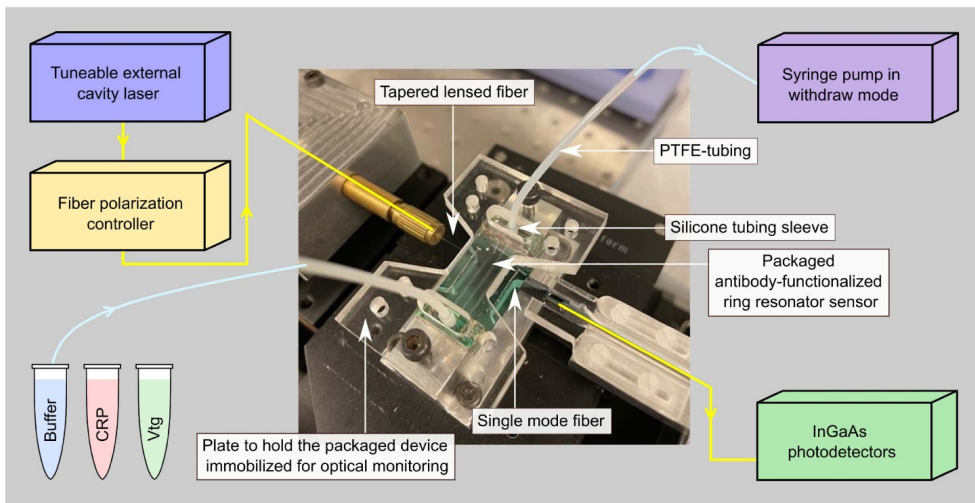
Figure 2. Optical-microfluidic experimental set-up to test packaging biocompatibility. The set-up was used to test the antibody functionalized ring resonator sensors that were packaged with the polymer microfluidic cartridge. The reagents of the antigen capture assay were pumped through the microfluidic channel during continuous optical monitoring of the sensor response to record binding events on the sensor surface, to assess the biological function of the antibodies after packaging. The yellow and light blue lines illustrate the optical and fluidic pathways, respectively. The experimental procedure is described in section 2.3.

of the light. A single mode fiber connected to InGaAs photodetectors (Thorlabs DET10C2) was placed in front of the output waveguide to capture the output power from the resonators. For fluidic operation, a syringe pump (Harvard Apparatus Pump 11 Pico Plus Elite) in withdraw mode was used. The syringe pump and reagent vials were connected to the LOC device by PTFE-tubing with a silicone tubing sleeve. The antigen capture assay was performed as follows at flow rate 20 μl min^{-1}; (a) 5 min buffer, (b) 15 min 5 μg ml^{-1} CRP (control antigen, C-reactive protein, SigmaAldrich) in buffer, (c) 5 min buffer, (d) 20 min 5 μg ml^{-1} Vtg (target antigen, Vitellogenin, Biosense Laboratories) in buffer, (e) 5 min buffer ('buffer' = PBS (phosphate buffered saline, SigmaAldrich) with 5 mg ml^{-1} BSA (bovine serum albumin, SigmaAldrich)). Small deviations to the time length of each step occurred due to fluidic operation considerations. During the antigen capture assay the laser was scanned across the selected resonance, and wavelength vs power for each sweep was stored in a separate file with the time stamp. After the measurements, Lorentzian fitting was performed on each wavelength sweep to extract the information about the resonance wavelength. Resonance wavelengths were then plotted against time stamps.

3. Results and discussion

3.1. Fabrication procedure

In this work we have used the commercial polymer Ostemer 322 Crystal Clear (oste322) (Mercene Labs, Sweden) and processed it in a novel manner to obtain biocompatible packaging of a silicon biosensor into a LOC device. Oste322 is a two-component resin, an off-stoichiometry thiol-ene-epoxy

made specifically for the requirements of microfluidics, microelectro-mechanical systems (MEMS) and LOC (OSTEMER 322 Crystal Clear n.d.). As opposed to PDMS it is slightly hydrophilic (Sandström *et al* 2015) and has low water vapor permeability (Sticker *et al* 2015). Fabrication of devices rely on a two-step polymerization reaction where the liquid prepolymer solidifies to a soft intermediate state replicating the mold structure in the first curing step initiated by UVA light (365 nm). The oste322 is then demolded and aligned to the substrate before the second curing step initiated by heat (90 °C–110 °C). This makes the polymer rigid like typical thermoplastics and simultaneously covalently bonded to the substrate (OSTEMER 322 Crystal Clear n.d.). Since this last curing step where the oste322 device bonds to the substrate takes place at 90 °C–110 °C, it is not appropriate for packaging biofunctionalized sensors as the biomolecules would denature. There is little absorption of UVA light at 365 nm in proteins and nucleic acids (de Gruijl 2000, Ravanat *et al* 2001, Porterfield and Zlotnick 2010, Rastogi *et al* 2010). Therefore, we hypothesized that we could obtain a biocompatible LOC packaging procedure if we were able to achieve proper curing and bonding of oste322 when reversing the order of the two curing steps.

When reversing the curing order (reverse cure) compared to that specified by the manufacturer (standard cure), finding appropriate thermal curing conditions required comprehensive experimentation. Differences between oste322 batches from the manufacturer complicated the matter, but there was consistency within batches. We concluded that the best approach for the thermal cure was to always use 90 °C temperature and adapt the curing time for each oste322 batch. We found the curing times to be independent of oste322 device thickness.

We achieved similar end results for all oste322 devices when utilizing this approach. Whether the first cure was a thermal or UVA cure, the physical appearance of the oste322 was similar; a soft, slightly sticky intermediate state with softness resembling cured PDMS. During storage of the thermally cured oste322 protected from light for up to 18 weeks the material gradually became less sticky and less soft.

The stickiness faded most rapidly, and after 4 weeks the oste322 was no longer sticky. The softness gradually decreased, but even after 18 weeks the oste322 was still soft enough to easily bend and adhere to the silicon chip surface.

The UVA cure could be performed with the same UVA exposure regime for all batches of oste322. The appropriate regime was found by performing the UVA cure as the first cure and exposing 2 s at a time until the pre-polymer solidified. Using reaction injection molds was very useful for these experiments as the oste322 device thickness was constant, and the appropriate UVA dose depends on oste322 thickness. Since the oste322 device has one area with thickness 0.6 mm and two areas with thickness 3.6 mm, they were exposed for different times to avoid overexposure of the thin area. The exposure was divided into repeating intervals of 2 s exposure followed by 20 s pause since the UVA-initiated reaction is exothermic (Datasheet Ostemer 322 Crystal Clear, Mercene Labs AB, 2019). If measures are not taken to limit the temperature increase during this exothermic reaction, this step might also cause thermal denaturation of the antibodies bound to the sensor surface. We found that separating the total exposure time in intervals of 2 s with 20 s resting time between exposures sufficiently reduced the heat generation to avoid antibody denaturation. If working with biosensors functionalized with more temperature-sensitive biomolecules, the silicon-polymer package may be cooled down while performing the UVA exposure.

After both curing steps of the reverse cure, the oste322 physical appearance is the same as after the full standard cure; it is hard and rigid like a typical thermoplastic. However, the bonding characteristics are different. Whereas the standard curing order results in a silicon-polymer package which is covalently bonded together, the reverse curing order results in a package which may be de-bonded after use (figures 3(a) and (b)). Although de-bondable, the reverse cured packages withstand more than 2500 mbar of fluidic pressure (see section 3.2.1), more than enough for most microfluidic applications. This combination of properties is very useful in LOC research as the silicon sensor die may be re-used or inspected with techniques requiring free access to the surface.

The reason for the difference in bonding properties for the standard and reverse cure is the chemical formulation of the resin. Oste322 contains three different monomers, each with either a thiol, allyl or epoxy functional group (monomers illustrated in figures 1(e)–(g)). In the standard cure, the first cure initiated by UVA light causes thiol and allyl functional groups to react, and the second cure initiated by heat causes thiol and epoxy functional groups to react (Sandström *et al* 2015). The covalent bonding of oste322 to silicon during the thermal cure is caused by the epoxy groups forming covalent bonds to hydroxyl groups on the silicon/silicon oxide
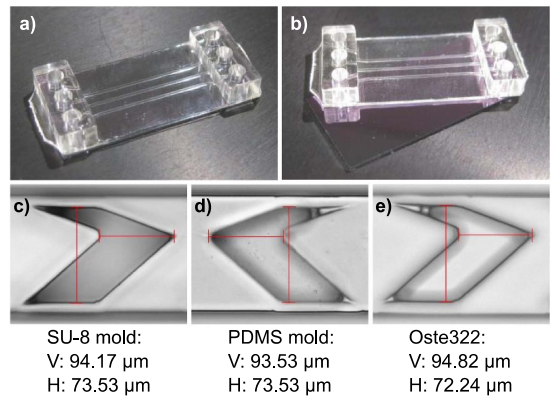

Figure 3. Final silicon-polymer package and dimensional fidelity assessment. (a) Image of the final bonded silicon-polymer package. (b) Image of the silicon-polymer package after de-bonding. (c)–(e) Dimensional fidelity throughout the two-step molding process from the SU-8 mold to PDMS mold to oste322 was assessed by measurement of the vertical (V) and horizontal (H) red lines in the microscope images. The width of the mixing pattern (vertical line; approximately 94 μm) is smaller than the mask design of 100 μm due to the double-layer SU-8 photolithography process.

surface (Datasheet Ostemer 322 Crystal Clear 2019). When reversing the curing order, the bonding curing step is the one initiated by UVA where thiol and allyl groups react. None of these functional groups form covalent bonds with hydroxyl groups on the silicon substrate. However, the thermal cure reaction of thiol and epoxy results in a product containing a hydroxyl group (figures 1(e) and (f)) (Sandström *et al* 2015). Hence, the thermally cured oste322 aligned to the silicon chip contains thiol, allyl, and hydroxyl functional groups before the UVA cure. Both for the blank (i.e. non-structured and non-biofunctionalized) and the biofunctionalized ring resonator chips the functional groups on the surfaces enable hydrogen bonding and dipole–dipole interactions with the thermally cured oste322 (figure 4). These intermolecular forces only become significant when the involved molecules are physically close together. Since the oste322 is soft and adheres well to the silicon chip, it may conform to the silicon surface topography maximizing intermolecular forces. This is supported by the surface roughness measurements described in section 3.2.1. The slight heat generation caused by the exothermic reaction might assist this action. As the oste322 stiffens after replicating the silicon surface topography, the bonding is also likely enhanced simply by frictional forces. The surface of the blank silicon chips only has hydroxyl functional groups. For the biofunctionalized ring resonator chips the whole surface is covered with BSA protein where the various amino acid side chains introduce several functional groups. By that, the blank silicon chips only enable intermolecular forces, while the biofunctionalized ring resonator chips might also facilitate covalent bonds; since thiol and allyl groups of oste322 react in the UVA cure, allyl groups on oste322 may likely also react with cysteine thiol groups on biofunctionalized sensors, forming covalent bonds.
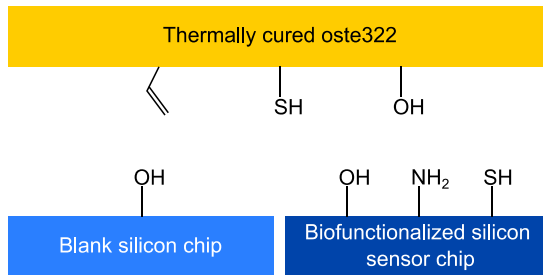
Figure 4. Surface functional groups. Schematic illustration of the surface functional groups on the different bonding surfaces. After the thermal cure, the oste322 surface contains allyl, thiol and hydroxyl functional groups. The blank (i.e. non-structured and non-biofunctionalized) silicon chips have hydroxyl functional groups, forming hydrogen bonds with hydroxyl and dipole–dipole interactions with thiol on oste322. Biofunctionalized silicon sensor chips are blocked with BSA protein where various amino acid side chains introduce various functional groups. Hydroxyl (serine, threonine, tyrosine) and nitrogen-containing (asparagine, glutamine, histidine) functional groups (here illustrated through a primary amine) are mainly responsible for hydrogen bonding at neutral pH to hydroxyl on oste322. Thiol (cysteine) may potentially form covalent bonds with thiol (disulphide bridges) and allyl (UVA-initiated reaction) on thermally cured oste322. In addition dipole–dipole interactions are possible for many amino acid side chains with thiol and hydroxyl on oste322 (not illustrated).

In addition, as there are thiol groups on both the oste322 and the biofunctionalized sensors, there is potential for formation of disulphide bridges.

The bonding of the surfaces by mainly intermolecular forces with a large extent of hydrogen bonds fits well with the observed bonding characteristics. Although intermolecular, when hydrogen bonds are formed over a large area, they become truly significant. This is exemplified e.g. by the deoxyribonucelic acid (DNA) double helix (Watson and Crick 1953) and its great structural stability, combined with the unwinding functionality. Also, as close surface proximity is obtained and there are hydroxyl groups on all bonding surfaces, the bonding mechanism between oste322 and silicon chips likely resembles the pre-bonding step of fusion bonding of hydrophilic silicon wafers (Taklo 2002), exhibiting similar characteristics.

3.2. Physical characterization

3.2.1. Bonding strength.
An overview of the results from investigating the bonding strength between the silicon chip and polymer microfluidic cartridge is found in table 1. All the silicon-polymer packages were tested up to 500 mbar while a selection was tested up to 2500 mbar (gauge pressure). No sign of leakage was observed in any of the tests. The packages could be de-bonded after use, leaving a clean silicon surface (figures 3(a) and (b)). The bond strength tests demonstrate a shelf life of more than 18 weeks between microfluidic cartridge molding and cartridge-to-silicon bonding—a significant advantage for both commercial utilization and research

projects. With microfluidic cartridges in stock, the biofunctionalized silicon sensors may be packaged in minutes when ready to perform a bioassay experiment. During storage, the microfluidic cartridges were covered by release liner to avoid dust accumulation. As evidenced by the bond strength measurements, contact with release liner does not deteriorate the bonding properties of oste322 to an extent that affects the application, i.e. the bond strength of at least 2500 mbar is maintained.

The arithmetic average surface roughness of the master PMMA mold 1 was $R_a = 0.02 \pm 0.09$ μm while the corresponding bonding surface of oste322 had $R_a = 0.02 \pm 0.02$ μm. Three-dimensional surface plots are found in supplementary figure S4. By that, the variation in surface topography is larger in the master mold than in the oste322 product. Average and maximum peak-to-valley roughness was 0.26 and 62 μm for PMMA mold 1, and 0.11 and 8 μm for oste322, respectively. These maximum peak-to-valley values originate from small areas with scratches in PMMA mold 1. As evidenced by the difference between the average and maximum values, they are not representative of the bonding surfaces. As discussed in section 3.1, the oste322 is soft when adhered to the silicon chip and may therefore conform to the very flat silicon surface, reducing the surface roughness and increasing the contact area for bonding. This increases the applicability of the bonding procedure, as cost-efficient molds which often have rougher surface topography may be utilized.

The measurement range of our experimental set-up was limited to 2500 mbar fluidic pressure. As all packages withstood this pressure level we were not able to assess differences in bonding strength for packages with biofunctionalized ring resonator chips and blank silicon chips. From the theoretical possibilities of bond formation discussed in section 3.1, it would be interesting to test whether biofunctionalized ring resonator chips tolerate higher pressures, as they feature the possibility of covalent bonds (thiol–allyl, thiol–thiol), in addition to intermolecular bonds available for both types of chips. However, as also the biofunctionalized ring resonator packages may be de-bonded after use, this implies that covalent bonding, if present, is not the dominant bonding mechanism.

3.2.2. Contact angle.
The contact angle of deionized water with the reverse cured oste322 was found to be approximately 80° (ranging from 73° to 85°). Sandström *et al* (2015) reported a water contact angle of 67° for standard cured oste322, while Zhou *et al* (2017) reported 70 ± 3° using 4 μl droplets of deionized water. The slight increase in contact angle in our experiments could indicate that reversing the curing order slightly increases the water contact angle. However, conclusions are difficult as the contact angle measurements are affected by droplet size, surface roughness and image analysis. Nevertheless, for both the standard and reverse cured oste322, the water contact angle is in the same range—on the slightly hydrophilic side.

3.2.3. Dimensional fidelity.
A valuable feature for LOC biosensors is the integration of microfluidic structures for
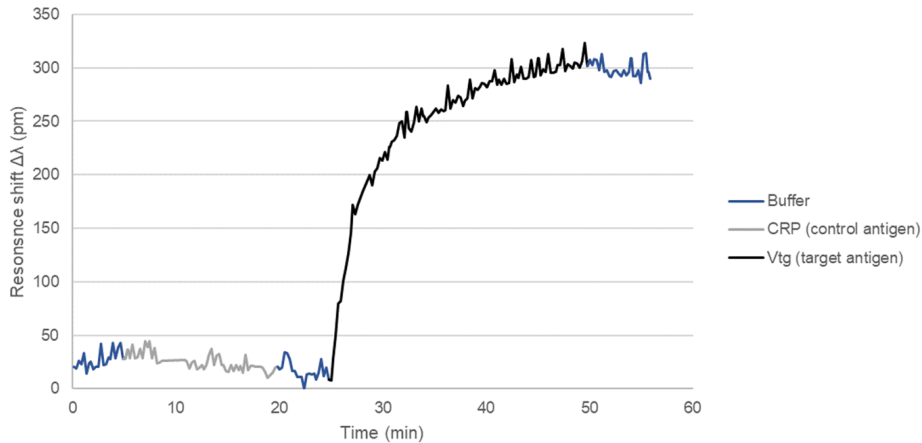
Figure 5. Test of the biocompatibility of the packaging procedure. A plot showing the real-time monitoring of the shift in resonance wavelength ($\Delta\lambda$) of an antibody-functionalized ring resonator sensor after packaging as the different solutions of the antigen capture assay are run through the microfluidic channels, indicated along the time axis. 'Buffer' = PBS with 5 mg ml^{-1} BSA, 'CRP' = 5 μg ml^{-1} C-reactive protein in buffer, 'Vtg' = 5 μg ml^{-1} Vitellogenin in buffer. The graph profile is representative for all experiments with the only difference being the size of the shift varying from approximately 300–400 pm.

advanced flow manipulation. One example is the integration of passive mixing structures to enhance the mass transfer of analyte to the sensing area (Oevreeide *et al* 2021a, 2021b). Feature dimensions are essential for such microfluidic structures. We therefore assessed the dimensional fidelity throughout the two-step molding process for fabrication of such a device. To fabricate the passive mixing structures, the microfluidic geometry was defined by SU-8 photolithography instead of milling. Investigation of dimensions in the photolithography defined SU-8 mold, PDMS mold and oste322 device (figures 3(c)–(e)) shows that dimensions are transferred through the two replication processes with less than 2% shrinkage. Low shrinkage from the SU-8 mold to the PDMS mold is attributed to PDMS curing at low temperature (40 °C) (Madsen *et al* 2014). Our results correspond well with the work of Sandström *et al* (2015) who demonstrate less than 1% shrinkage with oste322 standard cure for structures with comparable dimensions. This indicates that reversing the cure order does not significantly affect shrinkage. We expect similar dimensional fidelity for the PMMA to PDMS to oste322 molding process.

3.3. Biocompatibility of the packaging procedure

To investigate if the biological function of the antibodies was maintained after packaging, antibody-functionalized ring resonator sensors were bonded to oste322 cartridges prior to running an antigen capture assay. The antigen capture assay included a control antigen and a target antigen to assess binding selectivity. The working principle of ring resonator biosensors is explained e.g. in Washburn *et al* (2009). In short, when the antibody bound to the sensor surface binds to another molecule, a shift in the resonance wavelength is observed. A representative measurement from the antigen capture assay is shown in figure 5. When the buffer (5 mg ml^{-1} BSA in PBS)

or 5 μg ml^{-1} control antigen in buffer is run through the channels, we see no resonance shift, indicating no binding. However, as the solution of 5 μg ml^{-1} target antigen in buffer is introduced, the resonance wavelength shifts by approximately 300 pm, indicating antigen binding.

In total, four experimental replicates were performed with ring resonator chips bonded to oste322 after biofunctionalization. In addition, one ring resonator chip was bonded to oste322 before biofunctionalization, performing the biofunctionalization assay and antigen capture assay in one continuous run in the microfluidic channel, as a reference. Thus, in the latter case, the antibodies were not exposed to the packaging procedure. For all experiments, a similar profile as seen in figure 5 was observed for the antigen capture assay, with the size of the resonance shift varying between approximately 300 and 400 pm. For the ring resonator chips biofunctionalized before oste322 bonding, the resonance shifts were 290, 290, 310 and 400 pm. For the ring resonator chip biofunctionalized after oste322 bonding, the shift was 330 pm. The observed variation in resonance shift between technical replicates is within expected levels and can be mainly attributed to the biofunctionalization procedure. It is known that, due to the small sensing area, batch-to-batch differences in number, orientation and monolayer formation of attached antibodies may cause significant differences in antigen capture ability (Arnfinnsdottir *et al* 2020), and hence resonance shifts. Therefore, data from ring resonator biosensors is commonly presented as averages over several technical replicates (Graybill *et al* 2016, Valera *et al* 2016, Arnfinnsdottir *et al* 2020).

The resonance shift profiles indicate normal biological function of the antibodies with selective binding to the target antigen. The shift size is similar for antibodies which have been exposed to the packaging procedure and those which have not. This shows that the developed UVA-based packaging

procedure is in fact biocompatible. There is in general little absorption of light at 365 nm in proteins and nucleic acids (de Gruijl 2000, Ravanat *et al* 2001, Porterfield and Zlotnick 2010, Rastogi *et al* 2010), and therefore we expect similar results for all such biorecognition molecules. By that, this packaging procedure should be applicable for packaging a variety of biosensors into LOC systems.

4. Conclusions

In this work, we have presented a new procedure which permits packaging of pre-biofunctionalized silicon sensors into a LOC system. We have shown that the packaging procedure does not compromise the biological function of the attached biomolecules. The polymer microfluidic cartridge is bonded to the silicon biosensors (as opposed to clamped) and can withstand pressures higher than 2500 mbar which far exceeds the typical pressure requirements for most LOC applications. This eliminates the widespread problem of leakage in clamped systems. Additionally, the bonding is reversible allowing disintegration of the microfluidic package for free access to the sensor surface or re-use of the silicon sensor.

The polymer cartridge is fabricated by reaction injection molding using oste322. When fully cured, it forms a rigid, slightly hydrophilic polymer (wetting angle approximately 80°) which has several advantages over the commonly used soft and hydrophobic PDMS. The fabrication process based on molding is suitable for upscaling, and it allows integration of complex microfluidic patterns permitting full utilization of the microfabrication design potential to enhance the performance of biosensor systems. In addition, the microfluidic cartridge may be stored for more than 18 weeks before bonding, which drastically simplifies the logistics of the fabrication workflow.

In summary, this procedure overcomes many of the obstacles for microfluidic packaging of biosensors both for research and commercialization. By further developing this procedure for upscaled fabrication, we believe it could become an important contribution to the development and application of novel silicon biosensor-based diagnostic devices.

Data availability statement

The data that support the findings of this study are available upon reasonable request from the authors.

Acknowledgments

ORCID iD

Linda Sønstevold ⬤ https://orcid.org/0000-0003-0387-219X

References

Andreassen E and Mielnik M M 2014 *ESTC 2014–5th Electron. Syst. Technol. Conf.* (https://doi.org/10.1109/ESTC. 2014.6962736)

Arnfinnsdottir N B, Chapman C A, Bailey R C, Aksnes A and Stokke B T 2020 *Sensors* **20** 3163

Bartolo D, Degré G, Nghe P and Studer V 2008 *Lab Chip* **8** 274–9

Bong K W, Xu J, Kim J-H, Chapin S C, Strano M S, Gleason K K and Doyle P S 2012 *Nat. Commun.* **3** 805

Carlborg C F, Haraldsson T, Öberg K, Malkoch M and van der Wijngaart W 2011 *Lab Chip* **11** 3136

Carlborg C F, Vastesson A, Liu Y, van der Wijngaart W, Johansson M and Haraldsson T 2014 *J. Polym. Sci.* A **52** 2604–15

Chen X, Ning Y, Pan S, Liu B, Chang Y, Pang W and Duan X 2021 *ACS Sens.* **6** 2386–94

de Gruijl F R 2000 *Meth. Enzymol.* **319** 359–66

Dornhof J, Kieninger J, Muralidharan H, Maurer J, Urban G A and Weltin A 2022 *Lab Chip* **22** 225–39

Graybill R M, Para C S and Bailey R C 2016 *Anal. Chem.* **88** 10347–51

Haraldsson T, Carlborg C F and van der Wijngaart W 2014 *Proc. SPIE* **8976** 897608

Kratz S R A, Eilenberger C, Schuller P, Bachmann B, Spitz S, Ertl P and Rothbauer M 2019 *Sci. Rep.* **9** 9287

Leichlé T, Lin Y-L, Chiang P-C, Hu S-M, Liao K-T and Chou C-F 2012 *Sens. Actuators* B **161** 805–10

Lepock J R, Frey H E and Ritchie K P 1993 *J. Cell Biol.* **122** 1267–76

Lindsay M, Bishop K, Sengupta S, Co M, Cumbie M, Chen C-H and Johnston M L 2018 *IEEE Trans. Biomed. Circuits Syst.* **12** 1046–55

Luan E, Shoman H, Ratner D M, Cheung K C and Chrostowski L 2018 *Sensors* **18** 3519

Madsen M H, Feidenhans'l N A, Hansen P-E, Garnæs J and Dirscherl K 2014 *J. Micromech. Microeng.* **24** 127002

Mercene Labs AB Datasheet Ostemer 322 Crystal Clear 2019 (available at: www.ostemers.com/wp-content/uploads/ 2019/10/Data-sheet-OSTEMER-322-Crystal-Clear-v6.pdf) (Accessed 16 November 2021)

Mielnik M M, Tofteberg T R and Andreassen E 2013 *17th Int. Conf. Miniaturized Systems for Chemistry and Life Sciences, MicroTAS 2013* vol **2** pp 796–8

Oevreeide I H, Zoellner A, Mielnik M M and Stokke B T 2021a *J. Micromech. Microeng.* **31** 015006

Oevreeide I H, Zoellner A and Stokke B T 2021b *Micromachines* **12** 556

OSTEMER 322 Crystal Clear n.d. (available at: www.ostemers.com/products/ostemer-crystal-clear/) (Accessed 16 November 2021)

OSTEMER 324 Flex n.d. (available at: www.ostemers.com/products/ostemer-flex/) (Accessed 1 December 2021)

Pardon G, Saharil F, Karlsson J M, Supekar O, Carlborg C F, van der Wijngaart W and Haraldsson T 2014 *Microfluid. Nanofluidics* **17** 773–9

Poghossian A and Schöning M J 2021 *Curr. Opin. Electrochem.* **29** 100811

Porterfield J Z and Zlotnick A 2010 *Virology* **407** 281–8

Rastogi R P, Richa K, Tyagi A and Sinha M B 2010 *J. Nucleic Acids* **2010** 592980

Ravanat J-L, Douki T and Cadet J 2001 *J. Photochem. Photobiol.* B **63** 88–102

Saharil F, Carlborg C F, Haraldsson T and van der Wijngaart W 2012 *Lab Chip* **12** 3032–5

Sandström N, Shafagh R Z, Vastesson A, Carlborg C F, van der Wijngaart W and Haraldsson T 2015 *J. Micromech. Microeng.* **25** 075002

Sticker D, Rothbauer M, Lechner S, Hehenberger M-T and Ertl P 2015 *Lab Chip* **15** 4542–54

Taklo M M V 2002 *Wafer Bonding for MEMS* (Norway: University of Oslo)

Valera E, Shia W W and Bailey R C 2016 *Clin. Biochem.* **49** 121–6

Volpatti L R and Yetisen A K 2014 *Trends Biotechnol.* **32** 347–50

Washburn A L, Gunn L C and Bailey R C 2009 *Anal. Chem.* **81** 9499–506

Washburn A L, Luchansky M S, Bowman A L and Bailey R C 2010 *Anal. Chem.* **82** 69–72

Watson J D and Crick F H C 1953 *Nature* **171** 737–8

Zhou X C, Sjöberg R, Druet A, Schwenk J M, van der Wijngaart W, Haraldsson T and Carlborg C F 2017 *Lab Chip* **17** 3672–81

6.4   PAPER IV

Sensitivity enhanced biophotonic sensor utilizing sub-wavelength gratings

TABLE 6.1.   Errata list from paper IV

Page/Line/Figure	Original text	Corrected text
Caption of the Figure 1	(a) MZI interferometer with SWGs	(a) MZI interferometer **without** SWGs
Caption of the Figure 2	(a) MZI interferometer with SWGs	(a) MZI interferometer **without** SWGs
Caption of the Figure 5	Fig. 4. Measured output power vs wavelength, (a) MZI interferometer with SWGs, (b) MZI with 3044 SWGs periods in the sensing arm, (c) MZI with 3044 SWGs periods in both arms.	Fig. **5**. Measured output power vs wavelength, (a) MZI interferometer **without** SWGs, (b) MZI with **100** SWGs periods in the sensing arm, (c) MZI with **100** SWGs periods in both arms.

PROCEEDINGS OF SPIE

Sensitivity enhanced biophotonic sensor utilizing sub-wavelength gratings

Mukesh Yadav, Jens Høvik, Dag Roar Hjelme, Astrid Aksnes

SPIE.

Sensitivity enhanced biophotonic sensor utilizing sub-wavelength gratings

Mukesh Yadav, Jens Høvik, Dag Roar Hjelme and Astrid Aksnes

Department of Electronic systems, NTNU, Trondheim, Norway

mukesh.yadav@ntnu.no

ABSTRACT

We present a sensor design based on a Mach-Zehnder interferometer utilizing sub-wavelength gratings (SWGs) that were included in the waveguide to compensate for the short optical path length and to provide phase modulation. According to 2D finite element method simulations, it is possible to achieve 3-fold enhancement in sensitivity and 50% increase in modulation frequency with the inclusion of SWGs in the sensing arm as well as in the reference arm.

Keywords: Optical waveguide sensor, biosensor, Mach-Zehnder interferometer, sub-wavelength gratings, silicon-on-insulator, waveguide, phase modulation, lab-on-a-chip

1. INTRODUCTION

In recent years, there is growing interest in the development of integrated sensors for chemical and biomedical applications. These sensors are commonly referred to as lab-on-a-chip devices [1]. For many applications in the biomedical field, sensors are required with high sensitivity, selectivity, compactness, and low cost. Optical waveguide sensors have high potential to fulfill all these requirements. Optical waveguide sensors provide several advantages over other sensor technologies such as being label-free and free from electromagnetic interference. The aim of our work is to develop an all-optical waveguide lab-on-a-chip biosensor with these properties. Our optical waveguide design utilizes sub-wavelength gratings to increase the analyte-light interaction [8][9]. This higher interaction of light with outer media is advantageous for higher phase control and sensitivity. In order to design the sensor with the desired properties, 2D finite element method (FEM) simulations were performed by using COMSOL Multiphysics 5.2a.

2. THEORY

The Mach-Zehnder interferometer (MZI) sensor is one of the most common optical waveguide sensor designs due to its simple layout and high sensitivity [2][4][5][6][7]. Optical waveguide MZI sensors use the interference between two single mode waveguides. An input single mode waveguide is divided into two single mode waveguides utilising a Y-junction and then recombining into a single mode output waveguide. One arm is used as a reference and the other for sensing. The reference arm is impermeable to the target analyte and the sensing arm is cladded with a layer sensitive to the target analyte. The effective refractive index change in the sensing arm due to the target analyte results in the phase change. The output intensity of the Mach-Zehnder interferometer is periodic with respect to phase difference between the guided modes travelling in both arms and is given by:

$$I_T = I_S + I_R + 2\sqrt{I_S I_R}\cos[\Delta\varphi_S(t)] \tag{1}$$

The phase difference depends on the arm length and difference in effective refractive index of the guided mode in both arms,

$$\Delta\varphi_S(t) = 2\pi\frac{L}{\lambda}(N_S(t) - N_R) \tag{2}$$

where $\Delta\varphi_S(t)$ is the phase difference between the beam propagating in the two arms, λ is the coupled wavelength, L is the interaction length, N_R and $N_S(t)$ are the effective refractive indices of the guided mode in the reference arm and the sensing arm, respectively.

The periodic nature of the interferometer output has limitations of phase ambiguity, sensitivity fading and intensity fluctuations, which leads to false results, and lower limit of detection [2]. To avoid ambiguous output, a phase modulation technique is commonly utilized. It requires a modulation signal with higher frequency than the sensor response. At present, most phase modulated interferometer sensors are realised by utilising electro-optical modulators [2][10]. An electro-optical modulator requires electrodes and an electrical circuit, which makes fabrication more complex. It also creates hinderance in integration of the sensor with the microfluidics [3]. The all-optical phase modulation technique is advantageous over an electro-modulator. Electrodes and electrical circuits are not required in an all-optical technique which simplifies fabrication and allows miniaturization. It utilizes a tunable laser to induce the wavelength dependent phase modulation in a given interferometer [3].

The wavelength dependent phase modulation is given as:

$$\delta(\Delta\varphi_S) = \frac{2\pi}{\lambda}\left[-\frac{1}{\lambda}(N_S - N_R) + \frac{\partial(N_S - N_R)}{\partial\lambda}\right]L\delta\lambda \tag{3}$$

From equations (2) and (3), the sensor response and phase modulated signal are directly proportional to the interaction length and the difference between the guided mode indices of the two arms.

3. SIMULATION

3.1 Sensor design

A Mach-Zehnder interferometer sensor was designed using silicon waveguides supporting single TE-modes. The reference and sensing arm of the interferometer were 761 µm and the bend radius of the Y-junction was 140 µm. The interferometer reference arm was cladded with 1 µm wide SU8 polymer and the sensing arm with air. Subwavelength gratings with 250 nm period and 60% duty cycle were included in the interferometer arms to increase the light-analyte interaction, rather than increasing the pathlength of the arms.

3.2 Simulated results

2D Finite element method (FEM) simulations using COMSOL were performed on the designed Mach-Zehnder interferometer to estimate the sensitivity, and modulation frequency with the inclusion of subwavelength gratings (SWGs) in the arms of a conventional Mach-Zehnder interferometer sensor.

To estimate the sensitivity improvement due to inclusion of subwavelength gratings, we performed simulations on conventional Mach-Zehnder interferometers with SWGs in the sensing arm and in both arms. To estimate the sensitivity, the refractive index of the reference arm cladding was kept constant at 1.57 (SU8) while the refractive index of the sensing arm cladding was tuned from 1.33 to 1.38. The output intensity of the interferometer is plotted against the change in the refractive index of the sensing arm cladding, as shown in Fig.1.
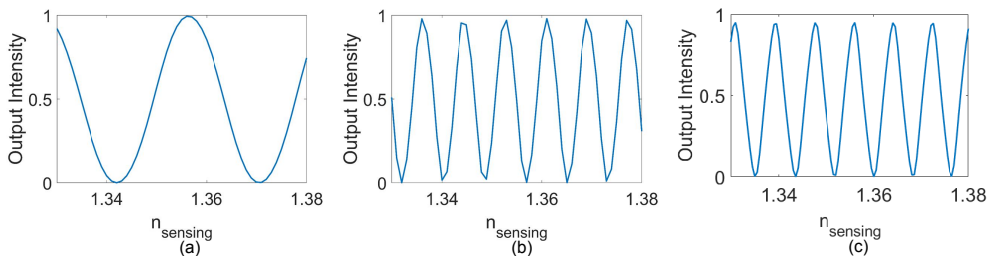
Fig. 1. FEM simulation of output intensity vs sensing arm cladding refractive index for 1550 nm (λ), (a) MZI interferometer with SWGs, (b) MZI with 3044 SWGs periods in the sensing arm, (c) MZI with 3044 SWGs periods in both arms.

To study the all-optical phase modulation, the estimation of output intensity with respect to change in the input wavelength was performed. Simulations were performed for interferometer designs without SWGs, with 3044 periods of

SWGs in the sensing arm and with 3044 periods of SWGs in both arms. The reference arm was cladded with SU8 and the sensing arm with air. The results are shown in Fig.2.

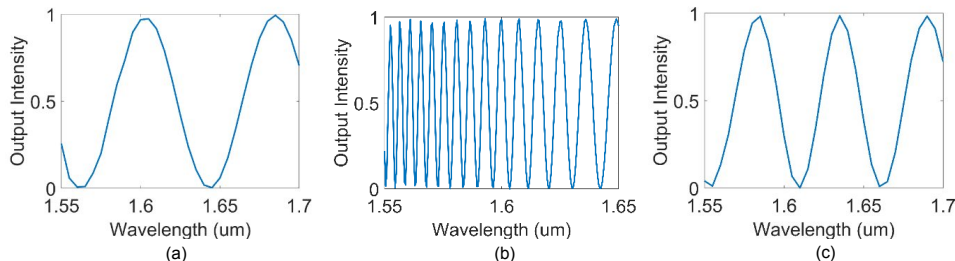
Fig. 2. FEM simulation of output intensity vs wavelength, (a) MZI interferometer with SWGs, (b) MZI with 3044 SWGs periods in the sensing arm, (c) MZI with 3044 SWGs periods in both arms.

As shown in Fig.1, a 3-fold enhancement in bulk sensitivity is estimated with the inclusion of SWGs gratings in the sensing arm. The sensitivity of the interferometer with SWGs in both arms is also increased by 3-folds in comparison to the conventional MZI. A low frequency sinusoidal modulated signal is observed for the conventional MZI. A high frequency modulation signal is observed when SWGs are introduced in sensing arm, but the frequency is not uniform over the wavelength range, chirping is seen. On the other hand, the MZI with SWGs in both arms has 50 % higher modulation frequency than the conventional MZI and is uniform over the wavelength range.

To understand the effect of SWGs only in the sensing arm, we performed MIT photonic band gap (MPB) simulations. MPB is used to find the frequency eigenstates for arbitrary propagation constants by solving Maxwell's equations. MPB simulations were performed on silicon core SWGs and strip waveguides with different claddings. The resulting dispersion relation is shown in Fig.3.
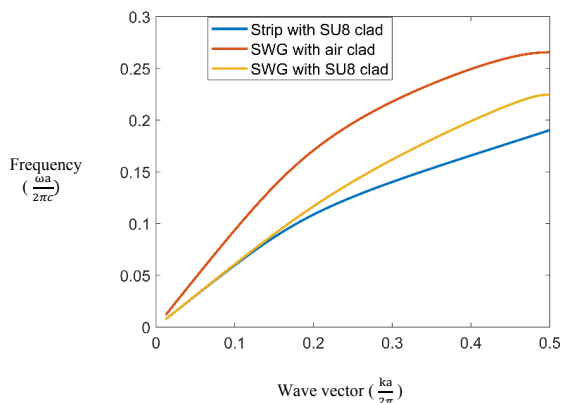
Fig. 3. MPB simulation of frequency vs wave vector for lattice constant (a) of 250 nm

where, f is the frequency, k is the propagation constant, c is the speed of light and a is the lattice constant.

As shown in Fig.3, SWGs have higher dispersion than strip waveguides. This indicates a higher sensitivity to change in the effective refractive index with respect to wavelength. The slope difference between the strip and SWGs result in non-uniform modulated signals (chirping) as shown in Fig.2 (b). It is further understood from equation 3, where the second term becomes negligible for the interferometer with the strip waveguide and results in a uniform sinusoidal signal. On

the other hand, it becomes non-negligible for the sensor with a strip waveguide in one arm and SWGs in the other arm, which results in a signal with non-uniform frequency over a wavelength range (chirping).

4. FABRICATION

To investigate the modulation, and sensitivity for different designs, strip waveguide based Mach-Zehnder interferometers were fabricated on a silicon-on-insulator platform. For comparison, Mach-Zehnder interferometers with 4mm arm length were fabricated without SWGs, with 100 periods of SWGs in the sensing arm, and with 100 periods of SWGs in both arms. Strip waveguides were used as they provide large surface area for evanescent fields. To satisfy single TE mode condition for the wavelength of 1550 nm, strip waveguides were fabricated with dimension of 220 nm height and 500 nm width. SWGs were fabricated with 250 nm period and duty cycle of 60% as shown in Fig.4 (b).

Amorphous silicon of 220 nm thickness was deposited on 1 µm thick layer of thermal oxide on silicon substrate. Amorphous silicon deposition is done using plasma-enhanced chemical vapor deposition (PECVD). Silicon strip waveguide based MZIs were fabricated by utilising electron beam lithography process. For electron beam lithography, 200 nm thin layer of CSAR62 was spin coated on an SOI chip and baked at 150 degrees for 1 minute. Baked electron beam resist was then exposed with Elionix ELS-G100 system to generate the waveguide pattern, with a beam current of 500pA . After exposure, the chip was developed in AR 600-546 for 1 minute, which was followed by 1-minute oxygen plasma. Inductively coupled plasma reactive ion etching (ICP-RIE) chiller was used to etch the amorphous silicon layer through the resist mask to generate the sensor design. After etching, the sample was cleaned using AR 600-71 to remove residual resist.
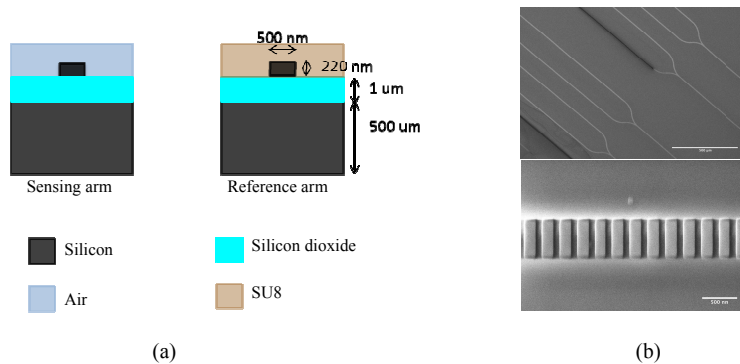
Fig. 4. (a) Schematic of waveguide dimensions, (b) SEM image of fabricated interferometer and SWGs

5. EXPERIMENTAL RESULTS

Preliminary modulation measurements of the fabricated strip waveguide based Mach-Zehnder interferometer were studied. For measurements, an infrared tunable laser source and infrared detector were used. In Fig.5, measurement results of output power with respect to wavelength tuning are shown for three different interferometer designs. In Fig.5a, the modulation signal is shown for the interferometer design having 4 mm arm length, a SU8 cladded reference arm, an uncladded sensing arm and no SWGs. A wavelength shift of 2.3 nm results in a 2π phase shift. In Fig.5b and c, modulation measurements are shown for the interferometer with inclusion of 100 periods of SWGs in the sensing arm and in both arms, respectively. The modulation frequency for the three designs was found to be the same. In the simulations, the modulation frequency for the interferometer with SWGs in the sensing arm decreases with wavelength , while for the fabricated interferometer non-uniformity is not observed. The main reason for this discrepancy is that in the simulations, the sensing arm is completely replaced with SWGs but in the fabricated one, SWGs replaced less than 1% of the sensing arm. Therefore, the effective refractive index due to the strip waveguide is dominant over the SWGs and results in the same response as for the strip waveguide. High transmission was observed through the fabricated strip waveguides, and also through the strip waveguides with SWGs.

Fig. 4. Measured output power vs wavelength, (a) MZI interferometer with SWGs, (b) MZI with 3044 SWGs periods in the sensing arm, (c) MZI with 3044 SWGs periods in both arms.

6. CONCLUSION

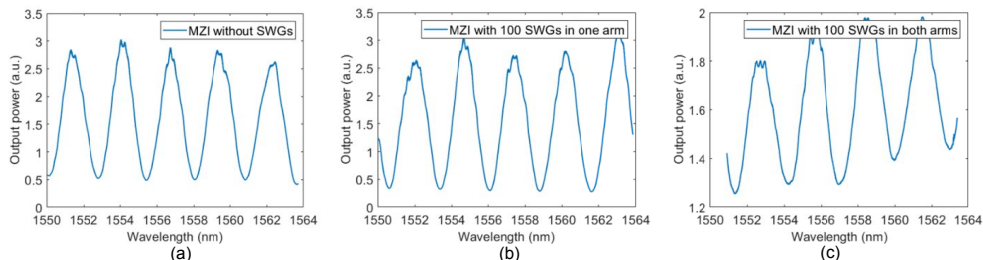The simulation results indicate a 3-fold increase in bulk sensitivity and 50 % increase in wavelength dependent modulation frequency of a Mach-Zehnder interferometer with the inclusion of SWGs in both arms. Low-loss waveguides with SWGs were fabricated. Preliminary measurements show promising results. Fabrication of Mach-Zehnder interferometer with SWGs in both arms can be used to compensate for short optical path length and reduce the effect of phase ambiguity.

Acknowledgements

REFERENCES

1. Estevez, M. Carmen, Mar Alvarez, and Laura M. Lechuga. "Integrated optical devices for lab-on-a-chip biosensing applications." *Laser & Photonics Reviews* 6(4), 463-487 (2012).
2. G. Heideman and P. V. Lambeck, "Remote opto-chemical sensing with extreme sensitivity: design, fabrication and performance of a pigtailed integrated optical phase-modulated Mach–Zehnder interferometer system," Sens. Actuators B Chem. **61**(1-3), 100–127 (1999).
3. Dante, Stefania, et al. "All-optical phase modulation for integrated interferometric biosensors." *Optics express* 20(7), 7195-7205 (2012).
4. Dullo, Firehun Tsige, et al. "Sensitive on-chip methane detection with a cryptophane-A cladded Mach-Zehnder interferometer." *Optics express* 23(24), 31564-31573 (2015).
5. Prieto, Francisco, et al. "An integrated optical interferometric nanodevice based on silicon technology for biosensor applications." *Nanotechnology* 14(8), 907 (2003).
6. Yuan, Dengpeng, et al. "Mach-zehnder interferometer biochemical sensor based on silicon-on-insulator rib waveguide with large cross section." *Sensors* 15(9), 21500-21517 (2015).
7. Heideman, R. G., R. P. H. Kooyman, and Jan Greve. "Performance of a highly sensitive optical waveguide Mach-Zehnder interferometer immunosensor." *Sensors and Actuators B: Chemical* 10(3), 209-217 (1993).
8. Wangüemert-Pérez, J. Gonzalo, et al. "Evanescent field waveguide sensing with subwavelength grating structures in silicon-on-insulator." *Optics letters* 39(15), 4442-4445 (2014).
9. Donzella, Valentina, et al. "Sub-wavelength grating components for integrated optics applications on SOI chips." *Optics express* 22(17), 21037-21050 (2014).
10. Preston, Kyle, et al. "Deposited silicon high-speed integrated electro-optic modulator." *Optics express* 17(7), 5118-5124 (2009).

APPENDIX A

Patent application on the MARC sensor

A.1 OPTICAL SENSING APPARATUS

US 20230134264A1

(54) **OPTICAL SENSING APPARATUS**

(71) Applicant: **NORWEGIAN UNIVERSITY OF SCIENCE AND TECHNOLOGY (NTNU)**, Trondheim (NO)

(72) Inventors: **Mukesh YADAV**, Trondheim (NO); **Astrid AKSNES**, Trondheim (NO); **Dag Roar HJELME**, Trondheim (NO); **Jens HØVIK**, Trondheim (NO)

(73) Assignee: **NORWEGIAN UNIVERSITY OF SCIENCE AND TECHNOLOGY (NTNU)**, Trondheim (NO)

(57) **ABSTRACT**

An optical sensing apparatus is provided comprising: an input interface for receiving input light into the optical sensing apparatus; an input waveguide and a reference waveguide, both arranged to receive input light from the input interface; a closed loop resonator, wherein the input waveguide is optically coupled to the closed loop resonator at an input point for introducing input light to the closed loop resonator; a sample region, adjacent the closed loop resonator, for receiving a sample such that evanescent coupling can occur between light in the closed loop resonator and the sample; a drop-port waveguide, optically coupled to the closed loop resonator at a drop point for receiving dropped light from the closed loop resonator; an output waveguide; and an output interface. The reference waveguide and the drop-port waveguide are arranged to direct interfering light through the output waveguide to produce an output signal at the output interface.

FIG. 1

FIG. 2

FIG. 3

FIG. 4

FIG. 5

FIG. 6

FIG. 7

Workstation/ computer

208

204

Photodetector

Single mode fiber

2

Photonic chip

Single mode fiber

200

202

206

Tunable laser

Polarization paddles
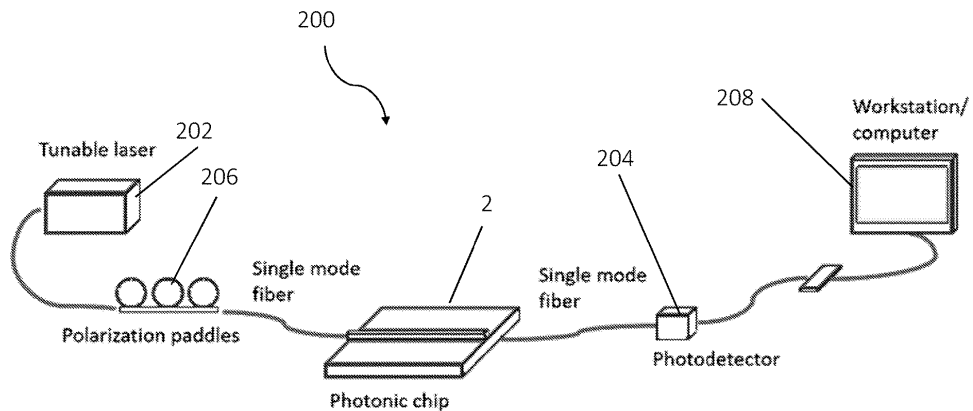
FIG. 8

FIG. 9

FIG. 10

OPTICAL SENSING APPARATUS

BACKGROUND OF THE INVENTION

[0001]   The present invention relates to a system and apparatus for optical sensing, e.g. for use in bio-sensing.

[0002]   Closed loop or ring resonators are formed from a waveguide that is looped back on itself, such as a circular waveguide. They have a spectral response that is characterised by resonances at wavelengths that are submultiples of the optical path length of the closed loop resonator. Typically, light (e.g. from a laser) is introduced into a ring resonator via evanescent coupling from an adjacent waveguide. The spectral response of the ring resonator may be observed by measuring the intensity of light that couples out of the resonator into a "drop-port" waveguide that is also located adjacent the ring resonator. Alternatively, it may be inferred from the intensity of the light in the input waveguide that does not couple into the resonator (referred to as the "through-port" transmission).

[0003]   The resonances of the ring resonator can be detected by sweeping the wavelength of monochromatic input light and monitoring the intensity of light at the through port or drop port. At resonant wavelengths, the through-port response dips in intensity (where power is diverted to the ring resonator), and the drop-port response peaks in intensity.

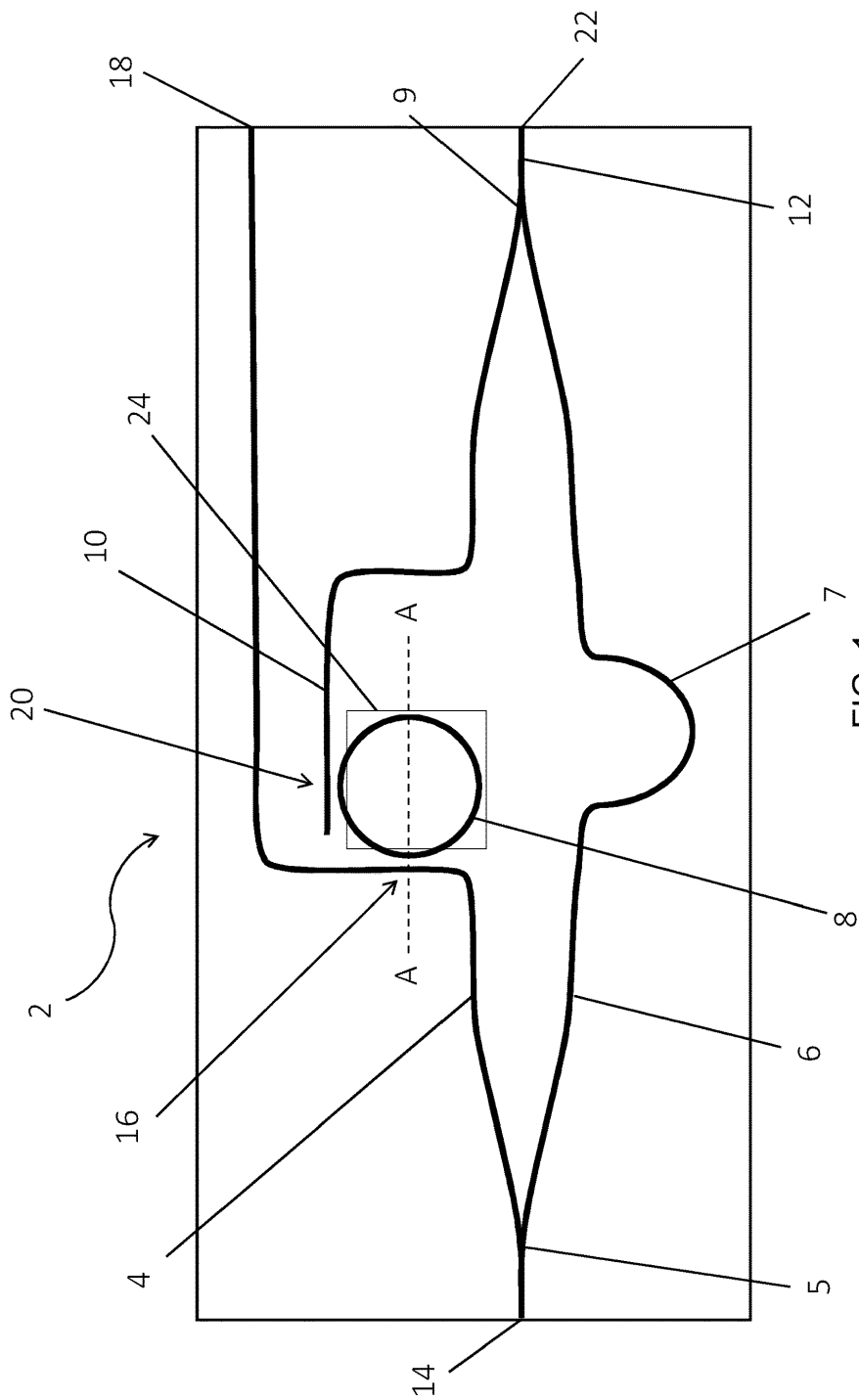[0004]   In a ring resonator, the repetition period of the pattern of resonant peaks at the drop port, or of dips at the through port, (which is also referred to as the free spectral range of the resonator) is determined largely by the size of the ring resonator. In general, as the optical path length of the resonator increases (e.g. as the diameter of a circular ring resonator increases), the wavelength spacing between resonances reduces.

[0005]   It is known to utilise ring resonators to measure properties of samples (e.g. liquid or gaseous biological samples). A sample having a property to be sensed is placed in or adjacent to the optical path of the ring resonator, thereby adjusting the refractive index, and hence the optical path length, of the ring resonator. For example, a chemical sensing layer may be immobilised on a surface of the ring resonator, which may bind a target analyte in the sample within the evanescent field of light in the resonator. The change in optical path length shifts the wavelengths at which resonance peaks occur. The magnitude of the wavelength shift can be measured to determine one or more properties of the sample, such as the concentration of a target analyte in the sample.

[0006]   However, if the magnitude of the wavelength shift in resonance peaks is comparable to the free spectral range of the ring resonator-based sensor, it becomes difficult or impossible to determine, without ambiguity, the direction and/or the magnitude of the shift. For example, a spectrum in which the peaks have been shifted the equivalent of 90% of a peak separation in one direction would appear to be essentially identical to a spectrum in which the peaks have shifted 10% of the peak separation in the other direction. Similarly, a spectrum that is shifted by 110% of the peak separation may be indistinguishable to a spectrum shifted by 10% of the peak separation.

[0007]   It may be possible to reduce some of these ambiguities using knowledge of an appropriate expected magnitude of shift, but this may not always be possible (e.g. for an entirely uncharacterised sample).

[0008]   Another approach is to decrease the size of the ring resonator so as to increase the spacing between resonance peaks and thus increase the dynamic range of the resonator. However, reducing the size of the ring resonator leads to a corresponding decrease in the Q-factor of the resonator (i.e. peaks that are less sharply defined) and thus to a lower sensitivity.

[0009]   An improved approach is therefore desired.

SUMMARY OF THE INVENTION

[0010]   According to a first aspect of the present invention there is provided an optical sensing apparatus comprising:

[0011]   an input interface for receiving input light into the optical sensing apparatus;

[0012]   an input waveguide and a reference waveguide, both arranged to receive input light from the input interface;

[0013]   a closed loop resonator, wherein the input waveguide is optically coupled to the closed loop resonator at an input point for introducing input light to the closed loop resonator;

[0014]   a sample region, adjacent the closed loop resonator, for receiving a sample such that evanescent coupling can occur between light in the closed loop resonator and the sample;

[0015]   a drop-port waveguide, optically coupled to the closed loop resonator at a drop point for receiving dropped light from the closed loop resonator;

[0016]   an output waveguide; and

[0017]   an output interface,

wherein the reference waveguide and the drop-port waveguide are arranged to direct interfering light through the output waveguide to produce an output signal at the output interface.
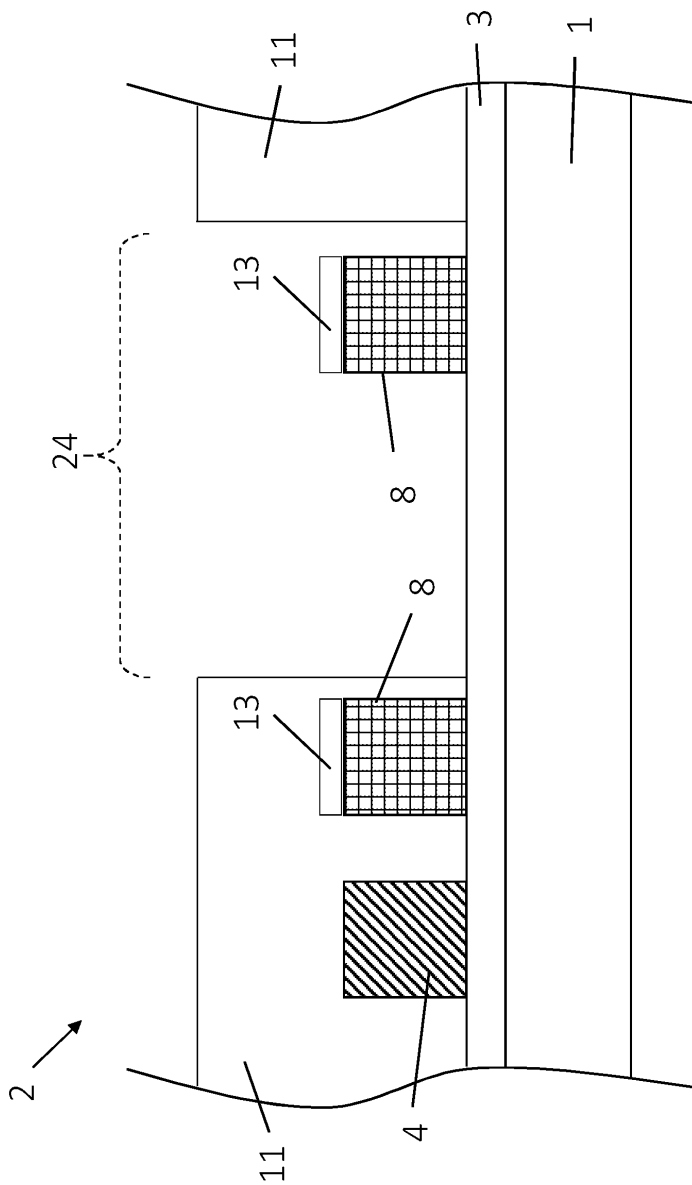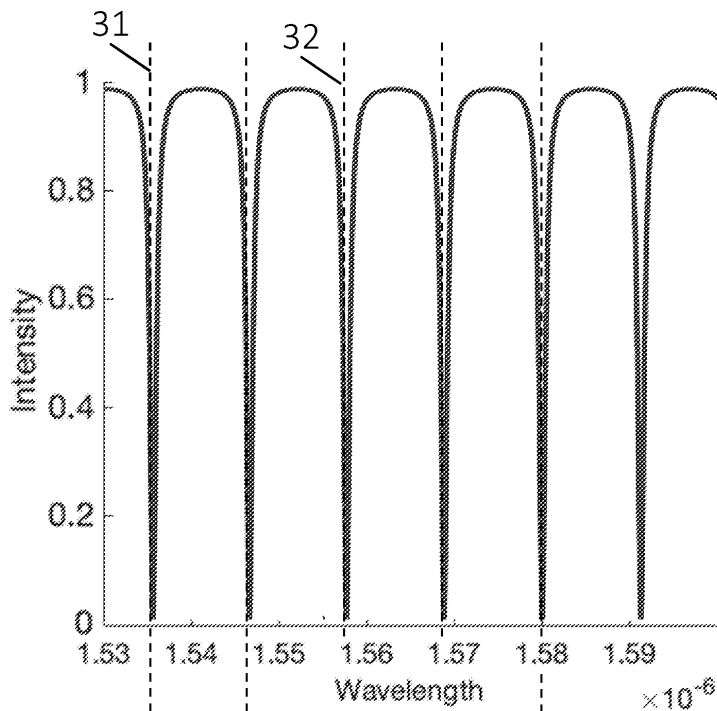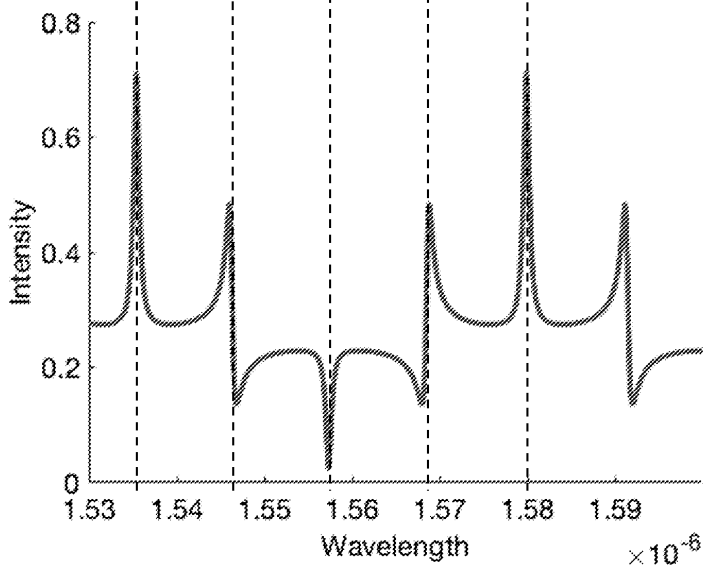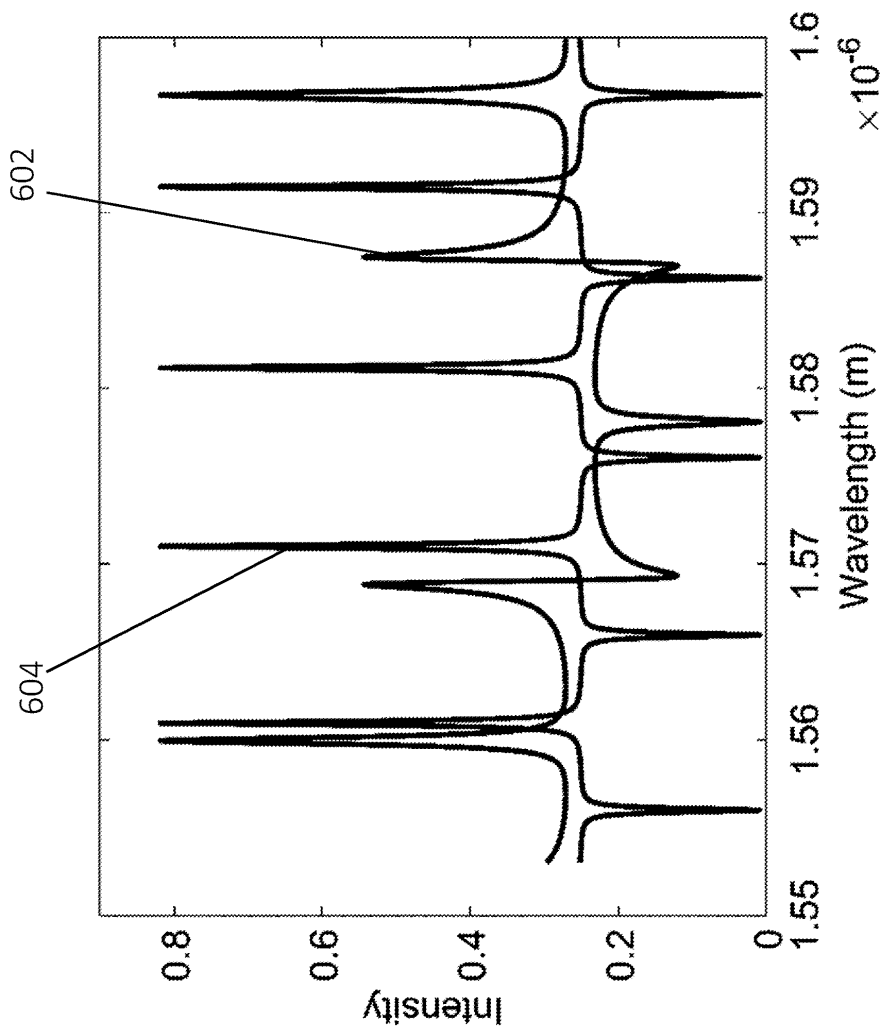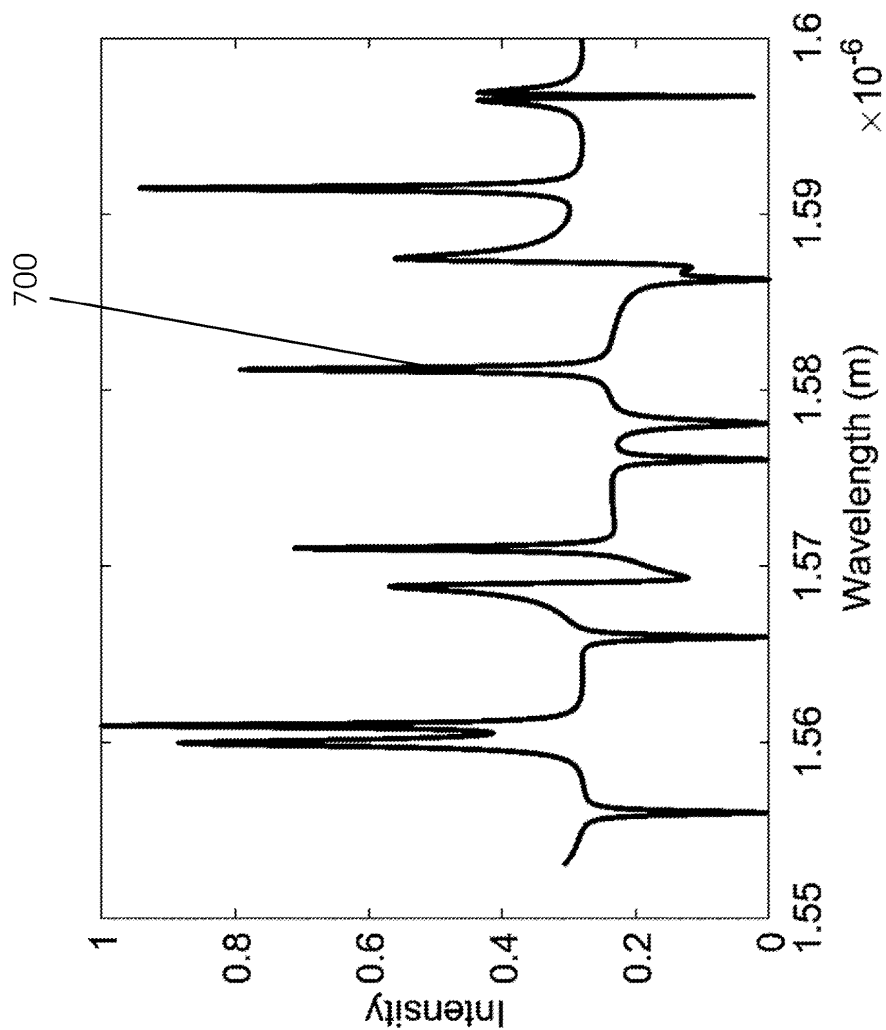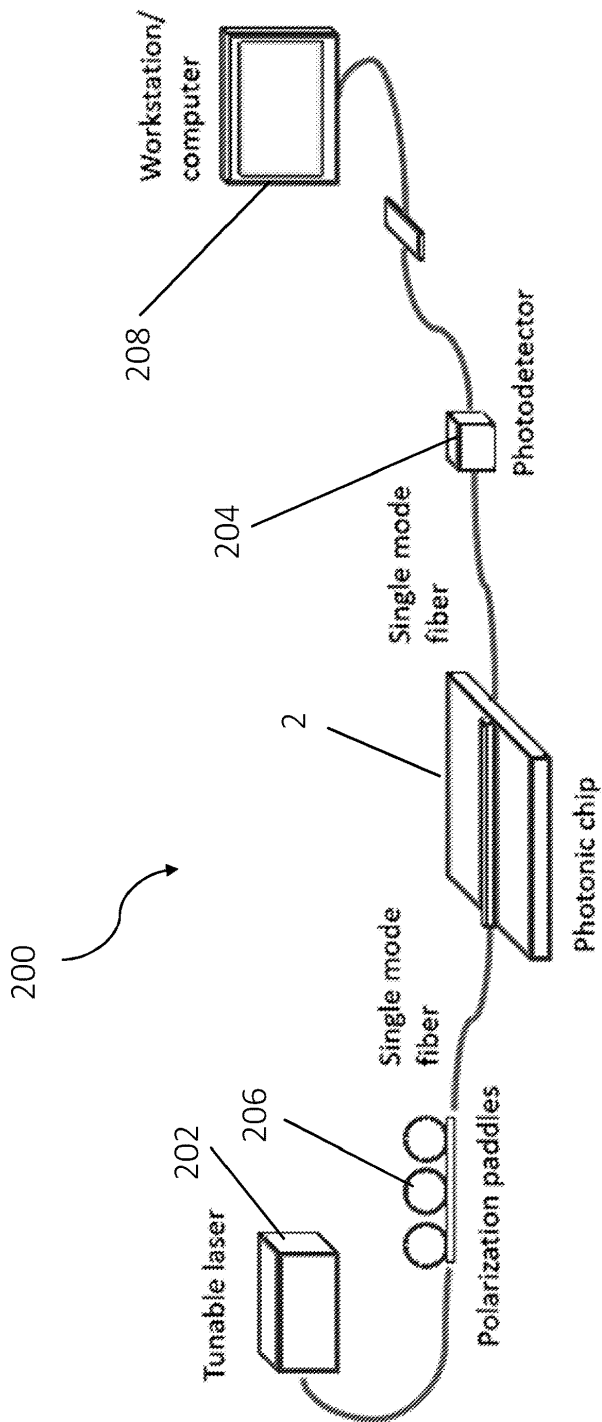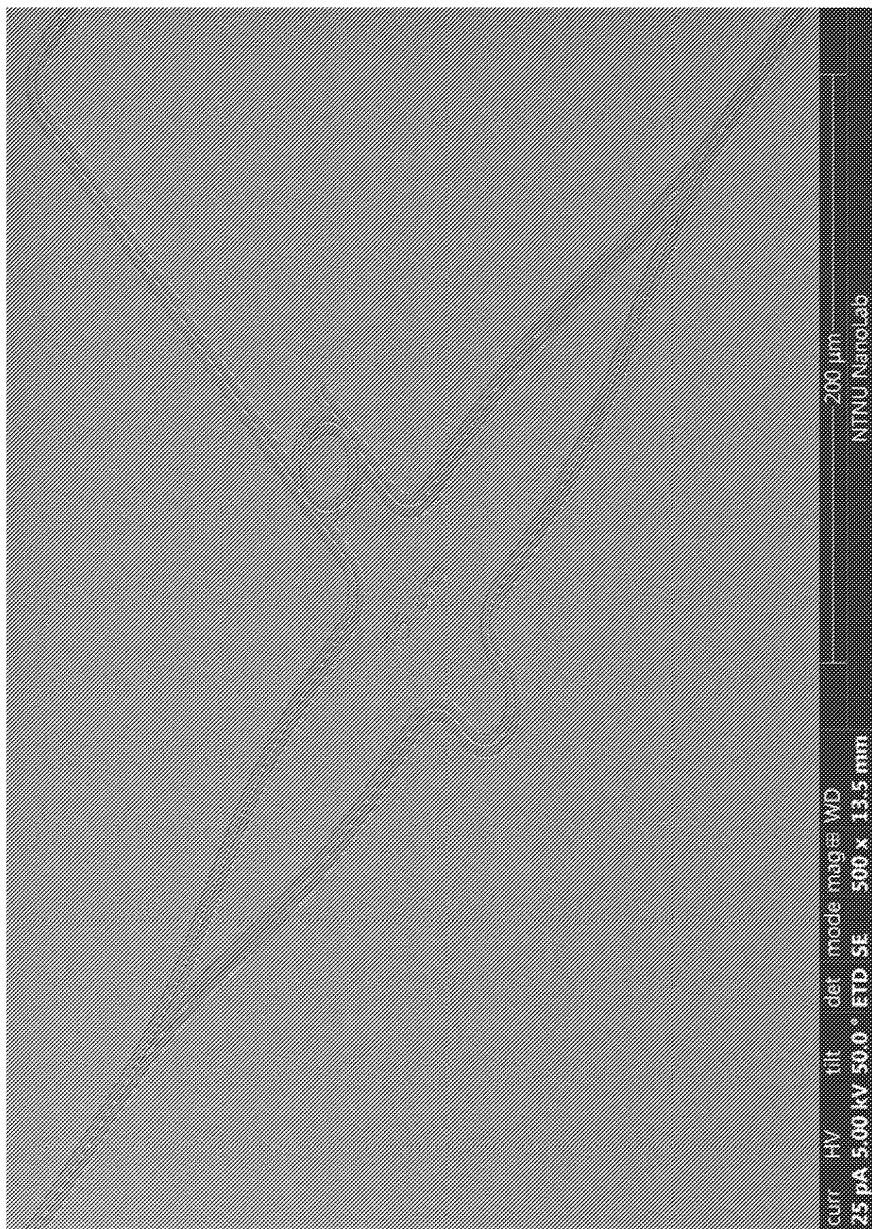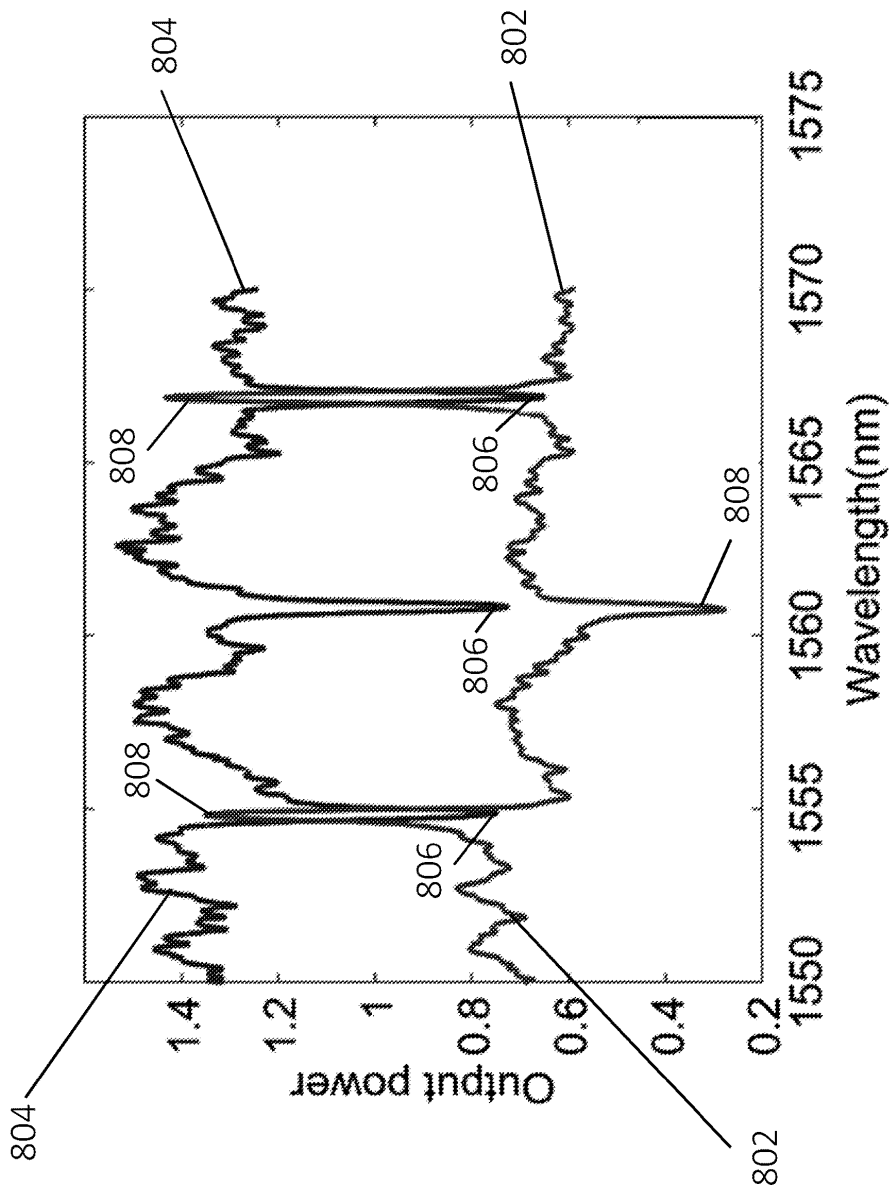
[0018]   Thus, it will be understood that the apparatus uses interference between light in a reference waveguide and light that is dropped from the closed loop resonator to generate an output signal. The output signal may have a spectral response to the input light that comprises a periodic pattern of resonance peaks that depends at least partially on a property of a sample in the sample region. The use of interference, in combination with resonance, for sensing a sample means that the pattern of peaks in the output signal may have two or more times the period of an equivalent conventional ring resonator-based sensor. In this way, the dynamic range of the whole optical sensing apparatus may be two or more times that of the closed loop resonator. This is because a wavelength-dependent phase offset is established between the dropped light in the drop-port waveguide and the input light in the reference waveguide, such that adjacent resonant peaks in the output signal have different intensities and/or spectral shapes, rather than all having substantially the same intensity as with a conventional ring resonator.

[0019]   For a conventional optical ring resonator, the free spectral range limits the dynamic range for the sensor. However, in some embodiments of the present invention, the dynamic range may merely be proportional to the free spectral range. It is therefore possible, in some embodiments, to measure, without ambiguity, a larger shift in the resonance peaks, when a sample is introduced to the sample region, without needing to reduce the size of the resonator to increase the spacing between resonance peaks. The optical sensing apparatus may thus have a larger closed loop

resonator (i.e. one with a longer optical path length) and still achieve a desired dynamic range , thereby increasing the Q-factor of the resonator and improving the sensitivity of measurements compared with using a resonator on its own. Furthermore, a shift in the pattern of resonant peaks may be identified with an observation of only part of the pattern (i.e. over a limited range of wavelengths that may not cover the whole pattern repetition unit). This may reduce the range of input light wavelengths required to establish the magnitude of a shift without ambiguity, which can reduce the required wavelength range, and thus cost and complexity, of a light source (e.g. tunable laser) for use with the apparatus.

[0020] The pattern of resonant peaks is achieved by interfering dropped light from the closed loop resonator with input light carried by the reference waveguide. Because the light is introduced to the closed loop resonator by the input waveguide at an input point, and dropped light is received from the closed loop resonator by the drop-port waveguide at a different drop point, there will be a phase offset between the input light in the reference waveguide and the dropped light in the drop-port waveguide, when the input light and dropped light interfere, that depends on the wavelength of the input light. Therefore, at different resonances of the closed loop resonator (i.e. at wavelengths of the input light which are submultiples of the optical path length of the closed-loop resonator) the phase offset between the input light in the reference waveguide and the dropped light in the drop-port waveguide will change. The dropped light in the drop-port waveguide will thus interfere differently with the input light in the reference waveguide at different resonance peaks, producing a pattern of resonance peaks in the output signal with different intensities.

[0021] The pattern of resonance peaks has a period that depends at least partially on the configuration of the input waveguide, closed loop resonator and the drop-port waveguide. The separation between the input point and the drop point can introduce a wavelength-dependent phase difference between the input light at the input point and the dropped light at the drop point. In some sets of embodiments, the input point and the drop point are separated by half the path length of the closed loop resonator. In such embodiments the dropped light at the drop point and the input light at the input point will be phase offset by π when the optical path length around the whole closed loop resonator is equal to an odd number of wavelengths of the input light, and will be in phase when the optical path length around the whole closed loop resonator is equal to an even number of wavelengths of the input light. This leads to a pattern of resonance peaks in the output signal with a period of two resonance peaks. This may be double the dynamic range of a same-sized conventional ring resonator-based sensor.

[0022] However, the dynamic range of the apparatus (corresponding to the period of the repeating pattern of peaks in the output signal) may advantageously be further increased by adjusting the separation of the input point and the drop point away from half the path length. Thus, in some sets of embodiments, the input point and the drop points are separated by less than half the optical path length of the closed loop resonator. (Of course, because the resonator is a loop, these points can also be seen as being separated by more than half the optical path length, when measured around the longer arc of the loop.) This results in the pattern of resonance peaks having period of three or more resonance

peaks (i.e. at least three times the free spectral range of a conventional ring resonator sensor). For example, the input point and the drop point may be separated by less than **45%** of the optical path length of the closed loop resonator. In some sets of embodiments the closed loop resonator is convex (e.g. circular) and the input point and the drop point have an angular separation around the closed loop of less than 180° and preferably less than 160°.

[0023] Preferably, the input point and the drop point are separated by an optical path length that is a submultiple (i.e. a unit fraction) of the optical path length of the closed loop resonator, such as a third, a quarter, a fifth, a sixth, a seventh or an eighth of the optical path length of the closed loop resonator. Such configurations can help to produce clear patterns of resonance peak intensities. For example, for a convex closed loop resonator (e.g. a circular resonator) preferably the input point and the drop point are separated by an angle of approximately 45°, 60°, 90°, or 120°. More generally, in some embodiments, the input point and the drop point may be separated by an optical path length that is a common fraction of the optical path length of the closed loop resonator, such as three-eighths of the optical path length of the closed loop resonator. For example, for a convex closed loop resonator (e.g. a circular resonator) the input point and the drop point may be separated by an angle of approximately 135°.

[0024] It will be appreciated that the optical path length of the closed loop resonator will change when a suitable sample is introduced to the sample region. For some embodiments, the optical path length around the closed loop resonator may refer to the path length when no sample is present. However, in some embodiments, so long as the sample affects the resonator fairly uniformly around the length of the resonator, the separation distance between the input and drop points will scale substantially in proportion with the optical path length, so the same path length proportions can be preserved, whether a sample is present or not. In some embodiments, the sample region may not extend entirely uniformly over the closed loop resonator; for example, the sample region may exclude areas located at or adjacent the input and/or drop points of the resonator, to prevent undesirable interaction by the sample with the evanescent field of light in the input and/or drop port waveguides.

[0025] The input waveguide may be optically coupled to the closed loop resonator by being physically connected (i.e. such that light in the input waveguide is simply directed into the closed loop resonator). However, in some embodiments the input waveguide may be coupled to the closed loop resonator by evanescent coupling, where the input waveguide and the closed loop resonator are physically separate but are brought sufficiently close together that the evanescent field of light in the input waveguide extends into the closed loop resonator so as to couple light into the closed loop resonator.

[0026] As mentioned above, embodiments of the invention enable a closed loop resonator with an increased optical path length to be used without sacrificing dynamic range.

[0027] In some embodiments, the closed loop resonator comprises an optical path length of at least 100 µm, 200 µm, 300 µm, 500 µm, 600 µm, 700 µm, or even 800 µm or more. For example, the closed loop resonator may comprise a circular waveguide with a diameter of approximately 100 µm or more.

[0028] In some embodiments of the invention, the optical sensing apparatus further comprises a through-port waveguide arranged receive light from the input waveguide that does not couple into the closed-loop resonator. It may be arranged to produce a through-port output signal at a through-port output interface. The spectrum of the through-port output signal will comprise dips corresponding to resonances of the closed loop resonator (where power is diverted from the input waveguide into the closed loop resonator). Whilst the spectrum of the through-port output signal may not have the increased free spectral range of the pattern observed at the output interface, it may still be useful for refining the position of individual peaks identified in the interference output signal.

[0029] The through-port waveguide may simply be a continuation of the input waveguide after it has optically coupled to the closed loop resonator, although it could alternatively comprise a separate waveguide that is optically coupled to the input waveguide.

[0030] As explained above, at some resonances the input light in the reference waveguide will be offset in phase relative to dropped light in the drop-port waveguide, at a point at which the input light and dropped light interfere, with the amount of phase offset determined by the wavelength of the input light, and by the configurations of the closed-loop resonator, the input waveguide and the drop-port waveguide. Whilst any measureable difference in the intensities and/or spectral shapes of resonant peaks may be sufficient to increase the dynamic range of the resonator, it may be desirable to maximise the difference in intensities of resonant peaks in the output signal. It may also be desirable to optimise the performance of the optical sensing apparatus for input light with a wide range of wavelengths.

[0031] In some sets of embodiments, therefore, the total optical path length from the input interface to the output interface through the reference waveguide is equal to: the optical path length from the input interface to the input point of the closed loop resonator, plus the optical path length from the drop point of the closed loop resonator to the output interface. In such embodiments, the optical sensing apparatus is "balanced" in that the input light and dropped light interfering in the output waveguide have travelled respective distances that differ by an integer number of wavelengths, for all resonant wavelengths, except for a further constant phase difference due to the non-zero separation of the input and drop points of the closed loop resonator. The only phase offset between the input light and the dropped light will therefore be the constant phase offset introduced by the closed loop resonator, regardless of the wavelength of the input light (since there is no dropped light when the input light is not at a resonant wavelength). Furthermore, if there are resonances where no phase offset is introduced by the closed loop resonator (e.g. for wavelengths that are submultiples of the separation distance between the input and drop points in embodiments in which the path length of the closed loop resonator is an integer multiple of the separation distance between the input and drop points), the dropped light and input light will interfere constructively to produce a maximum intensity peak.

[0032] In some embodiments the reference waveguide branches from the input waveguide at a branch point within the optical sensing component and merges with the drop-port waveguide at a merge point within the optical sensing component. The reference waveguide may have an optical path length between the branch point and the merge point that is equal to an optical path length of the input waveguide between the branch point and the input point plus an optical path length of the drop-port waveguide between the drop point and the merge point.

[0033] More generally, the apparatus may comprise an optical splitter (e.g. a Y-branch splitter) comprising an input optically coupled to the input interface, a first output optically coupled to the reference waveguide, and a second output optically coupled to the input waveguide. It may comprise an optical combiner (e.g. a Y-branch combiner) comprising a first input optically coupled to the reference waveguide, a second input optically coupled to the drop-port waveguide, and an output optically coupled to the output waveguide.

[0034] As explained above, the presence of a sample in the sample region may cause the resonance peaks in the output signal to shift from their position when no sample is held in the sample region, or when a control substance, such as an aqueous buffer solution, is held in the sample region. The magnitude of the shift may be indicative of one or more properties of the sample, such as the concentration of a target analyte in the sample, or of a refractive index of the sample.

[0035] However, the Applicant has recognised that the resonance peaks may also shift for other reasons, causing errors in measurements. For example, a change in the ambient temperature may cause the optical path length of the closed loop resonator to change due to thermal expansion and/or changes in the resonator's optical properties. If such a change in ambient temperature were to happen between a control measurement and an analyte being added to the sample region, the shift in resonance peaks due to the change in ambient temperature may be indistinguishable from the shift due to the presence of the analyte.

[0036] Environmental factors such as ambient temperature may therefore be monitored separately and compensated for retroactively (e.g. by using a look-up table or previously characterised relationship), but this may not be possible or sufficiently accurate for all factors effecting the positions of resonance peaks (e.g. physical stresses on the closed loop resonator).

[0037] In some sets of embodiments, additionally or alternatively, the optical sensing apparatus comprises a second closed loop resonator and a second sample region adjacent the second closed loop resonator. The input waveguide may be optically coupled to a (second) input point on the second closed loop resonator for introducing input light to the second closed loop resonator. The drop-port waveguide may be optically coupled to a (second) drop point on the second closed loop resonator for receiving dropped light from the second closed loop resonator. The apparatus may be arranged to additionally interfere light dropped from the second closed loop resonator with light from the reference waveguide. The spectrum of the output signal may comprise a first pattern of resonance peaks corresponding to the (first) closed loop resonator and a second pattern of resonance peaks corresponding to the second closed loop resonator. Alternatively, the (second) drop point on the second closed loop resonator may be coupled to a second output interface of the apparatus to output a second output signal separate from the (first) output signal; this may advantageously reduce the computational burden on the processing system, by generating two separate spectra directly, rather than a

combined spectrum, but it may require a second light detector which may increase hardware costs.

[0038] In some embodiments, the sample region is spaced apart from the second sample region. The sample region may be arranged to hold a first substance (e.g. comprising a target analyte) whilst the second sample region may be arranged to hold a second substance (e.g. comprising the same or a different analyte, or a control substance such as an aqueous buffer solution or air). The apparatus may provide an opening or well (e.g. in an optical cladding layer), for retaining a sample in the sample region, although this is not essential. In some embodiments, the first pattern of resonance peaks corresponds to a first substance and the second pattern of resonance peaks corresponds to a second substance.

[0039] The second closed loop resonator may have the same path length as the (first) closed loop resonator. The spacing of the first pattern of resonance peaks in the output signal may then be substantially identical to that of the second pattern of resonance peaks when no samples are present. When the (first) sample region holds a sample and the second sample region holds a control substance, a wavelength separation between the first and second patterns may then be measured to determine one or more properties of the sample, without needing to perform a control measurement and with environmental effects inherently accounted for (because the second closed loop resonator will be subject to similar if not identical environmental conditions to the first closed loop resonator and thus the first and second patterns would be affected substantially identically by any change in environment conditions).

[0040] In other embodiments, the second closed loop resonator may have a different path length to the (first) closed loop resonator (e.g. the closed loop resonators may comprise circular waveguides with different diameters), such that the spacing of the first pattern of resonance peaks in the output signal is different to that of the second pattern of resonance peaks. This may make it easier to distinguish between resonance peaks produced from the closed loop resonator and the second closed loop resonator.

[0041] In some sets of embodiments featuring a second closed loop resonator, the second input point and drop points may be separated by a fraction of the optical path length of the second closed loop resonator that is equal to the fraction of the optical path length of the (first) closed loop resonator by which the (first) input and drop points are separated. In such cases, the first and second patterns of resonance peaks may be similar (i.e. they may share a common characteristic pattern), although the spacing between peaks may differ if the first and second closed loop resonators have different optical path lengths, e.g. by having different fabricated path lengths, or by being exposed to samples that affect their refractive indexes differently. For example, in an embodiment where the closed loop resonator and the second closed loop resonator comprise circular waveguides, the (first) input and drop points and the second input and drop points may both be separated the same angle around the circular waveguide (e.g. 90° or 180°).

[0042] Alternatively, the second input point and drop points may be separated by a fraction of the optical path length of the second closed loop resonator different to the fraction of the optical path length of the closed loop resonator by which the (first) input and drop points are separated. In such cases, the first and second patterns of resonance

peaks may be dissimilar, which may allow the first and second patterns to be more easily distinguished in a combined output signal.

[0043] In some embodiments featuring a second closed loop resonator, the drop-port waveguide may comprise a first arm that is optically coupled to the closed loop resonator and a second arm that is optically coupled to the second closed loop resonator. The first and second drop-port waveguide arms may be arranged such that the optical path length from the input interface to the input point plus the optical path length from the drop point to the output interface, is equal to the optical path length from the input interface to the second input point plus the optical path length from the second drop point to the to the output interface. For example, the second arm may be shorter than the first arm to compensate for a second closed loop resonator that is further from the input interface than the (first) closed loop resonator.

[0044] The closed loop resonator (and the second closed loop resonator) may comprise any waveguide that is looped back on itself. A closed loop resonator may, for example, be circular or ellipsoidal. Some examples of closed loop resonators which may be used in embodiments of the apparatus include ring resonators, racetrack resonators, microdisk resonators, microsphere resonators, microcapillary resonators, microtoroid resonators or optical fibre-based resonators.

[0045] The apparatus may comprise any number of closed loop resonators—e.g. two, three, five, ten or more. They may all be arranged to output drop-port light that interferes with light in the reference waveguide. This can enable multiplexed analysis of a large number of analytes (which could be in a common sample or in different samples) to be performed simultaneously using the one apparatus.

[0046] One or more of the waveguides of the optical sensing apparatus may comprise a planar waveguide, a strip waveguide, a rib waveguide, a slot waveguide or a segmented waveguide. One or more of the waveguides may comprise an optical fibre. One or more of the waveguides may be formed at least in part using glass, polymer or a semiconductor material (e.g. silicon). One or more of the waveguides may comprise a single-mode waveguide. One or more of the waveguides may comprise a multi-mode waveguide.

[0047] The optical sensing apparatus may comprise a substrate (e.g. a silicon, glass, polymer or silicon nitride substrate) on which one or more of the elements of the optical sensing apparatus (e.g. the waveguides and/or closed loop resonator(s)) are formed. The optical sensing apparatus may be a monolithic component (e.g. a photonic chip). The optical sensing apparatus may comprise a semiconductor material and/or dielectric material (e.g. silicon dioxide). The semiconductor material and/or dielectric material may be grown on a substrate (e.g. glass, silicon, or a group III-IV material substrate). For example, a semiconductor material and/or dielectric material may be grown by means of an epitaxial process (e.g. molecular beam epitaxy) or a deposition process (e.g. a sputtering process or chemical vapour deposition). The elements of the optical component may be monolithically integrated onto a substrate of the optical component, which may be a planar substrate.

[0048] The sample region may comprise a sensing layer, which may be located adjacent one or more of the closed loop resonators. The sensing layer may be immobilised on a surface of the ring resonator. The sensing layer may be

arranged to bind a target analyte in a sample when the sample is present in the sample region. A plurality of different sample layers, which bind different respective target analytes, may be located adjacent different respective closed loop resonators.

[0049]   According to a second aspect of the present invention there is provided a sensing system comprising:

[0050]   the optical sensing apparatus as disclosed herein;

[0051]   a light source arranged to provide input light to the input interface of the optical sensing component; and

[0052]   a light detector arranged to receive the output signal from the output interface of the optical sensing component.

[0053]   The light source may be a monochromatic light source. It may be a spatially-coherent light source (e.g. when single-mode waveguides are used). Preferably the wavelength of monochromatic light provided by the light source is adjustable (i.e. the light source comprises a tunable light source). As mentioned above, the pattern of resonance peaks in the output signal means that only a subset of the resonance peaks in the pattern may need to be observed to establish the magnitude of a shift without ambiguity. Thus the range of wavelengths over which the output signal needs to be observed to identify unambiguously a shift in the positions of the resonance peaks may be smaller compared to conventional approaches. The light source may have a tunable range (i.e. the range of wavelengths of monochromatic light the light source is able to produce) which is of the same order as, or which is equal to or greater than, twice the free spectral range of the closed loop resonator and/or equal to or greater than the period of a pattern of resonance peaks in the output signal. The tunable range of the light source is preferably less than 20 nm and further preferably less than 15 nm, e.g. 10 nm, 8 nm or 5 nm or less. This may reduce the cost and complexity of the light source that can be used satisfactorily with embodiments of the invention.

[0054]   In some sets of embodiments, the light source comprises a tunable laser (e.g. an external-cavity tunable diode laser , a distributed Bragg reflector laser, a distributed feedback semiconductor laser, or a solid state laser such as an Nd:YAG laser).

[0055]   The light detector may comprise any device capable of measuring an intensity of incident light, e.g. a photodetector.

[0056]   The sensing system may comprise a processing system or device, which may be arranged to receive an electrical signal from the light detector. The processing system may be configured to process the electrical signal to determine a property of a sample in the sample region. It may be arranged to record a spectrum of light detected by the light detector—e.g. as the wavelength of the light source is changed over time. The processing system may be arranged to determine a position of a resonance peak in a spectrum of light detected by the light detector. The processing device may be arranged to compare two spectra to determine a shift in resonance peaks.

[0057]   In some embodiments, the processing system is configured to:

[0058]   determine data representative of a spectral response of the optical sensing apparatus to the input light;

[0059]   access stored data representative of a predetermined spectral pattern; analyse the spectral response to detect the predetermined spectral pattern in the spectral response;

[0060]   determine a position of the predetermined spectral pattern within the spectral response; and

[0061]   determine the property of a sample in the sample region at least in part based on said position.

[0062]   The processing system may perform a cross-correlation operation to determine the position of the predetermined spectral pattern within the spectral response. The processing system may be configured to determine the positions of a plurality of predetermined spectral patterns within the spectral response—e.g. corresponding to different respective closed loop resonators.

[0063]   The sensing system may comprise a second light detector arranged to receive light from the through-port output interface of the optical sensing component. The processing system may be arranged to determine a through-port spectrum of light detected by the second light detector. The processing system may be arranged to determine a position of a resonance peak in a through-port spectrum. The processing system may be arranged to use a determined position of a resonance peak in a through-port spectrum to determine and/or refine the position of a resonance peak in a spectrum of light detected by the light detector.

[0064]   The sensing system may comprise a controller arranged to control the wavelength of light provided by the light source. The controller may be arranged to control the light source so as to sweep the wavelength of input light across a predefined range.

[0065]   The processing system may acquire a series of spectra over time. It may process these to monitor a property of the sample over time—e.g. to measure a rate of change in concentration of an analyte.

[0066]   The processing system may comprise a processor and a memory storing software instructions which, when executed by the processor, perform any of the processing steps disclosed herein. The processing system may be local to or remote from the optical sensing apparatus. It may comprise a remote server.

[0067]   The light source and light detector may be coupled to the optical sensing apparatus via one or more optical fibres.

[0068]   Features of any aspect or embodiment described herein may, wherever appropriate, be applied to any other aspect or embodiment described herein. Where reference is made to different embodiments, it should be understood that these are not necessarily distinct but may overlap.

BRIEF DESCRIPTION OF THE DRAWINGS

[0069]   One or more non-limiting examples will now be described, by way of example only, and with reference to the accompanying figures in which:

[0070]   FIG. 1 is a schematic plan view of an optical sensing component according to a first embodiment of the invention;

[0071]   FIG. 2 is a schematic partial cross-sectional side view of the optical sensing apparatus along the line A-A shown in FIG. 1;

[0072]   FIG. 3 is a graph of part of the spectral response at the through-port output of the optical sensing component shown in FIGS. 1 and 2;

[0073] FIG. 4 is a graph of part of the spectral response at the output of the optical sensing component shown in FIGS. 1 and 2;

[0074] FIG. 5 is a schematic plan view of an optical sensing component according to a second embodiment of the invention;

[0075] FIG. 6 is a graph of the components in the spectral response measured at the output of the optical sensing component shown in FIG. 5;

[0076] FIG. 7 is a graph of the spectral response measured at the output of the optical sensing component shown in FIG. 5;

[0077] FIG. 8 is a perspective schematic view of a sensing system according to an embodiment of the present invention;

[0078] FIG. 9 is a photographic slide of an exemplary fabricated photonic chip embodying the invention; and

[0079] FIG. 10 is a graph of the measured spectral response of the exemplary photonic chip shown in FIG. 9.

DETAILED DESCRIPTION

[0080] As illustrated in FIG. 1, an optical sensing apparatus 2 comprises a base substrate 1 (e.g. of silicon) supporting a lower cladding layer 3 (e.g. a silicon dioxide substrate) onto which a network of strip waveguides (e.g. of crystalline silicon) are formed. These waveguides include an input waveguide 4, a reference waveguide 6, a ring resonator 8 (in this case comprising a circular waveguide), a drop-port waveguide 10 and an output waveguide 12. The apparatus 2 may have a solid upper cladding layer 11 (e.g. a further oxide layer) over most of its surface, or it may have no upper cladding layer and instead employ a gaseous or liquid cladding layer when in use.

[0081] The input waveguide 4 and the reference waveguide 6 are both arranged to receive input light from an input interface 14, via a Y-branch splitter 5. The reference waveguide 6 comprises a compensation curve 7, which, as explained in more detail below, is dimensioned to optimise the performance of the apparatus 2.

[0082] The input waveguide 4 passes adjacent the ring resonator 8, with the point of closest approach being at a first point 16, and continues to a through-port output interface 18. The drop-port waveguide 10 passes adjacent the ring resonator 8, with the point of closest approach being at a second point 20, and goes on to merge with the reference waveguide 6, at a Y-branch combiner 9. The Y-branch combiner 9 leads to the output waveguide 12, which carries output light to an output interface 22. The first point 16 and the second point 20 are separated by a path length along the ring resonator 8 that is approximately a quarter of the total path length of the ring resonator 10 (i.e. consisting of a 90° arc around the circular waveguide 8).

[0083] As shown in FIGS. 1 and 2, the optical sensing apparatus 2 has a sample region 24 that is located above the ring resonator 8. This region 24 may be defined by an opening in an upper cladding layer (e.g. a square well for holding a liquid sample), or it may comprise a region of free space adjacent a face of the apparatus 2. The region 24 further comprises a sensing layer 13 of receptor molecules, immobilised on the surface of the ring resonator 8. The sensing layer 13 may cover the whole ring resonator 8, or, as shown in FIG. 1, it may have small breaks by the first and second points 16, 20, so that the sample does not have an undesired effect on the input waveguide 4 and drop-port

waveguide 10. When a sample (e.g. a biological analyte) is present in the sample region 24, a target molecule can bind to the receptor molecules and interact with the evanescent field of light in the ring resonator 8, changing the effective optical path length of the ring resonator 8.

[0084] The optical sensing apparatus 2 in this example is a single monolithic component, e.g. a photonic chip, although this is not essential.

[0085] In use, monochromatic light (e.g. from a tunable laser) is provided to the input interface 4 (e.g. via an optical fibre, not shown in FIG. 1). The light passes along the input waveguide 4 and the reference waveguide 6. As light in the input waveguide 4 passes the ring resonator 8, it can couple light into the ring resonator 8 via evanescent coupling. Similarly, light in the ring resonator 8 couples into the drop-port waveguide 10 via evanescent coupling.

[0086] When the optical path length of the ring resonator 8 is not an integer multiple of the wavelength of the input light, there is no resonance and minimal power is diverted into the ring resonator 8 from the input waveguide 4. The intensity of light at the through-port output interface 18 is thus substantially equal to the intensity of the input light received by the input waveguide 4. Similarly, minimal power is in turn coupled into the drop-port waveguide 10. The light in the output waveguide 12 arriving at the output interface 22 thus has an intensity approximately equal to that of the input light received by the reference waveguide 6.

[0087] FIG. 3 shows the intensity of light emanating from the through-port output interface 18, as a function of input wavelength. It can be seen that, at and around a wavelength of approximately 1.54×10^{-6} m, for example, no resonance occurs and the intensity of light at the through-port output interface 18 is roughly constant at 1.

[0088] However, when the optical path length of the ring resonator 8 is an integer multiple of the wavelength of the input light, waves in the ring resonator 8 interfere constructively and a resonant standing wave is set up in the ring resonator 8. Almost all of the light from the input waveguide 4 couples to the ring resonator 8 and the intensity of light at the through-port output interface 18 drops to near zero. This can be seen in FIG. 3 for a wavelength of approximately 1.58×10^{-6} m, for example.

[0089] FIG. 4 shows the intensity of light emanating from the output interface 22, as a function of input light wavelength. It can be seen that, at and around an exemplary non-resonant wavelength of 1.54×10^{-6} m, the intensity of the light at the output interface 22 is roughly constant at 0.3.

[0090] The phase difference in the standing wave in the ring resonator 8 between the first point 16 and the second point 20 is dependent upon the separation of the first and second points 16, 20 and upon the wavelength of the light. When the separation between the first and second points 16, 20 is equal to an integer number of wavelengths of the input light, the two points are in phase. This situation is exemplified at the first dashed line 31 in FIGS. 3 & 4. When the separation between the first and second points 16, 20 is equal to an integer number of wavelengths plus half a wavelength, the two points are exactly out of phase. This situation is exemplified at the second dashed line 32 in FIGS. 3 & 4. For other resonant wavelengths, the phases of the light at the two points 16, 20 may have a difference somewhere between 0 and π.

[0091] Therefore, at resonant wavelengths, light coupled into the drop-port waveguide 10 has a wavelength-depen-

dent phase difference, at the Y-branch combiner **9**, relative to light in the reference waveguide **6**. The phase difference is different for different resonances.

[0092] For the apparatus **2** described with reference to FIGS. **1**-**4**, the separation between the first and second points **16**, **20** is a quarter of the optical path length of the ring resonator **8** (an angular separation of 90°). Thus, the phase difference between light in the drop-port waveguide **10** and light in the reference waveguide **6**, when they join at the at the Y-branch combiner **9**, changes by $2\pi/4$ for successive resonances. By carefully selecting the length of the compensation curve **7**, the apparatus can be tuned such that the light in the drop-port waveguide **10** and the light in the reference waveguide **6** are exactly in phase, at the Y-branch combiner **9**, for every fourth resonant peak. For the three intermediary resonant peaks, the phase difference between light in the drop-port waveguide **10** and the reference waveguide **6** at the Y-branch combiner **9** will be, successively, $\pi/2$, π (i.e. out-of-phase) and $3\pi/2$.

[0093] Thus, the intensity of light at the output interface **22**, at successive resonant peaks, cycles through four values:

[0094] a maximum value corresponding to complete constructive interference between the light in the drop-port waveguide **10** and the reference waveguide **6** (where they are in-phase);

[0095] a first intermediary value corresponding to partial constructive interference;

[0096] a minimum value (i.e. zero) corresponding to complete destructive interference; and

[0097] a second intermediary value corresponding to partial constructive interference.

[0098] The peaks with the first and second intermediary values also have a different spectral shape (e.g. comprising sudden dips or rises in intensity).

[0099] Thus, the pattern of peaks in the intensity of the output interface **22** shown in FIG. **4** has a period of four times the separation of adjacent resonant peaks of the ring resonator **8** in FIG. **3**.

[0100] The optical sensing apparatus **2** may be used to determine properties of and/or identify a sample (e.g. to detect a particular analyte in a biological sample). First, a control measurement of the spectral response of the optical sensing apparatus is made (e.g. with only an aqueous buffer solution present in the sample region **24**) by sweeping the wavelength of the input light over a predefined range and observing the pattern of resonant peaks at the output interface **22**.

[0101] A sample is then introduced to the sample region **24**, and the spectral response of the optical sensing apparatus **2** again measured by sweeping the wavelength of the input light over the predefined wavelength range and observing the pattern of resonant peaks at the output interface **22**. Because the analyte in the sample region can interact with the sensing layer **13** to change the optical path length of the ring resonator **8**, the wavelengths at which resonances occur (i.e. the positions of the resonant peaks) shift. The magnitude of this shift can be measured to determine the presence of and/or properties of a target analyte in the sample region **24**. In some cases the spectral response may be continuously measured (i.e. by repeatedly sweeping the wavelength of the input light) as the sample interacts with the sensing layer **13**, such that the shift in the positions of the resonant peaks can be observed over time—and potentially in real time. Because the pattern of intensities of peaks in the output

signal has, in this example, a period of four resonant peaks, a large shift (e.g. of up to 0.045×10^{-6} m) may be observed without ambiguity.

[0102] Another optical sensing apparatus **102** is shown in FIG. **5**. The optical sensing apparatus is similar to that of FIG. **1**. It comprises a substrate (e.g. a silicon substrate) onto which an input waveguide **104**, a reference waveguide **106**, a first ring resonator **108**, a second ring resonator **109**, a first drop-port waveguide arm **110**, a second drop-port waveguide arm **111** and an output waveguide **112** are formed. The input waveguide **104** and the reference waveguide **106** are both arranged to receive input light from an input interface **114**, via a Y-branch splitter **115**. The reference waveguide **106** comprises a compensation curve **107**. The first ring resonator **108** comprises a circular waveguide with a first diameter (e.g. of around 50 μm). The second ring resonator **109** comprises a second waveguide with a second, larger diameter (e.g. of around 100 μm).

[0103] The input waveguide **104** passes adjacent the first ring resonator **108** and the second ring resonator **109**, and continues to a through-port output interface **118**. The first drop-port waveguide arm **110** passes adjacent the first ring resonator **108**, and the second drop-port waveguide arm **111** passes adjacent the second ring resonator **109**. The points at which the input waveguide **104** and the first drop-port waveguide arm **110** pass closest to the first ring resonator **108** are separated by a quarter of the optical path length of the first ring resonator **108** (i.e. 90° around the circular waveguide). The points at which the input waveguide **104** and the second drop-port waveguide arm **110** pass closest to the second ring resonator **109** are separated by half of the optical path length of the second ring resonator **108** (i.e. 180° around the circular waveguide).

[0104] The first and second drop-port waveguide arms **110**, **111** go on to merge at a first Y-branch combiner **116** to form a common drop-port waveguide which then merges with the reference waveguide **106** at a second Y-branch combiner **119**. This becomes the output waveguide **112**, which carries output light to an output interface **122**. The first drop-port waveguide **110** includes a U-shaped compensation curve so that the paths through the first and second ring resonators **108**, **109** can each be balanced relative to the reference waveguide **106**, for their respective resonant wavelengths.

[0105] The optical sensing apparatus **102** comprises a first sample region **124** located above the first ring resonator **108** and a second sample region **126** located above the second ring resonator **109**. A sample (e.g. a biological analyte) present in the first or second sample region interacts with the evanescent field of light in the first or second ring resonator **108**, **109** respectively, changing the optical path length of the first or second ring resonator **108**, **109**. The two sample regions **124**, **126** may be physically separated so that they can hold two different samples (e.g. two different analytes, or an analyte and a control substance) simultaneously, or the first and second ring resonators **108**, **109** may have different chemical sensing layers bonded to respective exposed faces.

[0106] In use, monochromatic light (e.g. from a laser) is provided to the input interface **104** (e.g. via an optical fibre, not shown). The light passes along the input waveguide **104** and the reference waveguide **106**. As light in the input waveguide **104** passes the first and second ring resonators **108**, **109**, it couples light into the ring resonators **108**, **109** via evanescent coupling. Similarly, at appropriate wave-

8

lengths, light in the ring resonators **108**, **109** couples light into the first and second drop-port waveguides **110**, **111** via evanescent coupling.

[0107] As with the ring resonator **8** of the optical sensing apparatus **2** described above with reference to FIGS. **1**-**4**, the first and second ring resonators **108**, **109** each exhibit resonances when the wavelength of the input light is a submultiple of their optical path lengths. The first and second ring resonators **108**, **109** are different sizes and thus resonate at different (potentially overlapping) sets of wavelengths. Away from these resonances (i.e. at a wavelength that is not a submultiple of the optical path length of either ring resonator **108**, **109**), there is minimal power in the drop-port waveguides **110**, **111** and the light in the output waveguide **112** output by the output interface **122** has an intensity approximately equal to that of the input light received via the reference waveguide **106**.

[0108] The spectrum of light output by the output **122** is illustrated in FIGS. **6** and **7**. FIG. **6** which shows a first pattern of resonant peaks **602** corresponding to the first ring resonator **108** and a second pattern of resonant peaks **604** corresponding to the second ring resonator **109**. The first and second patterns **602**, **604** are shown separately in FIG. **6** for clarity but of course in reality a single output signal **700** shown in FIG. **7** is measured at the output **122** (i.e. comprising a superposition of the two signals shown in FIG. **6**). Because the resonant peaks of the first and second patterns **602**, **604** are generally narrow and sometimes fall at different wavelengths, it is possible to distinguish the two patterns from the spectrum of the single output signal **700**—e.g. using corresponding cross-correlation operations. FIG. **8** is a simplified diagram of a sensing system **200** which comprises a light source (e.g. a tunable laser) **202**, the optical sensing apparatus **2** described above with reference to FIGS. **1**-**4** and a light detector (e.g. a photodetector) **204**. The sensing system may also be used with the optical sensing apparatus **102** illustrated in FIG. **5**.

[0109] The light source **202** is arranged to provide monochromatic light with a configurable wavelength to the input interface **14** of the optical sensing apparatus **2**. The light detector **204** is arranged to detect the intensity of light output by the output **22** of the optical sensing apparatus **2**. Light from the light source **202** travels through single-mode optical fibres via polarisation paddles **206** to the input interface **14**. The dimensions of the waveguides of the optical sensing apparatus **2** are chosen in such a way that only the fundamental mode of TE or TM propagates through them. The polarization paddles **206** are used to match the polarization of the input light to the mode (Single TE or TM mode) supported by the waveguides. Light from the output **22** travels through a single-mode optical fibre to the light detector **204**, which is connected to a workstation **208** (e.g. a computer executing software) arranged to record and process the detected intensities for different wavelengths of input light to generate a spectrum.

[0110] The sensing system **200** is arranged to enable a user to determine one or more properties of a sample. The sample is added to the sample region **24** of the optical sensing apparatus **2** (e.g. by being washed over the upper face of the photonic chip **2**), and a spectrum of light from the output **22** (i.e. the spectral response of the optical sensing apparatus **2**) is measured by operating the light source to sweep the wavelength of light it produces over a predetermined range, whilst the intensity of light at the output **22** is measured

using the light detector **204** and recorded by the processor **208**. In some alternative embodiments, the input light may be generated by a broadband light source, and a spectrum analyser may be coupled to the output **22**.

[0111] The spectrum comprises resonant peaks corresponding to resonances of the closed loop resonator **8**. The position of these resonant peaks is compared to a control spectrum (corresponding to having a control sample in the sample region **24**, such as an aqueous buffer solution) and a shift in the position of the peaks is calculated. Because the presence of the target analyte in the sample region **24** alters the refractive index, and hence optical path length, of the closed loop resonator **8**, the shift in the positions of the resonant peaks can be used to detect the analyte and/or to determine one or more properties of the analyte (e.g. its concentration in the sample).

[0112] A series of spectra may be collected over time and analysed to determine further information about the sample.

[0113] In some embodiments, a photonic chip may have a larger number of ring resonators—e.g. three, five, ten or more—all arranged in parallel with the reference waveguide. Because their respective spectral signatures repeat only over a relatively long wavelength span, it can still be possible to identify each signature separately within the output intensity signal. Such multiplexing can enable a large number of analytes to be detected simultaneously.

[0114] In some embodiments, the interfering reference path may be provided at least partly outside the photonic chip. In some arrangements, the Y-branch splitter **5**, **115** and/or the Y-branch combiner **9**, **119** may be located off the chip—e.g. using a discrete beam splitter. The chip may have no reference waveguide, e.g. with the reference waveguide being provided by a separate optical fibre. The input interface **14**, **114** may then be coupled only to the input waveguide **4**, **104**. Or the input interface **14**, **114** may comprise a first port coupled to the input waveguide **4**, **104** and a second port coupled to a reference waveguide portion (not shown). Similarly, the output interface **22**, **122** may be coupled only to the output waveguide **12**, **112**, or it may comprise a first port coupled to the output waveguide **12**, **112** and a second port coupled to a reference waveguide portion (not shown).

[0115] In some embodiments, there may be no first Y-branch combiner **116**, and the second drop-port waveguide **110** may remain separate from the first drop-port waveguide **111**. The second drop-port waveguide **110** may instead merge with the reference waveguide **106** at a separate Y-branch combiner, distinct from the second Y-branch combiner **119**, and leave the chip **102** at a separate port, as a second output signal.

[0116] In some embodiments, the apparatus is not a photonic chip, but is formed from discrete optical components, e.g. connected by optical fibres or through air.

Example

[0117] A photonic chip **800** was manufactured and is shown in FIG. **9**. Its design is similar to that described above with reference to FIGS. **1** and **2**. The photonic chip **800** comprises an input interface, an input waveguide, a reference waveguide, a circular waveguide ring resonator with a diameter of approximately 30 μm (i.e. with a path length of approximately 95 μm), a drop-port waveguide and an output waveguide. The input waveguide is configured to direct light from the input interface into the ring resonator, and the drop-port waveguide is configured to receive dropped light

from the ring resonator. The input waveguide and the drop-port waveguide is optically coupled to the ring resonator at points separated by 180° (i.e. half the optical path length of the ring resonator). The ring resonator may be coated with a sensing layer to form an active sample region adjacent the ring resonator.

[0118] The reference waveguide and the drop-port waveguide merge at the output waveguide such that input light in the reference waveguide interferes with dropped light in the drop-port waveguide. The interfering light is directed through the output waveguide to a signal output. The input waveguide continues past the ring resonator to a through-port output.

[0119] Monochromatic light was input to the input interface and the intensity of light output by the through-port output and the signal output was measured whilst the wavelength of the input light was varied, to produce an interference output spectrum **802** and a through-port output spectrum **804**, which are shown in FIG. **10**.

[0120] The through-port output spectrum **804** comprises a series of dips **806**, with substantially the same intensity, at wavelengths corresponding to resonances of the ring resonator. The free spectral range of the through-port output spectrum **804** is equal to the separation of the resonance peaks, i.e. approximately 5 nm.

[0121] The output spectrum **802**, however, comprises a pattern of resonance peaks **808** with intensities that alternate between a high value and a low value. The repetition period of the output spectrum **802** is thus equal to twice the separation of the resonance peaks, i.e. approximately 10 nm. This may correspond to a doubling in the dynamic range.

[0122] While the invention has been described in detail in connection with only a limited number of embodiments, it should be understood that the invention is not limited to such disclosed embodiments. Rather, the invention can incorporate any number of variations, alterations, substitutions or equivalent arrangements within the scope of the appended claims.

1. An optical sensing apparatus comprising:
an input interface for receiving input light into the optical sensing apparatus;
an input waveguide and a reference waveguide, both arranged to receive input light from the input interface;
a closed loop resonator, wherein the input waveguide is optically coupled to the closed loop resonator at an input point for introducing input light to the closed loop resonator;
a sample region, adjacent the closed loop resonator, for receiving a sample such that evanescent coupling can occur between light in the closed loop resonator and the sample;
a drop-port waveguide, optically coupled to the closed loop resonator at a drop point for receiving dropped light from the closed loop resonator;
an output waveguide; and
an output interface,
wherein the reference waveguide and the drop-port waveguide are arranged to direct interfering light through the output waveguide to produce an output signal at the output interface.

2. The optical sensing apparatus of claim **1**, wherein the output signal has a spectral response to the input light that

comprises a periodic pattern of resonance peaks that depends at least partially on a property of a sample in the sample region.

3. The optical sensing apparatus of claim **2**, arranged such that the periodic pattern of resonance peaks has a period of at least three resonance peaks.

4. The optical sensing apparatus of claim **1**, wherein the input point and the drop point are separated by less than half the optical path length of the closed loop resonator.

5. The optical sensing apparatus of claim **4**, wherein the input point and the drop point are separated by less than 45% of an optical path length of the closed loop resonator.

6. The optical sensing apparatus of claim **1**, wherein the input point and the drop point are separated by a submultiple of an optical path length of the closed loop resonator.

7. The optical sensing apparatus of claim **1**, further comprising a through-port waveguide arranged to receive light from the input waveguide that does not couple into the closed-loop resonator and to direct said light to a through-port output interface.

8. The optical sensing apparatus of claim **1**, wherein a total optical path length from the input interface to the output interface through the reference waveguide is equal to: an optical path length from the input interface to the input point of the closed loop resonator, plus an optical path length from the drop point of the closed loop resonator to the output interface.

9. The optical sensing apparatus of claim **1**, further comprising a second closed loop resonator and a second sample region adjacent the second closed loop resonator, wherein the input waveguide is optically coupled to a second input point on the second closed loop resonator for introducing input light to the second closed loop resonator, and the drop-port waveguide is optically coupled to a second drop point on the second closed loop resonator for receiving dropped light from the second closed loop resonator.

10. The optical sensing apparatus of claim **9**, wherein the sample region is spaced apart from the second sample region.

11. The optical sensing apparatus of claim **9**, wherein a total optical path length from the input interface to the output interface through the reference waveguide is equal to: an optical path length from the input interface to the second input point, plus an optical path length from the second drop point to the output interface.

12. The optical sensing apparatus of claim **9**, wherein the second closed loop resonator has a different optical path length to the closed loop resonator.

13. The optical sensing apparatus of claim **9**, wherein the second input point and drop points are separated by a fraction of the optical path length of the second closed loop resonator that is equal to a fraction of the optical path length of the closed loop resonator by which the input and drop points are separated.

14. The optical sensing apparatus of claim **9**, wherein the second input point and the second drop point are separated by a fraction of an optical path length of the second closed loop resonator different to a fraction of an optical path length of the closed loop resonator by which the input point and the drop point are separated.

15. The optical sensing apparatus of claim **9**, wherein the drop-port waveguide comprises a first arm that is optically coupled to the closed loop resonator and a second arm that is optically coupled to the second closed loop resonator.

16. The optical sensing apparatus of claim **15**, wherein the first and second drop-port waveguide arms are arranged such that an optical path length from the input interface to the input point plus an optical path length from the drop point to the output interface, is equal to an optical path length from the input interface to the second input point plus an optical path length from the second drop point to the to the output interface.

17. The optical sensing apparatus of claim **1**, wherein the closed loop resonator has an optical path length of at least 100 μm.

18. The optical sensing apparatus of claim **1**, being a photonic chip.

19. The optical sensing apparatus of claim **1**, wherein the sample region comprises a sensing layer adjacent the closed loop resonator for binding an analyte in the sample region.

20. The optical sensing apparatus of claim **1**, comprising an optical splitter comprising an input optically coupled to the input interface, a first output optically coupled to the reference waveguide, and a second output optically coupled to the input waveguide.

21. The optical sensing apparatus of claim **1**, comprising an optical combiner comprising a first input optically coupled to the reference waveguide, a second input optically coupled to the drop-port waveguide, and an output optically coupled to the output waveguide.

22. A sensing system comprising:

an optical sensing apparatus, the optical sensing apparatus comprising:

an input interface for receiving input light into the optical sensing apparatus;

an input waveguide and a reference waveguide, both arranged to receive input light from the input interface;

a closed loop resonator, wherein the input waveguide is optically coupled to the closed loop resonator at an input point for introducing input light to the closed loop resonator;

a sample region, adjacent the closed loop resonator, for receiving a sample such that evanescent coupling can occur between light in the closed loop resonator and the sample;

a drop-port waveguide, optically coupled to the closed loop resonator at a drop point for receiving dropped light from the closed loop resonator;

an output waveguide; and

an output interface,

wherein the reference waveguide and the drop-port waveguide are arranged to direct interfering light through the output waveguide to produce an output signal at the output interface; and

wherein the sensing system further comprises:

a light source arranged to provide the input light to the input interface of the optical sensing apparatus; and

a light detector arranged to receive the output signal from the output interface of the optical sensing apparatus.

23. The sensing system of claim **22**, wherein the light source comprises a tunable laser.

24. The sensing system of claim **23**, wherein the light source comprises a tunable laser that has a tunable range which is equal to or greater than twice a free spectral range of the closed loop resonator, and/or which is equal to or greater than a period of a pattern of resonance peaks in the output signal.

25. The sensing system of claim **23**, wherein the light source comprises a tunable laser that has a tunable range of 10 nm or less.

26. The sensing system of claim **22**, further comprising a processing system arranged to receive an electrical signal from the light detector, wherein the processing system is configured to process the electrical signal to determine a property of a sample in the sample region.

27. The sensing system of claim **26**, wherein the processing system is configured to:

determine data representative of a spectral response of the optical sensing apparatus to the input light;

access stored data representative of a predetermined spectral pattern;

analyse the spectral response to detect the predetermined spectral pattern in the spectral response;

determine a position of the predetermined spectral pattern within the spectral response; and

determine the property of the sample in the sample region at least in part based on said position.

* * * * *

NTNU

Norwegian University of
Science and Technology